Measurements of ion temperatures and fast particles in the scrape-off layer of W7-X stellarator and EAST tokamak

Inaugural-Dissertation

zur Erlangung des Doktorgrades
der Mathematisch-Naturwissenschaftlichen Fakultät
der Heinrich-Heine-Universität Düsseldorf

vorgelegt von

Marion Henkel
aus Rostock

Jülich, August 2020

aus dem Institut für Laser- und Plasmaphysik
der Heinrich-Heine-Universität Düsseldorf

Gedruckt mit der Genehmigung der
Mathematisch-Naturwissenschaftlichen Falkultät
der Heinrich-Heine-Universität Düsseldorf

Berichterstatter:
1. Prof. Dr. Yunfeng Liang
2. Prof. Dr. Georg Pretzler

Tag der mündlichen Prüfung: 08.10.2020

Zusammenfassung

In Anbetracht der Erfolge der Fusionsforschung in den letzten fünfzig Jahren, besteht eine der wichtigsten Herausforderungen bei Fusionsplasmageräten darin, die Wärmeabgabe zu verstehen und zu handbaben. Insbesondere die Kenntnis der Physik des Plasmas in der Randschicht ist von wesentlicher Bedeutung. Unter anderem ist die Ionentemperatur ein Schlüsselwert für das Verständnis der Eigenschaften der Randschicht und des Divertorbereichs. Während der Limiterkampagne und der ersten Divertorkampagne am Stellarator W7-X waren jedoch keine Messungen für Ionen in der Randschicht verfügbar. Daher wurde für die zweite Divertorkampagne am Stellarator W7-X eine Multikanal-Gegenfeldsonde entwickelt.

Diese Multikanal-Gegenfeldsonde und seine Inbetriebnahme werden in dieser Arbeit vorgestellt. Die Herausforderungen und Optimierungen wurden diskutiert, angefangen mit einer einfachen zweidimensionalen Sonde für einen Machbarkeitstest am linearen Plasmagerät PSI-2, bis hin zur ersten Multikanal-Gegenfeldsonde in den Kampagnen des Tokamak EAST in 2016 und 2017 und schlussendlich der optimierten Sonde am Stellarator W7-X in der zweiten Divertorkampagne.

In der Vergangenheit wurde gezeigt, dass die schnellen Ionen eine starke Rolle bei der Stabilität von Plasmen mir Randmoden spielen. Daher wurden Messungen von schnellen Teilchen im Bereich der Randschicht im Tokamak EAST während des Auftretens der Randmoden durchgeführt. Mit zusätzlichen Diagnostiken werden die vorausgegangene Moden aufgezeigt. Die Bildung und Ausbreitung schneller Teilchen im Plasmakern und das Auftreten in der Randschicht, gemessen mit der Multikanal-Gegenfeldsonde, zeigten, dass der Einschluss schneller Ionen in Randmoden weniger stabil ist als der Einschluss schneller Elektronen und sie schon früher verloren gehen. Weiterhin wird gezeigt, dass sich schnelle Ionen lokal in der horizontalen Mittelebene ausbreiten.

Darüber hinaus ist das Wissen über die Ionentemperaturen in der Randschicht für verschiedene Transportprozesse wie die ambipolare Diffusion im Plasmarand, die Anstiegszeit des Wärmeflusses während der Randmoden und die Plasmakollisionalität von wesentlicher Bedeutung. Da in den vorherigen Kampagnen keine Ionentemperaturmessungen in der Randschicht des Stellarators W7-X verfügbar waren, wurden während der zweiten Divertorkampagne Ionen- und Elektronentemperaturprofilmessungen durchgeführt. Es konnte gezeigt werden, dass die Inselstruktur in der Randschicht zu einem

Peak im Elektronentemperaturprofil führt, während sich das Ionentemperaturprofil abflacht. Erste Studien zum Verhältnis von Ionen- zu Elektronentemperatur wurden durchgeführt.

Zusammenfassend zeigt diese Arbeit die Machbarkeit und Flexibilität der Multikanal-Gegenfeldsonde sowohl für Tokamak als auch für Stellarator.

Abstract

Considering the fusion research achievements of the past fifty years, one of the most important challenges of fusion plasma devices is understanding and handling power exhaust. The knowledge of the physics of scrape-off layer plasma is particularly essencial. Amongst other parameters, the ion temperature is a key value for understanding the characteristics of the scrape-off layer and divertor region. However, during the limiter campaign and first divertor campaign on the stellarator W7-X, no measurements for ions in the the scrape-off layer were availible. Therefore a multi-channel retarding field analyzer was developed for the second divertor campaign on stellarator W7-X.

This multi-channel retarding field analyzer and its commissioning are presented in this thesis. The challenges and optimisations were discussed, starting with a simple 2-dimentional probe for a feasibility test on the linear plasma device PSI-2, continuing with the first multi-channel retarding field analyzer in the 2016 and 2017 campaigns of the tokamak EAST and finishing with the optimised probe on the stellarator W7-X in the second divertor campaign.

In the past, it was shown that the fast ions have a strong role in the stability of ELMy plasmas. Therefore, fast particle measurements in the scrape-off layer region of the tokamak EAST during ELMs were done. Using additional diagnostics, the preceding precursors are shown. The formation and propagation of fast particles in the plasma core and the apppearance in the scrape-off layer, measured with the multi-channel retarding field analyzer, showed, that the confinement of fast ions is less stable than the confinement of fast electrons during the ELM crash and they already get lost earlier. Furthermore, it is shown, that fast ions propagate locally in the horizontal midplane.

Further, the knowledge about ion temperatures in the scrape-off layer is essential for several transport processes, like the ambipolar diffusion in the plasma edge, heat flux rise time during ELM and the plasma collisionality. Because no ion temperature measurements in the scrape-off layer of the stellarator W7-X were available in the previous campaigns, ion and electron temperature profile measurements were done during the second divertor campaign. It could be shown, that the island structure in the scrape-off layer leads to a peaking in the electron temperature profile, whereas the ion temperature profile flattened. First studies about the ion to electron temperature ratio were conducted.

Summarised, this thesis demonstrates the feasibility and the flexibility of the multi-channel retarding field analyzer, as well as in the tokamak and stellarator case.

Author's declaration

I declare that the work in this dissertation was conducted in accordance with the requirements of the University's Regulations and Code of Practice for Research Degree Programmes and that it has not been submitted for any other academic award. Except where indicated by specific references in the text, the work is the candidate's own work.Work done in collaboration with, or with the assistance of, others, is indicated as such. Any views expressed in the dissertation are those of the author.

SIGNED: ..... DATE: .....

Acknowledgments

Firstly, I would like to express my sincere gratitude to my advisor Prof. Dr. Yunfeng Liang for his patience, motivation and immense knowledge, and his continuous support of my PhD and related research. His guidance helped me throughout the duration of researching and writing this thesis. I could not have imagined having a better advisor and mentor for my Ph.D study.

Besides my advisor, I would like to thank Prof. Dr. Georg Pretzler and Prof. Dr. Friedrich Wagner for their support and various discussions, which inspired me to widen my research from various perspectives.

My sincere thanks also goes to the Max-Planck Institute for Plasma Physics, the Institute of Plasma Physics of the Chinese Academy of Sciences, and the Institute of Fusion and Plasma Research of the Huazhong University of Science and Technology, which provided me an opportunity to join their team as intern, and who gave access to the laboratory and research facilities. Without their precious support it would not have been possible to conduct this research.

Further, I would like to thank Norbert Sandri, Daniel Höschen, and Guru Saatheeswaran for their great job assembling the multi-channel retarding field analyzer probes for several fusion devices.

I thank also my colleagues Philipp Drews, Alexander Knieps, Dr. Shaocheng Liu, Dr. Michael Rack, Dr. Nengchao Wang, Dr. Xiang Han and Jörg Cosfeld for the stimulating discussions, for the sleepless nights we were working together before deadlines, and for all the success we have had in the last five years.

Besides my colleagues, my gratitude goes to Casten Killer, Marcin Jabubowski, and Sebastijan Brezinski for the discussions and the support related to W7-X stellarator experiments, and to Dr. Yongliang Li for his support related to EAST tokamak experiments.

Last but not the least, I would like to thank my family for supporting me spiritually throughout writing this thesis and my life in general.

Publications

First author publication:

M. Henkel et al: *Development of a multi-channel retarding field analyzer for the SOL physics on EAST and W7-X*, europhysics conference abstracts Volume 41F (2017)

M. Henkel et al: *Multi-channel retarding field analyzer for EAST*, Plasma science and technology 20 (2018)

M. Henkel et al: *Retarding field analyzer for the Wendelstein 7-X boundary plasma*, Fusion Engineering and Design, Volume 157, 111623 (2020)

Other publications:

J. Cai et al.:*A new multi-channel Mach probe measuring the radial ion flow velocity profile in the boundary plasma of the W7-X stellarator*, Review of Scientific Instruments 90, 033502 (2019)

P. Drews et al.: *Magnetic configuration effects on the edge heat flux in the limiter plasma on W7-X measured using the infrared camera and the combined probe*, Plasma Science and Technology, Volume 20, 054003 (2018)

P. Drews et al.: *Operation of probe heads on the Multi-Purpose-Manipulator at W7-X in OP 1.2a*, Fusion Engineering and Design 146, 2353-2355 (2019)

Y. Li et al.: *Measurement of the edge ion temperature in W7-X with island divertor by a retarding field analyzer probe*, Nuclear Fusion 59, 126002 (2019)

Y. Liang et al.: *Diagnostic set-up and modelling for investigation of synergy between 3D edge physics and plasma-wall interactions on Wendelstein 7-X*, Nuclear Fusion 57, 066049 (2017)

S. Liu et al.: *Observations of the effects of magnetic topology on the SOL characteristics of an electromagnetic coherent mode in the first experimental campaign of W7-X*, Nuclear Fusion 58, 046002 (2018)

S. Liu et al.: *Characteristics of the SOL turbulence structure in the first experimental campaign on W7-X with limiter configuration*, Physics of Plasmas 25, 072502 (2018)

S. Liu et al.: *The effects of magnetic topology on the scrape-off layer turbulence transport in the first divertor plasma operation of Wendelstein* , Nuclear Fusion 59, 066001 (2019)

T. Sunn Pedersen et al.: *Confirmation of the topology of the Wendelstein 7-X magnetic field to better than 1:100,000*, Nature Communications volume 7, 13493 (2016)

T. Sunn Pedersen et al.: *First divertor physics studies in Wendelstein 7-X*, Nuclear Fusion 59, 096014 (2019)

Contents

1 Introduction

As a new source of power, nuclear fusion is a great opportunity for future power generation. Regarding the international energy agency, the international energy consumption will increase by 27 % within the next 20 years. However, using conventional power sources, like nuclear fission or fossil fuels, is limited due to their limited natural occurrence. That's why the use of so-called renewable energy sources must strongly increase within the next decades.

However, conventional renewable energy sources, like solar cell or wind turbines, are coupled to the environmental conditions and therefore can not always be adapted to the current power consumption. A suitable solution is a nuclear fusion power plant, as an environmentally independent energy source.

Nuclear fusion is not limited by fossil sources and is environmentally friendly because no green house gases are released. Furthermore, the operation of such a power plant is much safer than nuclear fission power plants.

Nowadays, the two concepts for confined fusion are tokamak and stellarator. They will be explained in more detail in this chapter.

Finally, the aim of this thesis will be expalined in the last part of this chapter.

1.1 Nuclear fusion plasmas

Using the opposite effect of nuclear fision, several individual particles can be merged to form larger particles in nuclear fusion. In this case, the binding energy is released because the nuclei mass is smaller by Δm compared to individual particles. Using Einstein's energy relation $\Delta E = \Delta m c^2$, this so-called mass defect is transferred into the form of kinetic energy to the reactants. In the fusion energy research, this mass defect is used to win energy from the merger of two hydrogen isotopes to a helium isotope. This energy can subsequently be converted into electric energy in power plants. At the world's largest tokamak, ITER, the following reactions will occur: [51]

$$\mathrm{D} + \mathrm{T} \rightarrow {}^4\mathrm{He}\,(3.5\,\mathrm{MeV}) + \mathrm{n}\,(14.1\,\mathrm{MeV}) \tag{1.1}$$

$$\mathrm{D} + \mathrm{D} \rightarrow {}^4\mathrm{He}\,(0.82\,\mathrm{MeV}) + \mathrm{n}\,(2.45\,\mathrm{MeV}) \tag{1.2}$$

Today's devices, both stellarators and tokamaks, are currently operated with pure hydrogen, deuterium, or helium as main plasma species. In future power plants, a mixure of half deuterium and half tritium will be used.

The strong nuclear force is required for nuclear fusion reactions, which acts in distances of the order of nucleon sizes. In this range the Coulomb forces dominates. To overcome the repulsive Coulomb force, the resultant particles must be heated to several hundreds of keV, depending on relative velocity v between the reactants and their charges Z. [44]

$$E \sim \exp\left(-\frac{Z_1 Z_2 e^2}{hv}\right) \tag{1.3}$$

If they overcome this repulsive field, they are able to merge. The generated helium isotopes then heat the plasma by collisions, are decelerated, and finally leave the plasma due to particle flow to the plasma edge. The produced neutrons, however, leave the plasma immediately, since they are not confined magnetically and can be used to generate electrical energy. In figure 1, the reaction probability can be seen with different reactants.

As shown in figure 1, the reaction probability of deuterium and tritium is greatest at around 100 million °C. In order to achieve these temperatures with heating, the contact

between particles and wall must be prevented. Most suitable are magnetic fields, whose influence on charged particle motion is described in section 1.2.1.

For a fusion power plant it is important that energy losses are compensated by collissions of the helium particles from fusion reaction with background plasma. The power contained in the plasma is given by

$$P_{\mathrm{P}} = n_1 n_2 \langle \sigma\nu \rangle E_\alpha V \tag{1.4}$$

where n are the reactant's average density, σ the reaction cross-section, v the relative energy, E_α the released binding energy, V the plasma volume and $\langle ... \rangle$ the average over maxwellian energy distribution of the particles of the fusion cross-section σ and the relativ velocity ν.

The total energy loss $P_{\mathrm{L}} = W/\tau$ by radiation and conductive losses through the scrape-off layer is defined by the energy confinement time τ inside the vessel and the thermal energy

$$W = 3 n_e k_{\mathrm{B}} T V \tag{1.5}$$

where T is the plasma temperature assumed by maxwellian energy distribution.

Using these equations, the conditions for ignition mean that energy won by collision compensates for energy losses, which can be derived from the energy balance equation from Lawson [44]

$$n\tau_E T > \frac{12 k_B T^2}{\langle \sigma\nu \rangle E_\alpha (1 + 5/Q)} \tag{1.6}$$

where Q is the ratio of power released by fusion reaction to external heating. As shown in figure 2, in the last half past century, the plasma conditions increased near to the ignition, but have not yet been achieved. To achieve these conditions, inter alia, the confinement time must be improved.

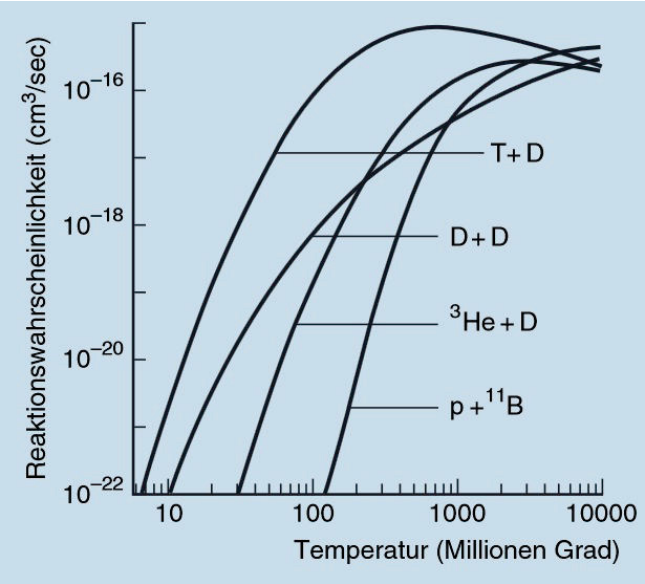

Figure 1: Reaction probability of a gas mixture of various reactants in dependence on the temperature. [51]

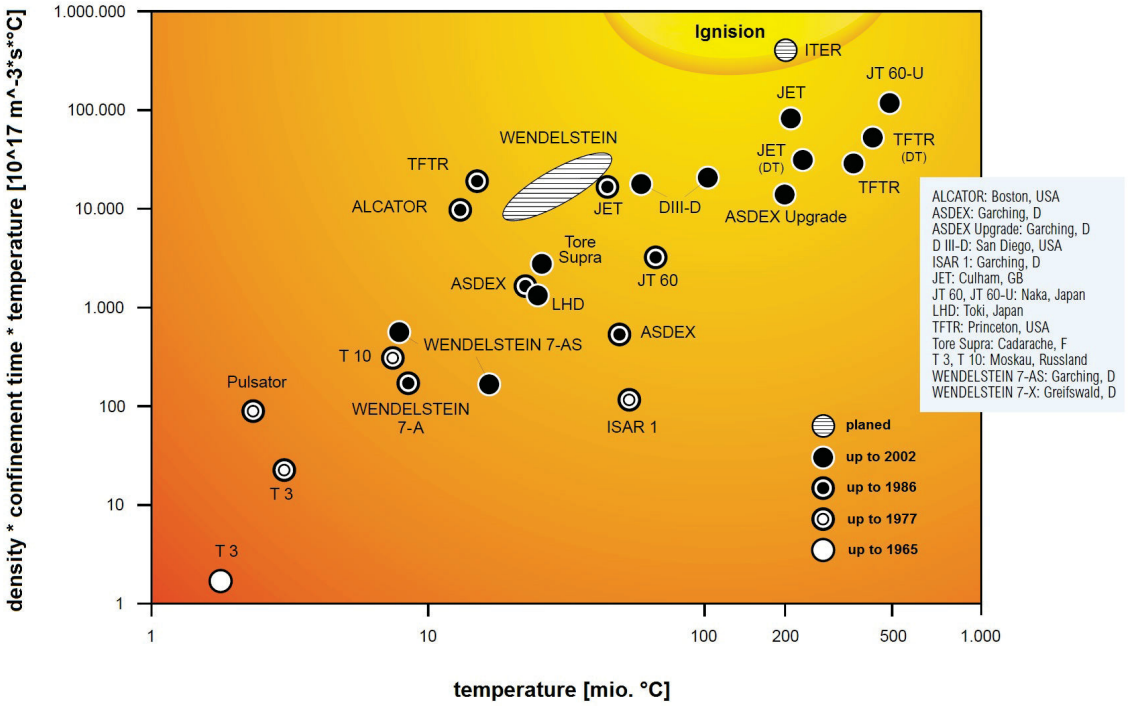

Figure 2: Achieved so-called fusion products and temperature for different fusion plasma devices. [51]

1.2 Principle of magnetic confinement fusion

1.2.1 Magnetic confinement and drift velocities in fusion devices

The plasma is confined magnetically, to avoid particle and heat losses, and damage of the boundary components caused by high heat load. That's why for each particle with a velocity $\vec{v}$ and a charge q a Lorentz force acts [60]:

$$\vec{F} = q\vec{v} \times \vec{B} \tag{1.7}$$

For the velocity component $\vec{v}_\perp$ perpendicular to the magnetic field $\vec{B}$, a force acts which is perpendicular to the magnetic field vector, and the velocity vector and therefore acts as a centripetal force around the magnetic field lines. Therefore, there is a gyration with the radius [60]

$$r_\mathrm{G} = \frac{m v_\perp}{|q|\, B} \tag{1.8}$$

and a cyclotron frequency of [60]

$$\omega_\mathrm{C} = \frac{qB}{m} \tag{1.9}$$

For velocity component $\vec{v}_\parallel$ parallel to the magnetic field lines, the particles are not affected. In summary, the movement of charged particles in a magnetic field can be described as a helical path.

To avoid end losses, in fusion devices the magnetic field lines are toroidal closed, in order to ensure efficient confinement of the charged particles. The resulting magnetic field, as well as other externally acting forces, lead to drift movements which are superposed on the helical motion.

In general, the drift velocity $\vec{v}_D$ can be described by [10]

$$\vec{v}_\mathrm{D} = \frac{\vec{F} \times \vec{B}}{qB^2} \tag{1.10}$$

The toroidal closed magnetic field system leads to inhomogeneities. Through the gradient of the magnetic field, a force $\vec{F} = -\mu\nabla\vec{B}$ acts on particles, which leads to a drift velocity [10]

$$\vec{v}_{\nabla\vec{B}} = \frac{-\mu\nabla\vec{B}\times\vec{B}}{qB^2} \tag{1.11}$$

A special case thereof is a curved system with radius R_C, which occurs in stellarators and tokamaks. There, curvature generates a radial force $\vec{F}_\mathrm{C} = m\vec{v}_\parallel^2\vec{R}_C\times\vec{B}/R_C^2$ and a drift velocity of [10]

$$\vec{v}_\mathrm{R} = \frac{m\vec{v}_\parallel^2\vec{R}_\mathrm{C}\times\vec{B}}{qR_\mathrm{C}^2B^2} \tag{1.12}$$

These drift velocities are charge-dependent and therefore, as can be seen in figure 3, lead to charge separation inside the system, which results in an electric field and a drift velocity $\vec{v}_{E\times B}$ of the whole system [10]

$$\vec{v}_{E\times B} = \frac{\vec{E}\times\vec{B}}{B^2} \tag{1.13}$$

Because the drift would lead to a loss of magnetic confinement, in addition a poloidal magnetic field is superimposed. This means that the magnetic field lines, in addition to the toroidal rotation, obtained a poloidal rotation, i.e. are twisted. Thereby, resulting charge separation can be neutralised immediately and thus drift velocities can be neglected.

In Tokamaks, this additional poloidal magnetic field is generated by toroidal plasma current, e.g. induced by transformer coils. (see Biot-Savart law). In stellarators, this poloidal magnetic field is generated by external stationary magnetic field coils.

This resulting twisting of the magnetic field lines is characterised by the normalised rotational transformation[1] [60]

$$\frac{\iota(r)}{2\pi} = \frac{r}{R}\frac{B_\mathrm{pol}}{B_\mathrm{tor}} = \frac{n}{m} \tag{1.14}$$

[1]The rotational transform ι is also known as safety factor $q = 1/\iota$.

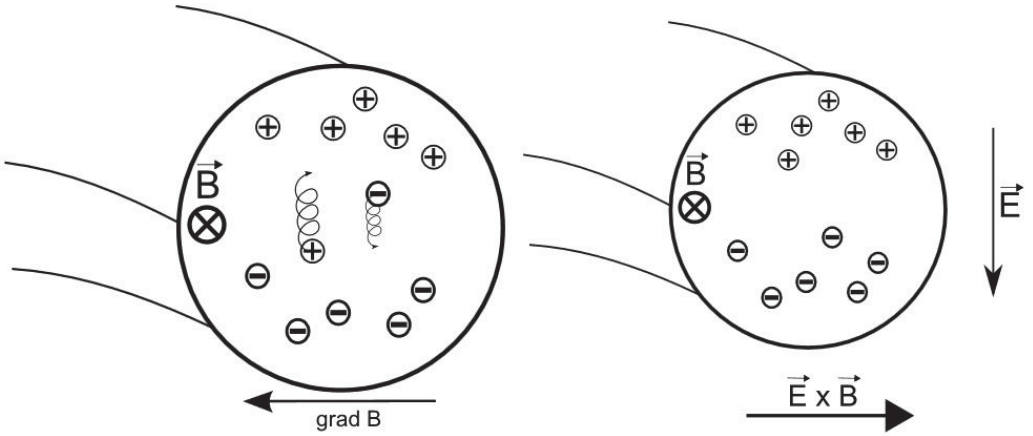

Figure 3: Drift motions by magnetic fields without poloidal component. Magnetic field gradient leads to charge separation. This leads to an electric field and drift. [60]

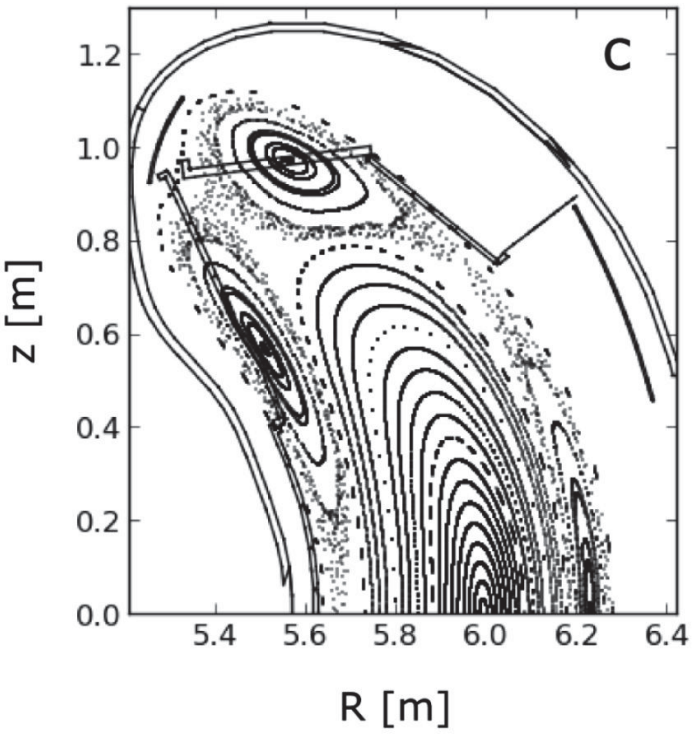

Figure 4: Flux surfaces in poloidal cross-section, represented by intersection points. Disturbances in the magnetic field leads to magnetic islands at resonant values of the rotation transformation. [34]

and indicates how often (n) the magnetic field lines rotate poloidal in m toroidal circulations. The resulting magnetic field lines are not closed for irrational values of the rotational transformation, so thermal charged free particles move on closed flux surfaces, as shown in figure 4.

This magnetically confined plasma can be described by the maxwellian equations and the magnetohydrodynamics (MHD) (chapter 2.2.1):

$$\text{plasma pressure: } J \times B = \nabla p \tag{1.15}$$

$$\text{current density: } \nabla \times B = \mu_0 J \tag{1.16}$$

$$\nabla \cdot B = 0 \tag{1.17}$$

1.2.2 Drift surfaces

The assumption that the particles move along the magnetic field lines is only valid for Larmor radii that are significantly smaller than the plasma radius. This is usually the case for thermal electrons. Due to the higher mass of the ions and therefore larger Larmor radius, this assumption needs to be extended.

The equilibrium of a magnetically confined plasma is given by [25]:

$$\vec{j} \times \vec{B} = \nabla p \tag{1.18}$$

i.e. the particle flux of thermal particles parallel to the magnetic field lines is predominant.

However, thermal and fast particles have non-negligible energies. If these particles move with high velocity in toroidal direction with major radius R, the canonical angular momentum changes [25]:

$$p_\psi = mRv_\psi - q\Psi \tag{1.19}$$

where the magnetic flux is $\nabla\Psi = \vec{B}$.

This leads to a shift of the surface axis and a change of the surface radius by the Grad-Shafranov shift [25]:

$$\Delta = \frac{m v_\psi R_0^2}{2e\Psi\left(R_0\right)} \tag{1.20}$$

With increasing particle energy, the shift also increases. The resulting flux surface is called drift surface.

Furthermore, this shift depends on the direction of the particle movement compared to the magnetic field lines and leads to a separation of flux parallel and anti-parallel to the field lines. For high energies, particles which are parallel and anti-parallel no longer have the same drift surface. For fast ions, this shift is in the order of a few millimetres.

1.2.3 Trapped ions

In a homogeneous magnetic field the particle motion is independent on the position. However, since the fusion devices are toroidally closed and thus circular, an inhomogeneous magnetic field exists. Therefore, the magnetic moment must also be considered.

The magnetic moment of a particle in a magnetic field B is given by [6]:

$$p_\mathrm{B} = \frac{m v_\perp^2}{2B} \tag{1.21}$$

At the same time, the energy conservation is given by [6]:

$$\frac{1}{2m}\left(p_\parallel^2 + p_\perp^2\right) = \text{const.} \tag{1.22}$$

If B increases, e.g. during motion from low field side to high field side of a fusion device, also $v_\perp$ increases and $v_\parallel$ decreases. If the magnetic field reaches $B_\mathrm{T}/B_0 = (v_0^2/v_{\perp 0})$ [6], the parallel velocity becomes zero and the particles will be refelcted and turn back.

As a result, the particle is trapped and will be reflected between both turning points. Thereby, they follow a trajectory, that looks like a banana in poloidal cross-section and is therefore called banana orbit, as shown in figure 5.

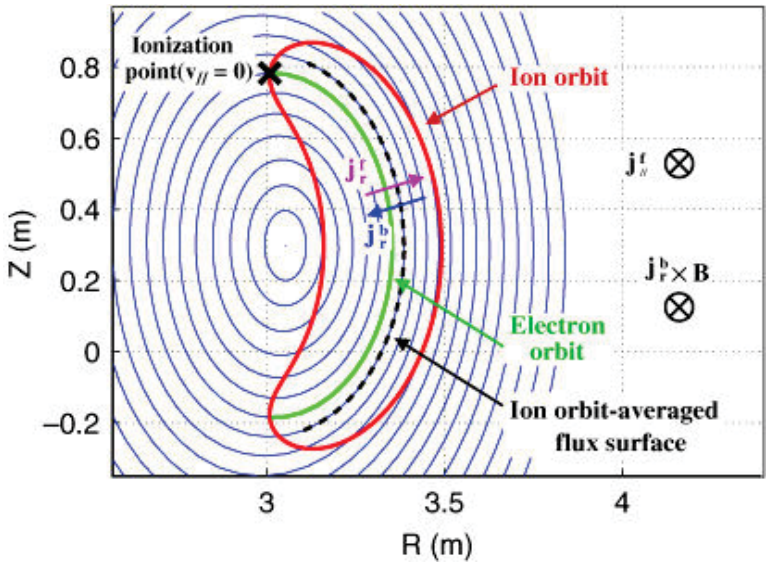

Figure 5: Schematic poloidal cross-section with banana orbit of ions (red) and electrons (green) compared to the magnetic flux surfaces (black) in a tokamak. [63].

The trapped particles are defined by the bounce frequency [70]:

$$\omega_{\mathrm{B}} = \frac{v_{\perp}}{\sqrt{2}qB_0}\epsilon^{\frac{1}{2}} \tag{1.23}$$

and the banana orbit half-width [33]:

$$\Delta r_{\mathrm{B}} = \sqrt{\epsilon}\frac{v_0}{\omega_{\mathrm{C}}} \tag{1.24}$$

Especially for ions, the banana orbit width can become large and therefore also the radial deviation. In this case, the collision of trapped ions leads to a larger radial transport, defined by the so-called banana diffusion coefficient [70]:

$$D_{\mathrm{B}} = \frac{q^2}{\epsilon^{\frac{3}{2}}}D_{\mathrm{classical}} \tag{1.25}$$

1.2.4 Plasma boundary

The perpendicular transport is mostly suppressed by the Lorentz force. Due to several processes like instabilities, turbulence, drifts and collisions, there is still transport perpendicular to the magnetic field lines. This particle transport perpendicular to the magnetic field lines, is by a factor of approx. 10^8 smaller than the transport parallel to the field lines.

Diffusion of magnetically confined particles perpendicular to magnetic field lines leads to a particle and heat transport from inside the plasma to the vessel. The interaction of charged particles can lead to impurities from wall, and damage of vessel components.

The simplest method to reduce the plasma-wall interaction is a so-called limiter (see figure 6). This limiter intersects with magnetic field lines. Flux surfaces without contact to the limiter are called closed, and intersected flux surfaces are called open. As can be seen in figure 6, the last closed flux surface (LCFS), also called Separatrix, separates the confined region from the scrape-off layer (SOL). Thereby, SOL refers to the region of open flux surfaces between the LCFS and wall.

The SOL can be divided into two parts. The inner part, e.g. measurable with our developed RFA probe, with a magnetic field line length in the order of several tens of metres, is defined by quasi-neutrality and collisional transport and is called near SOL. The outer part near the wall forms a positively charged plasma sheath without collisions and is called far SOL.

Because using limiters leads to high flux densities at limiter components, so-called divertors are more common (see figure 6). The first type is a magnetic divertor, where magnetic islands are used for better control of impurities. At Wendelstein 7-X, these islands at plasma edge are produced by the periodicity of the magnetic coil system. Thereby, the last closed surface is located outside the plasma core. This separation leads to a reduced particle and optimised heat transport from the core to the SOL region.

The second type are divertor components located in a wide area at SOL, so that the flux densities are more distributed (see figure 7). At Wendelstein 7-X, these components will be chilled to carry away the heat from the third divertor campaign.

The main difference between limiter and divertor based SOL is the ion and electron source. In the case of the limiter, this particle source is defined by transport from core

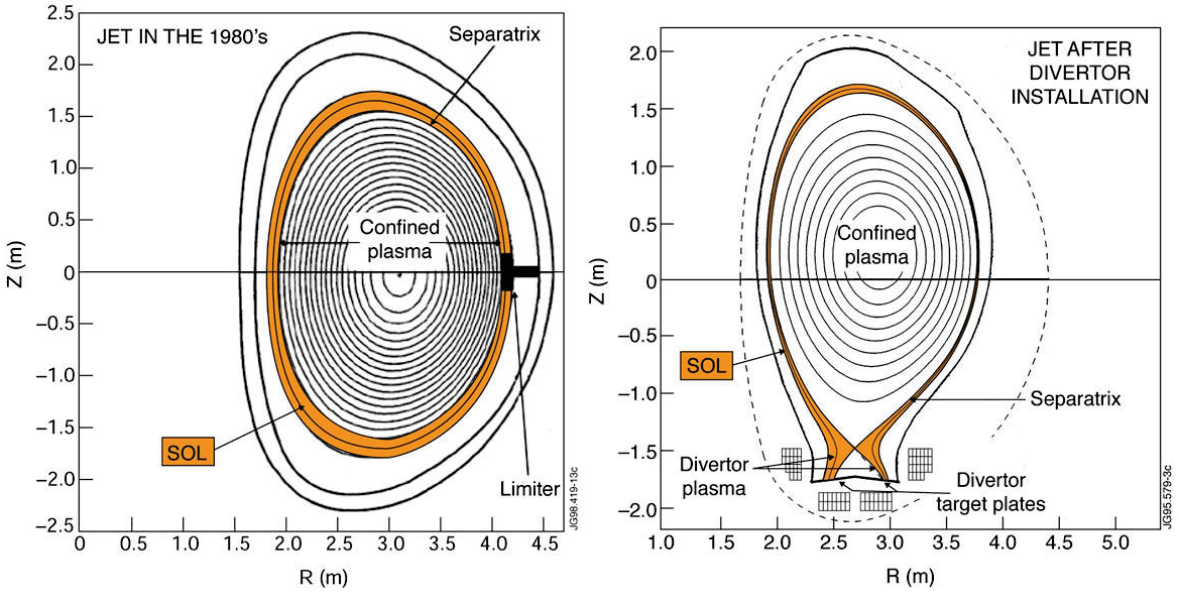

Figure 6: Plasma indicated by confined region with closed flux surfaces and scrape-0ff layer (SOL) with non-closed flux surfaces, separated by separatrix. Left: limiter case, right: divertor case of the JET tokamak. [21]

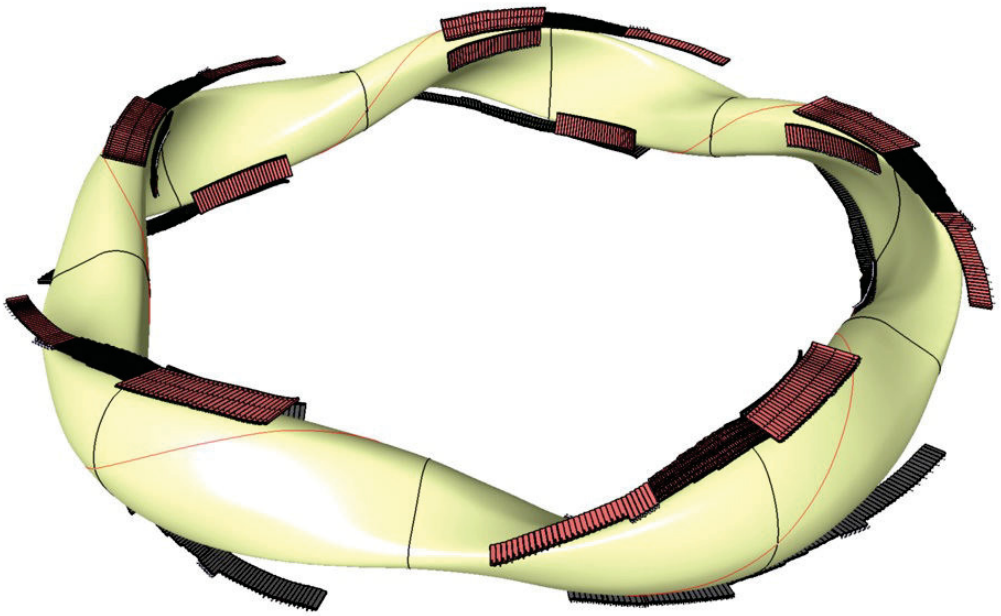

Figure 7: Divertor components (red), plasma (yellow) of the W7-X stellarator. [61]

plasma through the LCFS into the SOL and therefore leads to a relatively simple SOL. On the other hand, in the case of the more complex divertor, plasma recycling at the divertor components is an additional particle source, which leads to a physically and geometrically more elaborated SOL.

The heat source in both cases is given by the heat transport from plasma core through the LCFS and is composed of heating mechanisms and fusion reactions.

1.3 This thesis

1.3.1 Importance of ion temperature measurements

Ion temperature in SOL region is of key importance to modeling different types of plasma-wall interactions, which are important parameters for designing in-vessel components. But instead of the ion temperature most times the electron temperature in the SOL region is measured and assumed that $T_i = T_e$, because there are limited diagnostics available for ion temperature measurements.

Nowadays, the predictive heat flux calculations with numerical codes, like the EMC3-Eirene code, use the electron temperature as input parameter. Although they are able to calculate predictive ion temperatures, the diffusion coefficients are estimated by the electron temperature and usually constant in the SOL region. However, it is known, that such coefficients depend, amongst other things, on the local ion temperatures. Therefore, the heat flux in the SOL region and at divertor modules also strongly depends on the real ion temperature distribution.

In figure 8 it can be seen, that some experiments showed a higher ion temperature than electron temperature in the SOL region. In addition, a few empirical approaches to determine a formula for the ion-electron temperature ratio (e.g. [43], [42], [20]) are given.

Different to electrons, ion temperature can not be measured with the commonly used Langmuir probe, because the measurements would include ions and additionally electrons, due to their lower mass. Therefore, an ion temperature probe called multi-channel retarding field analyzer was investigated, enlarging the already known retarding-field analyzer.

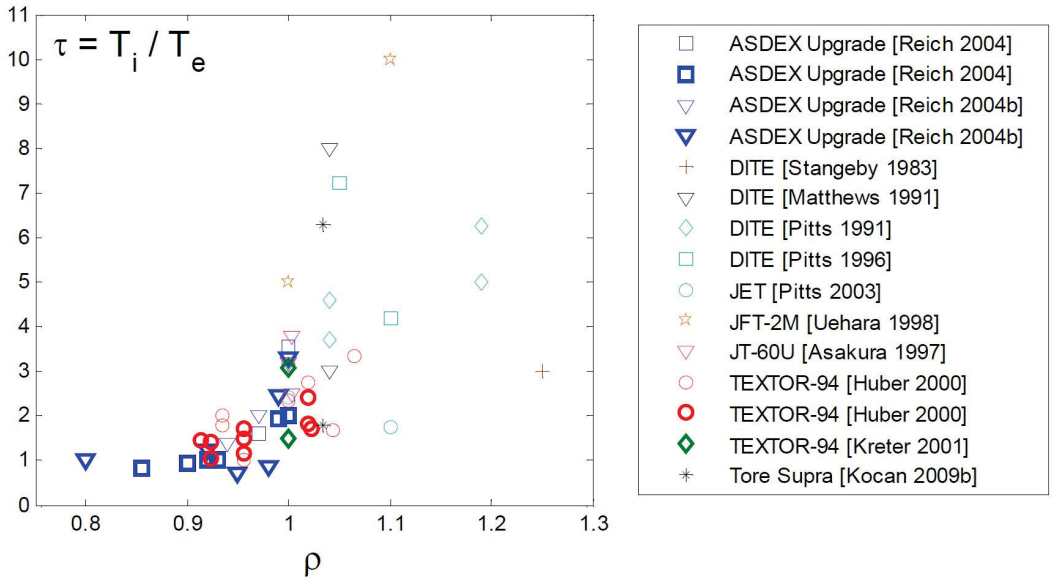

Figure 8: Ion-electron temperature ratio of different experiments plotted over normalised plasma radius. [44]

1.3.2 Development of the multi-channel retarding field analyzer

The design of a single-channel retarding field analyzer (e.g. [50]) has been known for several years. However, array-like measurements for ion temperatures are still not currently availible. Using a multi-channel retarding field analyzer, much more ion related physics can be investigated:

- Simultaneous ion temperature and electron temperature measurements
- Simultaneous measurements of ion temperature fluctuations at different radial position
- Determination of radial fast particle propagation

In chapter 4.1.1, the development of the multi-channel retarding field analyzer is shown. Starting with the basic design and first test in the linear plasma device PSI-2, the feasibility will be shown in chapter 4.1.2. Because previous publications (e.g. [42] showed an influence of the design parameters on the measurements, the dependence of ion sensitivity on the parameters was calculated and is shown in chapter 4.1.2.

In chapter 4.2.1, the commissioning of the probe on the tokamak EAST is shown and supplemented by first measurements of fast particles and ion temperature profiles. The

commissioning of the improved multi-channel retarding field analyzer will be shown in chapter 4.2.2. Further, a list of obstacles which occured, and their solutions will be provided in chapter 4.2.3.

1.3.3 Determination of ion temperatures and fast particle appearance in the SOL region

As previously mentioned, the ions have a key role in various processes. During ELMs in tokamaks for instance, fast ions usually get lost earlier, due to their stronger sensitivity to magnetic perturbations. Indeed, ions have a strong contribution to divertor heat load. However, apppearance and propagation in the SOL region is barely investigated due to limited diagnostics.

Using the retarding field analyzer, fast particles during ELM on the EAST tokamak were measured and shown in chapter 5. First, the plasma conditions and the preceding precursors during experiments will be explained. Afterwards, the appearance and the propation of both fast ions and fast electrons in the plasma core were measured by using neutral particle analyzers and heterodyne radiometers. Furthermore, the propagation of both species were measured, using the retarding field analyzer and divertor Langmuir probes. It will be shown, that fast ions have more localised propagation than fast electrons during the ELM crash. In the last part of chapter 5, an observed postcursor in the fast ion contribution, detected in the plasma core and the SOL region, will be shown.

Furthermore, the ion temperature is of key importance for modelling in the SOL and divertor region. That's why ion temperature measurements were done on the W7-X stellarator. In chapter 6, the plasma conditions and the magnetic edge island topology will be introduced. Although, the so-called standard configuration was used throughout the experiments, the island size could be adjusted using additional control coil currents.

Nowadays, mostly $T_e = T_i$ is used for numerical simulations in the SOL region. However, experiments showed that the ion temperature is higher than electron temperature in the SOL region and differs in the peaking of the profiles inside the edge island. Measurements for different control coil currents are shown in the second part of chapter 6. Further, the interplay between plasma collisionality and ion to electron temperature ratio will be shown in the last part of chapter 6.

Summarised, fast ion and ion temperature measurements with the multi-channel retarding field analyzer were successfully done in the tokamak EAST and the stellarator W7-X.

2 Transport processes in perturbed plasmas

This chapter gives a short summary of the fluid description of plasmas. Further, the transport processes and the evolution of its calculation will be shown.

Mainly, the particles follow the magnetic field lines. Nevertheless, there is perpendicular transport due to different processes. Generally, there are three types of mechanisms, which cause perpendicular transport [19]:

- *Classical: Because there are several particles, they collide jointly with another particle. This leads to a small offset of the momentum and a changed radial position. This mechanism leads to convection and conduction.*
- *Neoclassical: The geometry of the reactor, both stellarator and tokamak, is inhomogenious, which introduces additional effects like banana orbits. This leads to new diffusion effect, which modifies the classical diffusion.*
- *Turbulences: MHD description includes several types of instabilities, which lead to fluctuations in plasmas. This turbulences also lead to radial transport of particles and energy.*

In the first part, specific perturbed field topologies will be introduced. Because perturbed topology has a strong impact on the edge particle and heat transport, the temperature and density in the plasma edge, as well as the confinement, will also be influenced, as shown in chapter 5 and 6.

In the second part, the different transport mechanisms for the different perturbed plasmas will be introduced in more detail.

2.1 Plasma exhaust in perturbed boundaries

In steady-state operation in stellarators and tokamaks, radiation losses and heat power deposition on limiter or divertor targets are equal to the power input defined by the heating power. To achieve such steady-state operation in stellarators and tokamaks, the peak power load value to the limiter or divertor targets has to be reduced. In case of ITER, the external heating power of 40 MW [14] has to be handled in a way that the peak heat load on the target is less than 10 $\mathrm{MW/m^2}$.

For this, two approaches are available. First, the power in the scrape-off layer can be reduced by radiation due to impurities in the plasma edge. Experiments on the ASDEX Upgrade tokamak showed that a reduction of up to 90% can be reached without energy confinement losses in the core plasma [26].

Second, the heat load profile on the limiter or divertor targets can be broadened, so that the peak value decreases. Therefore, usually perturbations in the magnetic field topology or plasma will be used to change the magnetic topology. Thereby, the heat transport is dominated by convective and conductive heat transport. Due to a large anisotropy between parallel and perpendicular heat transport, the radial temperature profile flattens and the peak heat power value decreases. [36]

2.1.1 Resonant magnetic perturbation

As described in chapter 1.2.1, the twisting of the magnetic field lines and therefore the ratio between toroidal B_ϕ and poloidal magnetic field B_θ is given by the rotational transform ι or the safety factor q. If the safety factor q_s of a flux surface becomes rational at minor radius $r = r_\mathrm{s}$, it is called resonant flux surface. In this small layer, the ideal MHD equations used in the bulk plasma have to be replaced by the resistive MHD equations because the resistivity in the resonant flux surface becomes important. [36]

Subsequently, ideal and resistive MHD equations have to match at the boundary of the resonant flux surface. This leads to a discontinuity of the radial derivative of the perturbed poloidal flux Ψ, which is defined by the "tearing stability index" [23]:

$$\Delta' = \left[\frac{1}{\Psi}\frac{d\Psi}{dr}\right]_{r_s^-}^{r_s^+} \tag{2.1}$$

and can be interpreted as degree of available free energy, which starts a growth of a magnetic perturbation. The growth rate $\frac{dw}{dt}$ of the width w of the resulting so-called tearing modes is therefore given by [62]:

$$0.82\tau_{\mathrm{r}}\frac{dw}{dt} = r_{\mathrm{s}}^2\Delta' \tag{2.2}$$

where r_{s} is the minor radius of the non-perturbed resonant flux surface and τ_{r} represents the current diffusion time [62].

Classical tearing modes in the plasma core are already unstable in the linear case. However, in the scrape-off layer boundary they are mostly stable. (see figure 4) [23] A detailed derivation of the arising magnetic islands in stable case is given in [23].

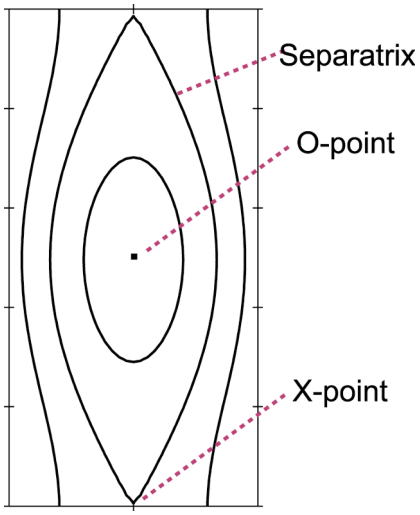

Figure 9: Magnetic island structure in poloidal cross-section with O-point, X-point and separatrix. [37]

As shown in figure 9, the flux surface is replaced by a locally nested flux tube, where the axis of this local flux tube is called O-point. The outermost flux tube, where the flux tubes intersect is called X-point.

The distance between innermost and outermost points in minor radial direction is called island width w and is the stationary stable case of the growth rate $\frac{dw}{dt} = 0$ [36]:

$$w = 4q_{\mathrm{s}}\sqrt{\frac{\Psi}{r_{\mathrm{s}}B_\phi\left[\partial q/\partial r\right]_{\mathrm{r_s}}}} \tag{2.3}$$

The resulting structure connects inner and outer parts of the plasma. On the one hand, the distance between innermost and outermost points of the magnetic island along the magnetic field lines is larger than perpendicular. On the other hand the particle and heat transport along the magnetic field lines is larger than the perpendicular transport. As a result, the radial temperature profile inside the magnetic island becomes flattened.

The degree of flattening is thereby defined by the ratio of island width w, the toroidal mode n (see chapter 1.2.1) and scale island width w_c [36]:

$$w_c = \left(\frac{8 R_o q}{n \left(\partial q / \partial r \right)} \right)^{\frac{1}{2}} \left(\frac{\chi_\parallel}{\chi_\perp} \right)^{-\frac{1}{4}} \tag{2.4}$$

2.1.2 Ergodic magnetic field

As described in chapter 2.1.1, magnetic islands can arise in perturbed magnetic topologies. For magnetic configurations, where various resonant flux surfaces occur in the plasma edge, a so-called ergodic magnetic field can arise.

If the radial distance between two magnetic islands is smaller than the width of both islands together, the outer island flux surfaces intersect. As result, the field lines will be partly destroyed and a chaotic (called ergodic) layer builds up (see figure 10). The degree of the overlap is thereby characterised by the Chirikov parameter, defined by the island widths w and minor radii r of the resonant flux surfaces [12]:

$$\sigma_{\mathrm{Ch}} = \frac{\left(w_1 + w_2 \right) / 2}{r1 - r2} \tag{2.5}$$

Due to the chaotic orientation of the magnetic field lines inside the ergodic layer, the transport parallel to the magnetic field lines also have an influence on the radial transport. For large anisotropies between parallel and perpendicular particle and heat transport, the radial temperature profile also flattens, like in a pure magnetic island.

The temperature profile first flattens in the remaining island structures. If the anisotropy becomes larger, the temperature profile also starts to flatten in the ergodic layer.

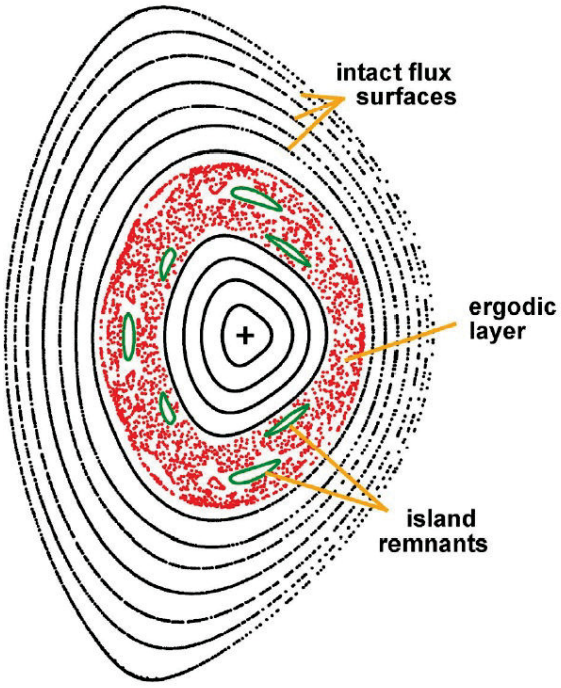

Figure 10: Poloidal plot of an ergodic layer with $\sigma_{\mathrm{Ch}} = 1.6$ produced by overlapping 3/2 and 4/3 magnetic islands in ASDEX Upgrade. [36]

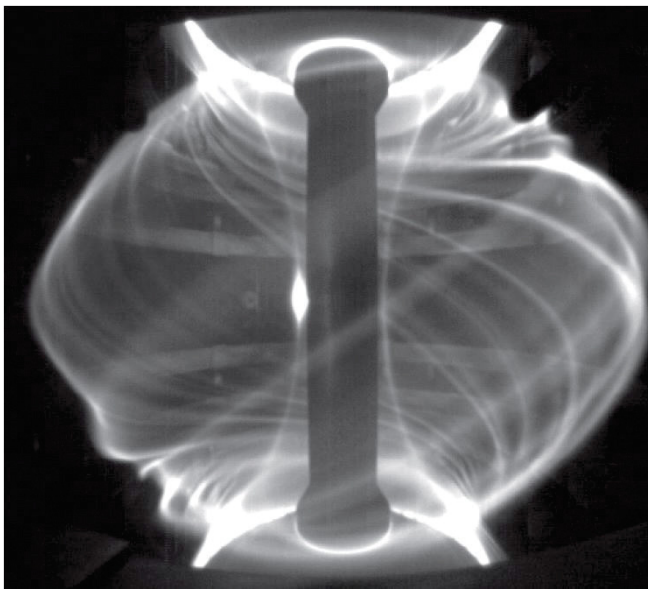

Figure 11: Camera image made during ELM instability in the MAST tokamak. The perturbation leads to plasma filaments, which can be seen. [55]

2.1.3 Edge localised modes

So-called edge localised modes (ELM) typically occur the during high performance operation (H-mode) of a tokamak. Large gradients in pressure, density, temperature or current profiles of H-mode plasmas can drive resonant high mode number MHD instabilities. Mostly, these instabilities are ballooning or peeling modes. A more detailed description can be found in [46].

Whenever the growth of these filaments exceeds the linear MHD limit in in pressure, density, temperature, current, or magnetic field, the instability growth nonlinear until the local confinement collapses. The time delay between start of the ELM and maximum temperature is in the order of 100 µs and described by the so-called heat flux rise time [46]:

$$\tau_{\parallel} = \frac{2\pi q_{95} R}{\sqrt{\left(T_e + T_i\right)/m_i}} \tag{2.6}$$

After the collapse, the profiles flatten due to the losses. Afterwards, the mode can grow again. A fraction of the ELM energy becomes free after the collapse and propagates outwards through the scrape-off layer. Additionally, particle confinement becomes lost, and fast particles propagate through the scrape-off layer.

Mostly, not only a single mode arises, but a more complex system given by a set of toroidal mode numbers between five and fifteen [46]. Such an ELM system is called ELM filamentary and can be measured in the scrape-off layer and divertor by a temporary temperature, density or current increase (see figure 11).

2.2 Transport processes

2.2.1 Plasma as fluid

A usual way to describe plasma is the so-called fluid description, where infinite small cells with a single particle probability distribution function $f\left(v, r, t\right)$ of particle velocity v, position r and time t were used.

The basic balance equation for so-called magneto-hydro-dynamic (MHD) plasmas is the time derivation of the distributed particles. Because of particle conservation, the

absolute derivative is ideally zero, so the Boltzmann equation is given by:

$$\frac{df}{dt} = \frac{\partial f}{\partial t} + \nabla_x f \frac{dx}{dt} + \nabla_v f \frac{dv}{dt} = 0 \tag{2.7}$$

For general particle motion is $dx/dt = v$ and for simplicity, particles will be forced only by electromagnetic field. Because plasma systems are not ideal, there are losses by collisions. Therefore, the continuity equation can be derived from equation 2.7:

$$\frac{\partial f}{\partial t} + \vec{v}\nabla_x f + \frac{q}{m}\left(\vec{E} + \vec{v} \times \vec{B}\right) \nabla_v f = \left(\frac{\partial f}{\partial t}\right)_{collision} \tag{2.8}$$

For momentum conservation, the continuity equation can be developed for ion-electron collisions $\sim mv$ and their frequency $\sim n\nu_m$ [40]:

$$mn\left(\frac{\partial v}{\partial t} + (\vec{v}\nabla)\,\vec{v}\right) = nq\vec{E} - \nabla p - m\vec{v}n\nu_m \tag{2.9}$$

This distribution can be used to calculate quantities like particle density n, fluid velocity $\vec{u}$ and temperature T to simplify the evolution equations. The so-called moments of the particle distribution function f are defined by:

$$n = \int f\,(\vec{v})\; d^3v \tag{2.10}$$

$$\vec{u} = \frac{1}{n}\int \vec{v} f\,(\vec{v})\; d^3v \tag{2.11}$$

$$T = \frac{1}{n}\frac{m}{3}\int (v-u)^2\, f\,(\vec{v})\; d^3v \tag{2.12}$$

By using these moments of the distribution function and integrating the Boltzmann equation (equation 2.7), the particle balance equation is given by [30]:

$$\frac{\partial n}{\partial t} + \nabla\,(nv) = S_{an}^{ie} \tag{2.13}$$

where S_{an}^{ie} are the particle sinks and sources by ionisation or neutralisation.

The momentum balance equation is given by [30]:

$$\frac{\partial}{\partial t}\left(mnu\right) + \nabla\left(mnu^2 + P\right) = S^{\mathrm{F}}_{\mathrm{amV}} + S^{ee}_{\mathrm{amV}} + S^{ei}_{\mathrm{amV}} \tag{2.14}$$

where S^{ee}_{amV} and S^{ei}_{amV} are sources and sinks by collisions and $S^{\mathrm{F}}_{\mathrm{amV}}$ by other forces. The pressure tensor P is defined by the viscosity tensor[2] Π and the scalar pressure p and can be calculated by [30]:

$$p = nT \tag{2.15}$$

$$\Pi = mn\left[\left\langle v^2\right\rangle - \frac{1}{3}\left\langle v^2\right\rangle I\right] \tag{2.16}$$

$$P = pI + \Pi \tag{2.17}$$

The energy balance equation is given by [30]:

$$\frac{\partial}{\partial t}\left(\frac{3}{2}nT + \frac{1}{2}mnu^2\right) + \nabla\left(\frac{5}{2}nTu + \frac{1}{2}mnu^2u + q + v\Pi\right) = S^{\mathrm{F}}_{\mathrm{aE}} + S^{\mathrm{ee}}_{\mathrm{aE}} + S^{\mathrm{ei}}_{\mathrm{aE}} \tag{2.18}$$

where $S^{\mathrm{F}}_{\mathrm{aE}}$, $S^{\mathrm{ee}}_{\mathrm{aE}}$ and $S^{\mathrm{ei}}_{\mathrm{aE}}$ are energy sinks and losses, and can be used to calculate plasmas.

The heat flux density q is defined by [30]:

$$q = \frac{mn}{2}\left\langle v^3\right\rangle \tag{2.19}$$

Due to large transport along the magnetic field lines, the density and temperature distribution follow the topology instantaneously. That's why stationary case is reasonable and the time derivation can be neglected. In this case, the plasma current density can be described by [40]:

$$\vec{j} = \frac{en}{m\nu_{\mathrm{m}}}\vec{E} - \frac{k_BT}{m\nu_{\mathrm{m}}}\nabla n \tag{2.20}$$

for high collisionality $\nu_{\mathrm{m}} \gg \nu$, where ν^2 term is neglected and adiabatic plasma $\nabla p/p \sim \nabla n/n$ is assumed.

[2] v_iv_j are two arbitrary vectors given by the dyadic product $v_iv_j = v^iv^je_ie_j$ and $\langle ...\rangle$ is an averaging operator like the moments of f

The first term is driven by an electric field, p.e. produced by charge separation. Generally, this term is small in near SOL compared to the second term, which is driven by the density gradient.

Because the plasma is quasi-neutral, the E-term of equation 2.9 can be neglected in first order. In this case, the force equation is given by [3]

$$mn\frac{du}{dt} = -\nabla p + j \times B = 0 \tag{2.21}$$

This equation defines the change of fluxes and therefore needs, in addition to the current density, information about the magnetic field. For this, the low frequency case of the maxwellian equations is suitable, which is given for slow E changes.

$$\nabla B = \mu_0 j + \epsilon_0 \mu_0 \frac{\partial E}{\partial t} \approx \mu_0 j \tag{2.22}$$

Using the equations 2.20 to 2.22, the confined plasma, more precisely the magnetic field, current density and pressure, can be described.

To also describe the binding forces from the magnetic field to the plasma, the so-called plasma pressure is used. This magnetic pressure can be derived by combining equation 2.21 and equation 2.22 and is given by [66]:

$$p_{\mathrm{mag}} = \frac{B^2}{2\mu_0} \tag{2.23}$$

To define the pressure and power of of the plasma relative to the magnetic field strength, the so-called relative pressure β was introduced, which is the ratio of thermal pressure and magnetic pressure [66]:

$$\beta = \frac{p_{\mathrm{th}}}{p_{\mathrm{mag}}} = p_{\mathrm{P}} B^2 / 2\mu_0 \tag{2.24}$$

Derivations of further MHD equations can be found in several other publications. (e.g. [3])

2.2.2 Scrape-off layer transport in limiter configuration

If there are no particle sources or sinks, the particle flow perpendicular to the magnetic field lines into the SOL is balanced by the parallel particle losses at limiter. [44]

$$L_{\parallel}\frac{d}{dr}\Gamma_{\perp} \approx \Gamma_{\parallel} \tag{2.25}$$

where $L_{\parallel}$ is the magnetic connection length and $\Gamma_{\parallel} \sim nv_{\parallel}$. The cross field particle diffusion coefficient $D_{\perp}$ is defined by [44]

$$\Gamma_{\perp} = -D_{\perp}\frac{dn}{dr} \tag{2.26}$$

Considering sources and sinks within the SOL, like ionisation and recombination and $S_{\mathrm{iz}} \gg S_{\mathrm{rec}}$, the particle conservation equation $\nabla\Gamma = S = S_{\mathrm{iz}} - S_{\mathrm{rec}}$ leads to an advanced equation 2.25 [24]:

$$\lambda_{\Gamma} = \frac{\Gamma_{\perp}}{S_{\mathrm{iz}} + \Gamma_{\parallel}/L_{\parallel}^{\mathrm{iz}}} \tag{2.27}$$

and

$$L_{\parallel}^{\mathrm{iz}} \equiv \left(\int_0^{L_{\parallel}} S_{\mathrm{iz}} s_{\parallel} ds_{\parallel}\right) / \left(\int_0^{L_{\parallel}} S_{\mathrm{iz}} ds_{\parallel}\right) \tag{2.28}$$

In the case of such volumetric sources, the connection length will be replaced by the ionisation-weighted length. Moreover, there is an additional term for parallel transport and leads to a reduction of λ_{Γ} [24]. When $S_{\mathrm{iz}} \ll n/\tau_{\parallel}$ equation 2.28 approaches again to the simpler equation 2.25.

If, for simplicity, it is assumed that $L_{\parallel}$, $v_{\parallel}$ and $D_{\perp}$ are independent of minor radius r, the density distribution can be described by [44]

$$n\,(r) \approx n_{\mathrm{LCFS}} \cdot \exp\left(-\frac{(r-a)}{\lambda_n}\right) \tag{2.29}$$

where n_{LCFS} is the density at the last closed flux surface and λ_n the density e-folding length.

For energy balance equation, equally T_i is obtained by [44]:

$$T(r) \approx T_{\mathrm{LCFS}} \cdot \exp\left(-\frac{(r-a)}{\lambda_T}\right) \tag{2.30}$$

The corresponding particle flux and heat flux decay lengths are defined by [15]:

$$\lambda_\Gamma = \frac{1}{(1/\lambda_n + 0.5/\lambda_T)} \tag{2.31}$$

$$\lambda_q = \frac{1}{(1/\lambda_n + 1.5/\lambda_T)} \tag{2.32}$$

Thereby, the heat transport coefficient can be determined by [44]

$$D_\perp = \frac{\lambda_n^2 v_\parallel}{L_\parallel} \tag{2.33}$$

To describe this diffusion coefficient, many different approaches have been made in the past. The most important ones are briefly presented here.

The so-called classical transport is caused by collisions of the gyrating particles. The time step of the diffusion is given by the collision frequency $\Delta t = 1/\nu$ and step length is given by gyration radius r_L. If random walk is then assumed, a diffusion coefficient is given by [19]:

$$D = r_\mathrm{L}^2 \nu \tag{2.34}$$

The collision frequency thereby is defined by [7]:

$$\nu_i = \frac{\nu_e}{\sqrt{2}} = \frac{\ln \Lambda e^4 n}{12\pi^{3/2}\epsilon_0^2\sqrt{m}T^{3/2}} \tag{2.35}$$

The so-called coulomb logarithm is the logarithmic ratio of minimum distance between particles given by the repulsive field between particles and particle energy and the debye length.

To estimate the ratio between particle losses caused by intersected field lines and by diffusion, the dimensionless parameter plasma collisionality ν^* is defined [58]:

$$\nu^* = \frac{\text{connection length}}{\text{trapped particle mean free path}} \tag{2.36}$$

$$= \nu_i \left(\frac{m_i}{T_i}\right)^{1/2} L_\parallel \tag{2.37}$$

The plasma collisionality indicates which transport process in the scrape-off layer dominates. For $\nu^* < 10$ the convective transport dominates, for $\nu^* > 10$ the conductive transport dominates. (see chapter 2.2.3)

There are also other drive mechanisms like magnetic or electric fields, and density or temperature gradients, which could lead to diffusion. For the isothermal case, described by equation 2.20, the mobility given by the electric field driven term is [40]:

$$\mu_\parallel = \frac{|q|}{m\nu_\mathrm{m}} \tag{2.38}$$

and the diffusion coefficient given by the density gradient driven term is [40]:

$$D_\parallel = \frac{k_B T}{m\nu_\mathrm{m}} \tag{2.39}$$

In this case, perpendicular particle flux is given by the parallel particle losses caused by electron-ion collisions. Therefore, the mobility perpendicular to the magnetic field lines is given by [40]:

$$\mu_\perp = \frac{\mu_\parallel}{1 + \omega_\mathrm{C}^2 \tau^2} \tag{2.40}$$

and therefore

$$D_\perp = \frac{D_\parallel}{1 + \omega_\mathrm{C}^2 \tau^2} \tag{2.41}$$

The fact that $\Gamma_\perp \ll \Gamma_\parallel$ is given, shows that the SOL is defined by thin flux layers and its is decay mostly defined by the ratio of perpendicular and parallel particle transport.

If a strong magnetic field $\omega^2\tau^2 \gg 1$ is assumed, the perpendicular diffusion is approximated by [40]:

$$D_\perp = \frac{k_\mathrm{B}T}{m\nu_\mathrm{m}} \cdot \frac{\nu_\mathrm{m}^2}{\omega_\mathrm{C}^2} \sim \frac{\nu_\mathrm{m}}{B^2} \tag{2.42}$$

However, this would result in a faster decay of the electrons, because of the higher mobility. The arising electric field leads to a counteracting force, which maintains the quasi-neutrality. The resulting so-called ambipolar diffusion is defined by [24]:

$$D_\mathrm{amb} = \frac{\mu_i D_e + \mu_e D_i}{\mu_i + \mu_e} \tag{2.43}$$

Because generally $\mu_e \gg \mu_i$ is given, the ambipolar diffusion can be described by [24]:

$$D_\mathrm{amb} = D_i \left(1 + \frac{T_e}{T_i}\right) \tag{2.44}$$

However, experiments in the past shown a B^{-1} dependence instead of the derived B^{-2} dependence of the diffusion coefficient. Likewise, the range of $D \sim 10^{-3} m^2/s$ does not fit with measured diffusion coefficients. So more complex diffusion processes had to be found. The so-called Bohm diffusion coefficient can be described by [4]:

$$D_\perp = D_\mathrm{Bohm} = \frac{1}{16}\frac{k_B T}{qB} \tag{2.45}$$

The Bohm diffusion coefficient has a value of $\sim 1 m^2/s$ for modern stellarators and tokamaks and still matches with simulations of SOL plasma.

However, classical transport can not explain the diffusion coefficient measured in experiments. That is why diffusion of trapped particles (called neoclassical transport) will be included in the next step. As described in [19], charged particles can be trapped in low magnetic field strength between two high field parts. There, such particles move on so-called banana-orbits, which have a significantly larger radial extent than gyration. In this case, the step width in diffusion is defined by the banana orbit width w_B and the time step is defined by the collision frequency ν_eff, for collisions, where

trapped particles change $v_\perp/v_\parallel$ in such a way, that they are no longer trapped. Thus, the neoclassical diffusion coefficient is given by [19]:

$$D_{\text{neo}} = \frac{q^2}{\epsilon^{3/2}} D_{\text{class}} \tag{2.46}$$

with the safety factor $q = 1/\iota$ and aspect ratio $\epsilon = R/r$.

Superposed to this diffusion caused by collisions, there are diffusion processes caused by turbulences. Small fluctuations in temperature, density, or the magnetic or electric field lead to diffusion processes like electrostatic (ES) and electromagnetic (EM) processes, which can be estimated by [24]:

$$\Gamma_\perp^{\text{ES}} = \langle n v_\perp \rangle = \frac{\left\langle n \tilde{E}_\wedge \right\rangle}{B} \tag{2.47}$$

$$\Gamma_\perp^{\text{EM}} = \frac{\left\langle \tilde{n} c_{\text{s}} \tilde{B}_\perp \right\rangle}{B} \tag{2.48}$$

where the tilde values are fluctuation quantities (p.e. $\tilde{T} = T - \langle T \rangle$).

In the following table some typical values of the different kinds of diffusion coefficients for EAST and W7-X cases are given.

type	D [m^2/s]
classical	$\sim 10^{-4}$
neoclassical	$\sim 10^{-3}$
Bohm	$\sim 10^{0}$
EM/ES turbulence	$\sim 10^{1}$

Table 1: Perpendicular particle flux for typical SOL plasma parameters

As shown in table 1, the particle transport perpendicular to the magnetic field lines is underestimated by classical and neoclassical diffusion coefficients. The Bohm diffusion coefficient is in the order of the measured values, it is simply empirical. The largest contribution to the perpendicular diffusion of the SOL region is given by turbulences.

2.2.3 Scrape-off layer transport in divertor configuration

Due to the fact that the magnetic connection length at divertor is dependent on the minor radius r in the SOL in the divertor configuration used on W7-X, the previous approximation for limiters is not accurate enough. For this reason, a more accurate description for the SOL region is needed.

Generally, the energy balance equation of a plasma is given by [68]:

$$\frac{\partial}{\partial t}\frac{3}{2}nT + \nabla\left(\frac{5}{2}T\Gamma + \vec{q}\right) = \vec{u}\nabla p \tag{2.49}$$

where Γ is the particle flux density, $\vec{q}$ the heat flux density, $\vec{u}$ the flux velocity and p the plasma pressure.

For a fully ionised plasma with single ion species the heat flux density can be described by [7]:

$$q = -\chi_{\parallel}\nabla_{\parallel}T - \chi_{\perp}\nabla_{\perp}T + \frac{5}{2}\frac{cnT}{ZeB^2}\vec{B}\times\nabla T \tag{2.50}$$

under the condition $\omega\tau \gg 1$.

The first term describes the parallel and the third term the poloidal heat transport. Because the heat conductivity parallel and perpendicular to the magnetic field lines are driven by different physical processes, the parallel component $\chi_{\parallel}$ is typically 10^6 up to 10^{10} times higher [24] than the perpendicular component $\chi_{\perp}$.

The parallel heat conductivity is thereby given by the Spitzer-Härm expression [24]:

$$\chi_{\parallel} = 3.2 v_{\mathrm{te}}\lambda_e \sim L_{\parallel} v_{\mathrm{te}}/\nu_e^* \tag{2.51}$$

where $v_{\mathrm{te}} = \sqrt{k_{\mathrm{B}}T/m}$ is the electron thermal velocity, $\lambda_e = v_{\mathrm{te}}\tau_e$ is the electron-ion-collisional mean-free-path and ν^* the electron collisionality, where $\nu^* = L_{\parallel}/\lambda_e$ is typically in the range of $10 - 100$ in the near SOL.

For far SOL case ($\nu^* < 10$), the heat transport is not longer defined by the conductive transport, but by convective transport, where the heat transport is carried by the particle transport.

Because it is only possible to measure radial and thereby only perpendicular ion temperature distributions with the midplane manipulator probe, the second term of equation 2.50 is investigated in this work. In this way, the equation can be simplified to:

$$q = -\chi_\perp \nabla_\perp T \tag{2.52}$$

where the thermal conductivity for ions is defined by [7]:

$$\chi_\perp = 2\frac{n_i T_i}{m_i \omega_i^2 \tau_i} \tag{2.53}$$

with confinement time τ and gyration frequency ω.

The temperature decay length thereby is defined by the confinement time in a flux surface and perpendicular velocity. Although, the particle transport and the heat transport are clearly decoupled in the scrape-off layer plasma (see chapter 1.2.4), assuming advective transport $v_{\perp n} = v_{\perp T}$ leads to a correlation between both decay lengths [24]:

$$\frac{\lambda_n}{\lambda_T} \approx \frac{\tau_{\parallel n}}{\tau_{\parallel T}} \approx \frac{\chi_\parallel}{c_\mathrm{s} L_\parallel} \approx \left(\frac{T_e}{T_i}\frac{m_i}{m_e}\right)^{\frac{1}{2}} \frac{1}{\nu^*} \tag{2.54}$$

Superposed to the conductivity driven heat transport, there are turbulence driven heat transport processes like electrostatic and electromagnetic processes, which can be estimated by [24]:

$$q_\perp^{\mathrm{ES}} = \frac{3}{2} T \Gamma_\perp^{\mathrm{ES}} + \frac{3}{2} n \frac{\left\langle \tilde{T}\tilde{E}_\wedge \right\rangle}{B} = \frac{3}{2} \left\langle n T v_\perp \right\rangle \tag{2.55}$$

$$q_\perp^{\mathrm{EM}} = \frac{5}{2} T \frac{\left\langle \tilde{n} c_s \tilde{B}_\perp \right\rangle}{B} - q_\parallel \left\langle \frac{\tilde{B}_\perp^2}{B^2} \right\rangle \frac{L_\parallel}{\lambda_T} \tag{2.56}$$

To understand the heat and particle flux and its interplay with magnetic topology is one of the significant tasks for future power plants.

2.2.4 Transport processes in stochastic layers

As introduced in chapter 2.1.2, a stochastic layer can arise caused by the overlapping of two magnetic islands or can be driven by dynamic processes such as ELM. The chaotic trajectories in ergodic layers result in a parallel contribution to the radial heat transport, which increases the radial diffusion due to the significantly higher parallel transport.

More detailed descriptions can be found in [39], [67] and [45], in which three collisional subregimes were identified. They are defined by the characteristic electron diffusion times:

$$\tau_{\parallel} = L_0^2/\chi_{\parallel} \tag{2.57}$$

$$\tau_k = L_k^2/\chi_{\parallel} \tag{2.58}$$

$$\tau_{\perp} = 1/\left(k_{\perp}^2\chi_{\perp}\right) \tag{2.59}$$

The corresponding characteristic lengths for a m/n magnetic perturbation are defined by [45]:

$$L_0 \approx qR_0 \tag{2.60}$$

$$L_k \approx \left[L_S^2/\left(k_{\perp}^2 D_M\right)\right]^{1/3} \tag{2.61}$$

$$D_M = L_0 \sum_{m,n} \left(B_{r,m/n}/B_{\phi}\right)^2 \tag{2.62}$$

$$k_{\perp} \approx m/r \tag{2.63}$$

$$L_S = q^2/\left(r\partial q/\partial r\right) \tag{2.64}$$

where $B_{r,m/n}$ is the radial component of the perturbation, D_M the magnetic diffusion coefficient and $k_{\perp}$ the perpendicular wave vector. The different regimes can thereby divided into [45]:

$$\text{fluid regime (fl)} : \tau_{\perp} < \tau_{\parallel} < \tau_k \tag{2.65}$$

$$\text{Kadomtsev-Pogutse regime (KP)} : \tau_{\parallel} < \tau_{\perp} < \tau_k \tag{2.66}$$

$$\text{Rechester-Rosenblith regime (RR)} : \tau_{\parallel} < \tau_k < \tau_{\perp} \tag{2.67}$$

The increase χ_r^+ of the radial heat diffusivity without stochastivity $\chi_r = \chi_\perp + \chi_r^+$ is [45]:

$$\chi_{r,fl}^+ = D_M \chi_\parallel / L_0 \tag{2.68}$$

$$\chi_{r,KP}^+ = D_M \left(\chi_\perp \chi_\parallel\right)^{1/2} k_\perp \tag{2.69}$$

$$\chi_{r,RR}^+ = D_M \chi_\parallel / L_k \tag{2.70}$$

This increase in the radial diffusivity leads to a flattening in the density and temperature profile. Therefore, ergodic layers are a promising method for future devices, to distribute the heat load and protect the divertor modules.

2.3 Heat transport in magnetic edge islands

As mentioned in chapter 2.1.1, the scale island width w_c is a key value to determine the radial heat transport through the edge island.

For high a parallel diffusion coefficient, the parallel transport domintes. In this case, the heat propagates from the inner to the outer separatrix by parallel transport along the magnetic field lines. Afterwards, the heat will be transported from the separatrix to the O-point slower. In such a case, definied by $\frac{w}{w_\mathrm{c}} < 1$, the temperature profile is usually peaking at the edge island structure.

For this case, the increase of the radial heat diffusivity $\kappa = \left(\chi_r - \chi_\perp\right)/\chi_\perp$ was eximinated by [35] with:

$$\kappa \sim \left(\frac{w}{w_\mathrm{c}}\right)^4 \tag{2.71}$$

Whereas, the heat transport for $\frac{w}{w_\mathrm{c}} > 1$ was examinated with:

$$\kappa \sim \left(\frac{w}{w_\mathrm{c}}\right)^2 \tag{2.72}$$

In this case, the perpendicular heat transport is stronger and the radial transport across the edge island is dominated by a diffusion from the inner separatrix, across the O-point, to the outer separatrix. In this regime, a significant flattening of the temperature profile can be found, as shown in figure 12.

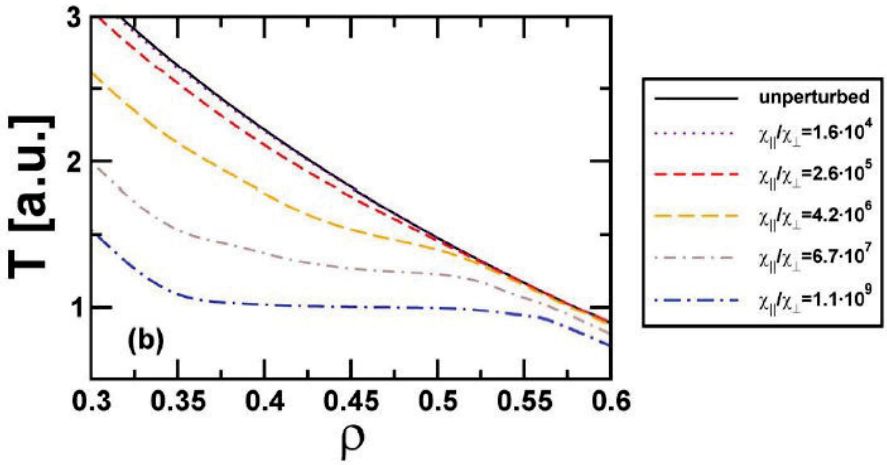

Figure 12: Radial profiles of the poloidally and toroidally averaged temperature distribution within an magnetic island for different anisotropies. [36]

3 Utilised fusion devices and diagnostics

This chapter focuses on the fusion devices, which were used for the retarding field analyzer experiments in chapter 5 and 6.

In the first part, both devices will be introduced and the respective advantages will be shown. The EAST tokamak is a midsize tokamak, which is suitable for edge localised plasmas and investigations of particle confinement during ELM. On the other hand, the stellarator W7-X is most suitable for measurements of the of edge topology on plasma parameters, due to the static edge islands.

In the second part, available edge diagnostics will be explained and the importance of developing an ion diagnostic will be shown. Therefore, the different methods of density and temperature profile measurements will be described.

In the last part, two diagnostics for fast particles will be briefly explained. Especially for the experiments in chapter 5, these diagnostics are essensial because the appearance of fast particles after an ELM crash indicates the confinement of fast ions in ELMy plasmas.

3.1 Fusion devices

In fusion plasma research there are usually two types of devices, called tokamak and stellarator. To investigate the interplay between the particle and heat transport, and magnetic topology in the SOL region, measurements on the tokamak EAST in Hefei (China) and on the stellarator W7-X in Greifswald (Germany) were done. Both devices are described below.

3.1.1 EAST

The experimental advanced superconducting tokamak (EAST), is a steady-state-capable device for high temperature fusion plasma research which began operating in 2006. It is the first tokamak with fully superconductive magnetic field coils and is used to accomplish a scientific and technological basis for fusion power plant tokamaks.

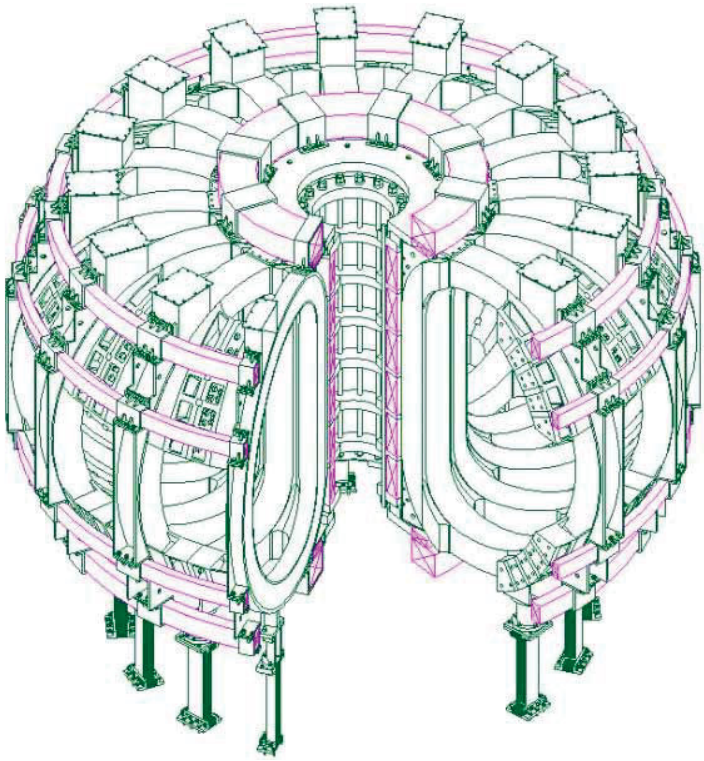

Figure 13: Magnetic coils system of EAST: D-shaped toroidal coils (green), poloidal and central solenoidal coils (purple). [57]

major radius:	1.85 m
minor radius:	0.45 m
magnetic field:	3.5 T
toroidal current:	1.0 MA

Table 2: Technical specifications of EAST

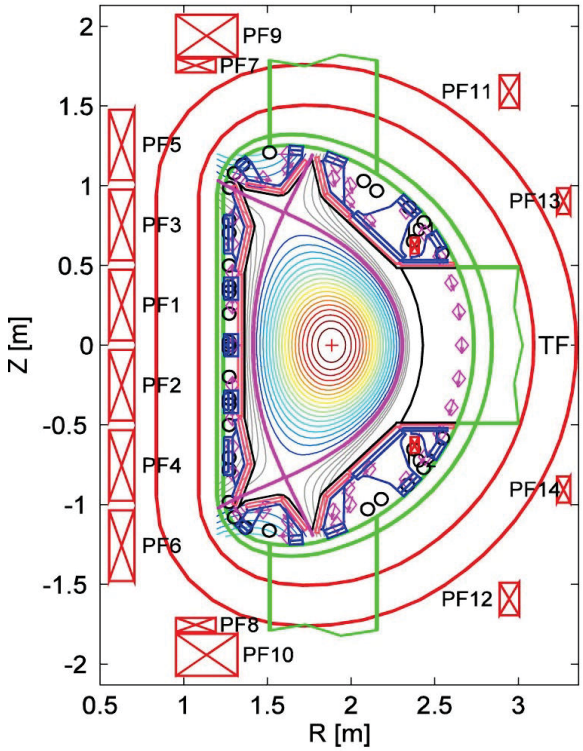

Figure 14: Magnetic field cross-section at double-null-configuration at EAST. core plasma (colored flux surfaces), separatrix (purple), SOL (gray flux surfaces) [11]

As shown in figure 13, the magnetic coil system of EAST consists of two coil subsystems. The toroidal magnetic field inside the tokamak is produced by 16 superconductive D-shaped coils. Additionally, there is a second set of 6 vertical and 6 central solenoid superconductive coils, to produce a non-conductive poloidal magnetic field. The technical specifications of EAST are given in table 2.

Similar to most tokamaks, EAST is approximately a 2D magnetic field system. The poloidal magnetic field cross-section is independent on the toroidal position, as shown in figure 14. The toroidal magnetic field is given by the coils, whereas the poloidal magnetic field component is partly induced by the toroidal plasma current.

As shown in figure 14, the SOL region of EAST is defined by magnetic divertors. In single null configuration, one additional superconductive coil is located above or below the plasma vessel (in double null configuration both coils). This leads to a so-called separatrix, meaning that there is a self-intersecting flux surface which divides the plasma into confined region and SOL region.

The magnetically confined plasma can be heated by electron cyclotron resonance heating (ECRH) on 60, 110 and 118 GHz up to 0.5 MW [74], ion cyclotron radio-frequency heating (ICRF) in a range of 25 MHz to 70 MHz up to 12.0 MW [73], lower hybrid current drive (LHCD) at 2.45 GHz up to 2.0 MW and 3.75 GHz up to 1.5 MW [27] or by neutral beam injection (NBI) up to 4.0 MW heating power. Throughout the experiments, pure deuterium plasmas were used.

Due to intensive studies of resonant magnetic perturbed plasmas at EAST (e.g. [69]), it is particularly suitable for investigations of the influence of magnetic field topology on the plasma wall interactions.

3.1.2 W7-X

The stellarator Wendelstein 7-X (W7-X), from the group of optimised stellarators, started operation in december 2015 and allows to draw conclusions about the suitability of power plant stellarators. W7-X is a helical-axis advanced stellarator and aims at steady state operation with reactor relevant plasma collisionallity and plasma β.

As shown in figure 15, the magnetic coils system of Wendelstein 7-X consists of two coil systems. The helical magnetic field inside the Stellarator is produced by 40 nonplanar 3D superconductive coils, optimised for stable and heat insulting magnetic confinement.

Figure 15: Magnetic coils system of W7-X: optimised helical coils (blue) and additional coils (red) for adapting the magnetic field. [52]

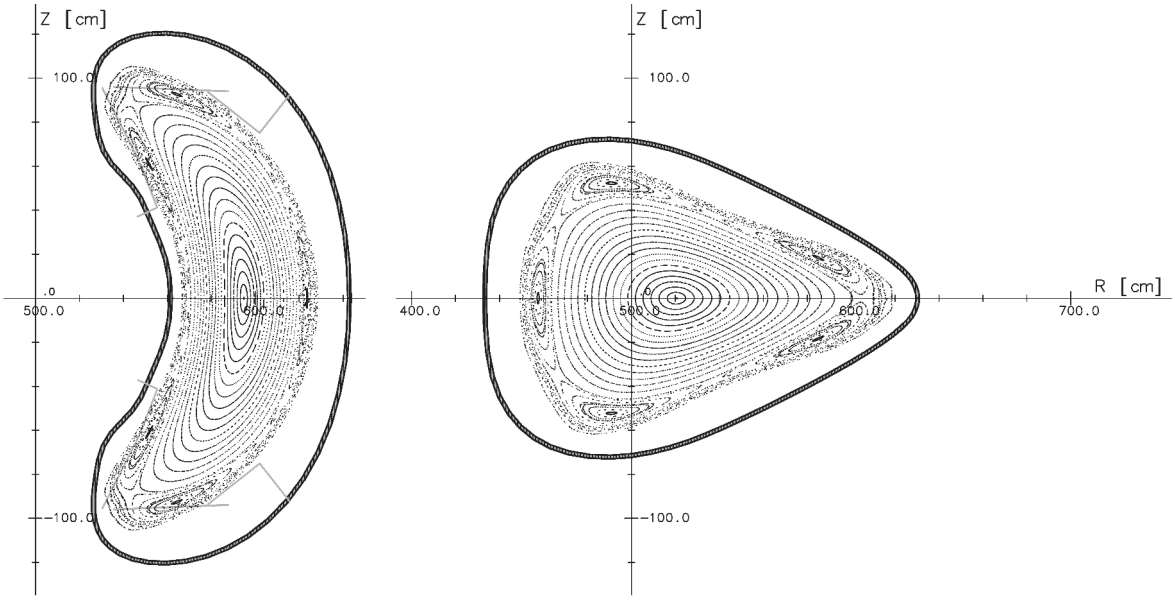

Figure 16: Magnetic field cross-section at 5-periodic turning points at W7-X. left at $\phi = 0°$ and right at $\phi = 36°$. [2]

major radius:	5.5 m
minor radius:	0.53 m
magnetic field:	3 T
plasma volume:	30 m^3

Table 3: Technical specifications of W7-X

In order to vary the magnetic field, a second set of 20 planar superconductive coils is superposed.

W7-X started as limiter based device for the first campaign with non-circular magnetic field cross-sections and was upgraded to a non-cooled island divertor based stellarator in 2016. As shown in figure 16, the cross-section switches 5-periodically between bean shape and triangle shape. Due to this 5-periodicity, the magnetic field topology forms magnetic islands at resonant rotational transform values $\left(\frac{n}{5}\right)$. Because there are divertors located inside these magnetic islands, the plasma heating is suppressed by intersecting the flux surfaces. Thereby, the magnetic island region becomes a scrape-off layer.

In the limiter campaign, as well as in the first two divertor campaigns, hydrogen and helium plasmas were used. The technical specifications of W7-X are given in table 3. The plasma on W7-X is heated by electron cyclotron resonance heating (ECRH). Therefore, 10 gyrotrons with 140 GHz and up to 10 MW microwave power are available. For standard scenario at $2,5$ T this leads to X2 on-axis heating. [59] For a lower magnetic field, off-axis and higher harmonic heating are also available. This heating guarantees, that the heat source inside the SOL is only given by transport from core plasma through the LCFS.

A benefit for further studies of the particle and heat transport in the SOL region is that in W7-X, the torioidal and poloidal magnetic field can be completely generated by external coils. Therefore, the rotational transform in the scrape-off layer can be adapted and thereby the magnetic field topology, especially the edge island size, can be varied.

3.2 Edge diagnostics

At W7-X, different diagnostics are available to obtain ion and electron parameters to investigate the particle and heat flux distribution in the plasma edge. The used diagnostics and its applications are listed below.

Used additional diagnostics		
Divertor Langmuir probe:	T_e,n_e	@divertor
Spectroscopy:	particle flux	@divertor
Infrared camera:	heat flux	@divertor
Spectroscopy:	T_e,n_e	@SOL
Ion sensitive probe:	T_i,n_i	@SOL
Retarding field analyzer:	T_i,n_i	@SOL
EMC-3-Eirene modeling:	T_e,n_e,T_i,n_i	linking SOL and divertor

The devolped multi-channel retarding field analyzer for ion parameter measurements and Langmuir probe for electron parameter measurements will be described in detail in chapter 4. The ion sensitive probe is a new probe design, described detailed in [22]. It features a structure much like the Langmuir probe, which the addition of an electron replying tube which surrounds the pin. Similar to a single Langmuir probe, I-U characteristics will be measured. All three probes were used on the the fast multipurpose manipulator at W7-X.

These methods interact directly with the plasma and therefore influence it. Other possibilities include the the non-invasive methods like spectroscopy and infrared camera.

3.2.1 Non-invasive diagnostics

Spectroscopy: In the plasma edge a small proportion of particles which are not yet fully ionised are still availible due to the lower temperature. Bounded electrons change between different electric states and emit radiation, where the wave length is defined by the energy difference between these states. For He plasma, generally the transitions $3^1D \rightarrow 2^1P\,(\lambda_1 = 667.8\text{nm})$ and $3^1S \rightarrow 2^1P\,(\lambda_2 = 728.1\text{nm})$ were used to determine n and additionally $3^3S \rightarrow 2^3P\,(\lambda_2 = 706.5\text{nm})$ to determine T.

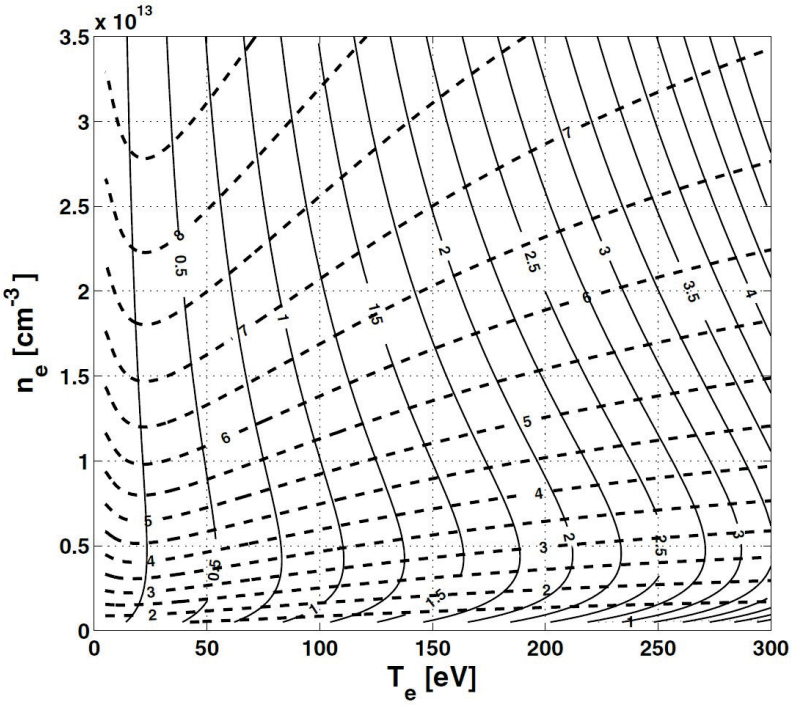

Figure 17: Temperature and density dependence of the ratios of the measured intensities of the three transitions. solid lines: $r_{12} = I_1/I_2$, dashed lines: $r_{32} = I_3/I_2$. [8]

To calculate temperature and density, the intensity of the emitted radiation of the specific wave lengths will be measured and compared with the data set of Brix [8] (see figure 17).

Infrared camera: Another method for divertor measurements is via infrared camera. It is exploited that heat flux at divertor leads to an increase of the target temperature. Due to this temperature, the target emits radiation like a black body. In the case of black body, the intensity of the signal depends on sensitivity of the camera and temperature of the emitting target. Including calibration of the camera system, it is given [16]:

$$I\left(T\right) = c_1 \cdot N_{\mathrm{IR}}\left(T\right) + c_2 \tag{3.1}$$

where N_{IR} is a simplified function of the integrated wave lenght distribution of the emitted radiation in measured range $\lambda = [\lambda_1, \lambda_2]$ and defined by [16]:

$$N_{IR} = c_3 \cdot \frac{1}{\exp\left(\frac{hc}{\lambda k_{\mathrm{B}} T}\right) - 1} + c_4 \tag{3.2}$$

The heat flux q at divertor can be calculated by determining the target temperature T_t from the measured intensity of the infrared radiation and utilising the heat conductance λ_{layer} of the d thick layer [16]:

$$q = \frac{\lambda_{\mathrm{layer}}}{d} \cdot (T_t - T_{\mathrm{bulk}}) \tag{3.3}$$

3.2.2 Invasive diagnostics

Usually there are two types of invasive diagnostics in the plasma edge. First, a manipulator can be used for different probe heads. Second, probes can be included in the divertor or limiter tiles.

The most common invasive probes are the Mach probe for plasma flow measurements, the Langmuir probe for electron temperature, potential and density measurements, and the retarding field analyzer or ion sensitive probe for ion temperature measurements.

All three probes use I-U-curve measurements in thermal plasma with biased pins. The characteristic curve of Langmuir pins is shown in figure 18. However, the ion sensitive probe and the retarding field analyzer diverge to 0 for high positive biasing, due to the electron repelling.

In the following, the characteristic points in the curve are defined:

- Plasma potential V_{p}: Potential of the plasma in front of the probe, which is given by [41]

$$V_{\mathrm{p}} = V_{\mathrm{f}} + kT_e \tag{3.4}$$

- Floating potential V_f: Potential of a surface (e.g. the probe tip) due to sheath effects, caused by interaction between plasma and surface, which is defined by [76]

$$\Psi = -\frac{T_e}{2e} \ln \left[2\pi \frac{5}{2} \left(\frac{m_e}{m_i} \right) \left(1 + \frac{T_i}{T_e} \right) \right] \tag{3.5}$$

- Ion saturation current I_sat: Pure ion current is measured due to a total reflection of the electrons by the biased probe.

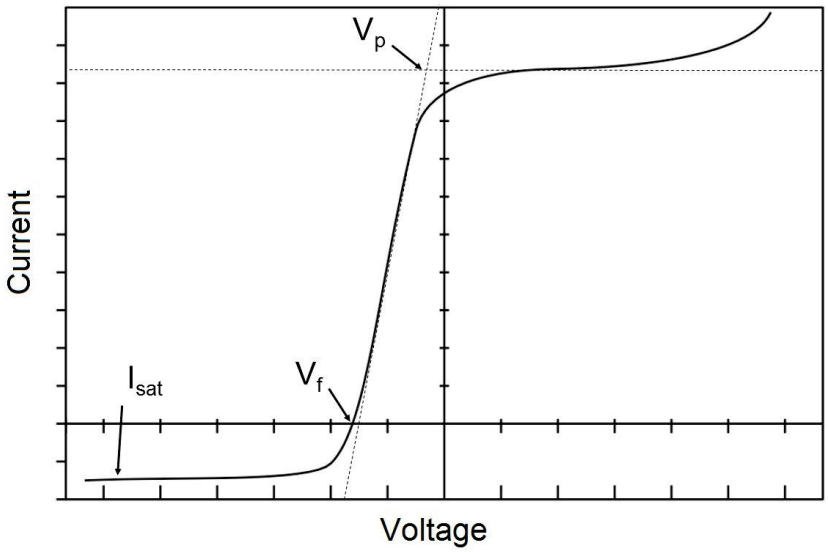

Figure 18: I-U-curve of current measurements in thermal plasma with biased pins.

Mach probe: The Mach probe is used to determine the plasma flow parallel to the magnetic field lines. For characterising such flow, the so-called Mach number M was introduced. The Mach number is the ratio between the plasma flow velocity and the ion sound speed $c_\mathrm{s} = \sqrt{k_\mathrm{B} \left(T_e + T_i \right) / m_i}$ [49]:

$$M = \frac{v}{c_\mathrm{s}} \tag{3.6}$$

To determine this value, a double pin probe is used. A sketch is shown in figure 19. The biased pins are oriented along the magnetic field line and are separated by a plasma

blocking component. Thereby, the ion saturation currents in the direction of both upstream (core) and downstream (divertor) will be measured.

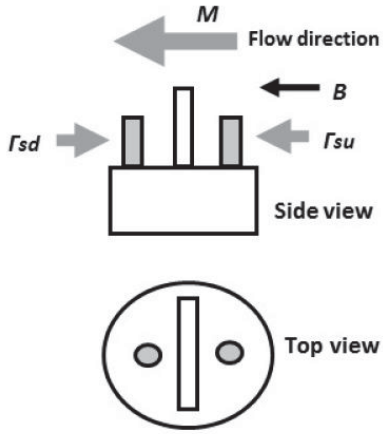

Figure 19: Schematic view of a Mach probe [41].

Using a 1-dimentional fluid model, the Mach number can be determined by the ratio of up- I_{up} and downstream ion saturation current I_{down} [1]:

$$M = M_{\mathrm{C}} \ln\left(\frac{I_{\mathrm{up}}}{I_{\mathrm{down}}}\right) \tag{3.7}$$

Langmuir probe: The Langmuir probe is used for electron temperature measurements. An often used design is the triple Langmuir probe, including one floated pin for floating potential measurements, one positively biased V_+, and one negatively biased pin V_-. A schematic view of a triple probe is shown in figure 20.

Using the characteristic points in an I-U curve, temperature and density can be determined. The electron temperature can be measured by using the floating potential and V_+ [41]:

$$T_e = (V_+ - V_f) \ln 2 \tag{3.8}$$

The density can be determined by using the ion saturation current measured with the V_- and V_+ pins with surface areas A_{p} [41]:

$$I_{\mathrm{sat}} = e n_e A_{\mathrm{p}} c_{\mathrm{s}} \tag{3.9}$$

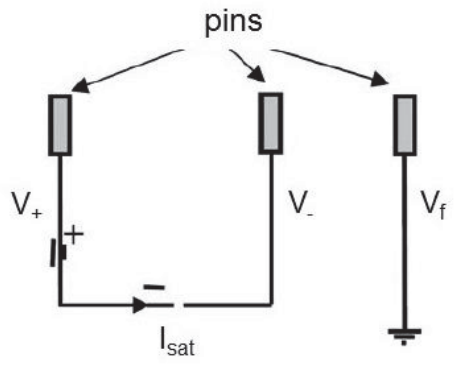

Figure 20: Schematic view of a triple Langmuir probe. [41]

Ion sensitive probe: The ion temperature can not be measured by a Langmuir probe, because of the higher mass of ions compared to electrons. Therefore, the ion sensitive probe was developed.

This probe includes an inner pin, surrounded by an outer ring. The inner pin is located inside the probe head in such a way that the distance to the top surface is larger than the electron Larmor radius and smaller than the ion Larmor radius, to ensure pure ion measurements. This pin will be biased sweeping U_G, similar to a retarding field anaylzer (see chapter 4) or a single Langmuir probe. In addition, the outer ring is biased negatively U_0 to protect the pin from electrons. A schematic view of an ion sensitive probe is shown in figure 21.

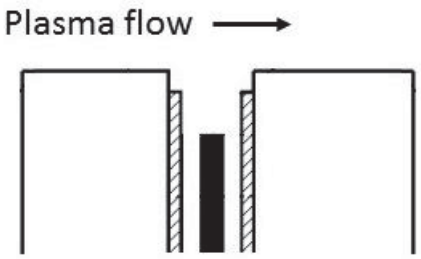

Figure 21: Schematic view of an ion sensitive probe with inner pin (black) and outer ring (shadded).

By sweeping the biasing on the inner pin, all of the I-U characteristics can be measured. For a Maxwellian distribution of the single ion velocities in the plasmas, the current measured by the inner pin can be expressed by [44]:

$$I \sim eZ_i \cdot \int_{v_0}^{\infty} dv_\parallel v_\parallel f\left(v_\parallel\right) \xi\left(v_\parallel\right) \tag{3.10}$$

$$I = I_0 \exp\left(-\frac{Z_i}{T_i}\left(U_\mathrm{G} - U_0\right)\right) + I_\mathrm{offset} \tag{3.11}$$

$$I_0 = \frac{1}{4} q n A_\mathrm{p} \sqrt{\frac{8 k_\mathrm{B} T_i}{\pi m_i}} \tag{3.12}$$

Using this equation, the ion temperature can be determined by fitting an exponential decay on the measured I-U characteristic.

3.3 Fast particle diagnostics

In addition to the edge diagnostic, two core diagnostics were used for the fast particle experiments on the tokmak EAST. The principles of these are shown in the following.

Solid state neutral particle analyzer: For the neutral particle analyzer will be used, that ions in the plasma core collides with neutral particles. During this process, they exchange charge ($\mathrm{i}^+_\mathrm{fast} + \mathrm{i}^0 \rightarrow \mathrm{i}^0_\mathrm{fast} + \mathrm{i}^+$). Afterwards, the resulting fast neutral particle moves outwards with the previous energy and momentum because only a small amount of energy is transferred.

To measure the resulting fast neutral particle, a solid state probe will usually be used, to reionise the fast particles. Using a magnetic field, a velocity separation for different detector channels can be achieved, using the dependence of the Lorentz force on the velocity.

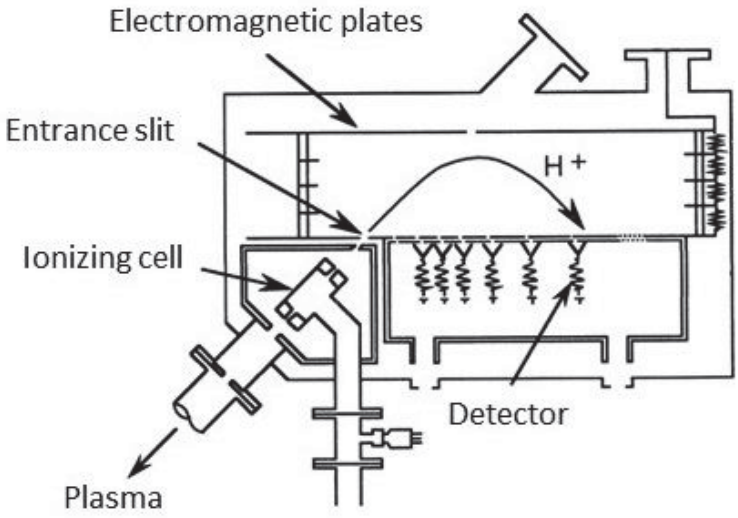

Figure 22: Sketch of a neutral particle anayzer, including ionising cell, entrance slit, electromagnetic plates and detectors.

Heterodyne radiometer: The gyrating electrons in the plasma core emit radiation. The frequency depends on the magnetic field and can be calculated for the harmonic n in tokamaks with [65]:

$$f_n = \frac{neT_{T0}R_0}{2\pi m_e \gamma \left(R_0 + r\right)} \tag{3.13}$$

Scanning the frequency of the heterodyne radiometer and given magnetic field, the radial position in the plasma core can be be scanned. Further, the transport of the signal in a thermal plasma is given by [65]:

$$I\left(\omega\right) = I_B\left(\omega\right)\left(1 - \exp\left(-r\left(\omega\right)\right)\right) \tag{3.14}$$

For an optical thick plasma, the detected signal is given by [65]:

$$I\left(\omega\right) = \frac{\omega^2 k_B T_e}{8\pi^3 c^2} \tag{3.15}$$

and is linear proportional to the electron temperature. For fast particles $E >> k_B T_e$, a superposed signal to the thermal particle related signal in the heterodyne radiometer can be found.

4 Multi-channel retarding field analyzer probe

As shown in the previous chapters, the ion temperature distributionmust be known, to investigate the particle and heat transport in the SOL region. Therefore, a multi-channel retarding field analyzer was developed.

In the first part, the basic design will be described. Further, feasibility tests will be preseneted that were performed on the linear plasma device PSI-2. Additionally, the influence of the design parameters on the measurements was simulated and will be shown.

The design of the developed multi-channel RFA probe, and first measurements of ion temperature profiles and fast particle propagation on the EAST tokamak will be described in the second part.

Further, the improved design of the multi-channel RFA probe and ion temperature measurements during the second divertor campaign on Wendelstein 7-X stellarator will be shown in the last part.

4.1 Design of the multi-channel retarding field analyzer

4.1.1 Multi-channel retarding field analyzer probe head

The design of a single-channel retarding field analyzer was established in the eighties (e.g. [53], [50]). For investigations of radial transport in the SOL region, a multi-channel retarding field analyzer was developed. A schematic design is shown in figure 23.

The front slit plate is made by tungsten, due to the good thermal resistance. Because the power distribution can be distorted by increasing thickness of the slit plates [42], the first plate has a thickness of 3 mm and triangle slits, so that at smallest slit width it has an effective depth of 100 µm (see figure 24).

Further, the slit width should be of the order of the Debye length (between 10 µm and 100 µm on EAST and W7-X) to shield the measurements from collective plasma effects [20]. For the upper limit (100 µm), experiments on the PSI-2 device showed good shielding (see chapter 4.1.2). Therefore, a slit width of 100 µm was used on the front slit plate for both EAST campaigns and for W7-X during the first divertor campaign.

Because of the space charge limit [53], care must be taken care to limit the plasma current density inside the probe head. For the multi-channel RFA probe used on EAST during the 2016 and 2017 camapigns and on W7-X during the first divertor campaign, the plasma was limited by an additional low transmission grid, also made of tungsten, and with a thickness of 50 µm due to the lower heat load. Due to the reduced slit width of 30 µm for the multi-channel RFA probe on W7-X during the second divertor campaign campaign, the low transmission grid was omitted.

The first high transmission grid is biased negatively to repel the thermal electrons from the plasma. The transmitted ions are then decelerated by the second high transmission grid, biased sweeping positively. Additionally, there is a third negatively biased high transmission grid, to repel secondary electrons from the collector. For these high transmission grids, tungsten plates with a thickness of 50 µm are used as well. The grid bars have a width of 100 µm and are separated by 400 µm space, which leads to a transmission factor of 80%.

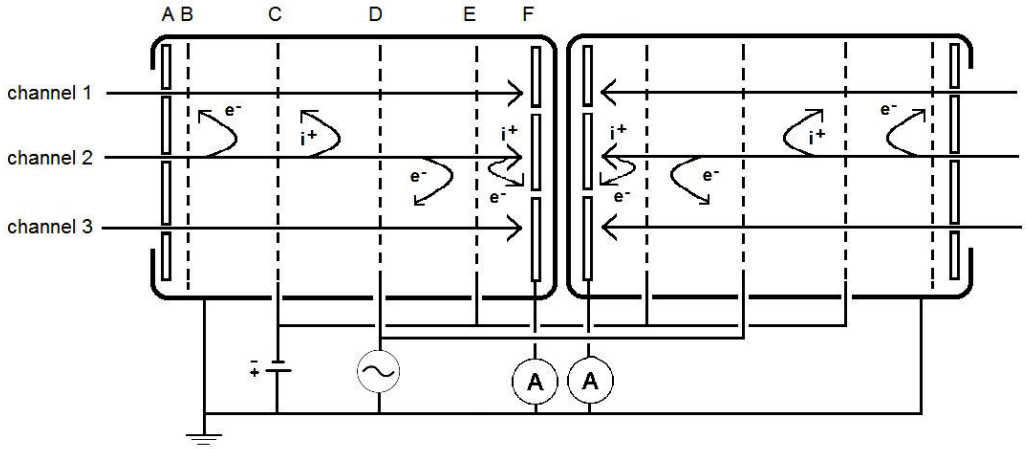

Figure 23: Schematic view of the structure of the MC-RFA probe modules. Front slit plate (A), low transmission grid (B), high transmission grids (C-E), collector strips (F) [31].

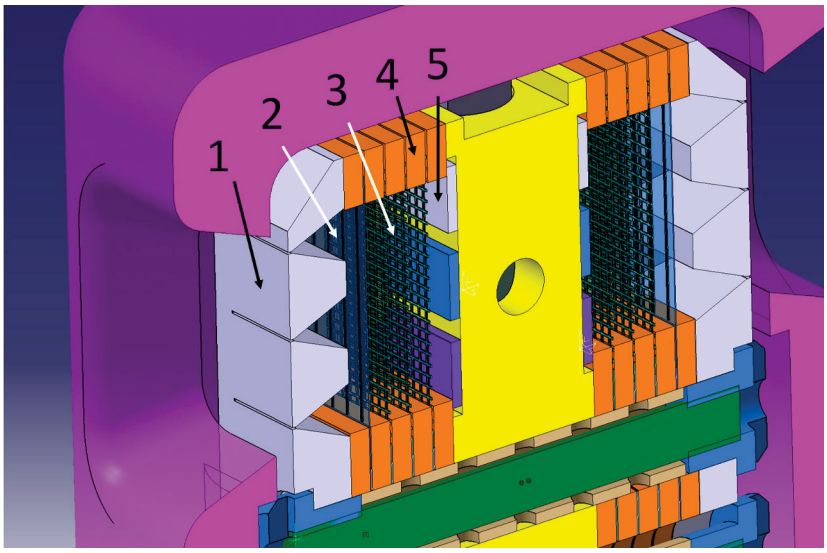

Figure 24: Design of MC-RFA modules: slit component for different channels (1), low transmission grid (2), high transmission grids (3), ceramic components (4), collector plates (5) [31].

The overcomming ions generate a detector current, which can be measured and is defined by the second grid voltage U_G. The measured detector current can be expressed as [44]

$$I \sim eZ_i \cdot \int_{v_0}^{\infty} dv_\parallel v_\parallel f\left(v_\parallel\right) \xi\left(v_\parallel\right) \tag{4.1}$$

where $v_0 = \sqrt{eZ_i \left(U_\mathrm{G} - U_0\right)/m_i}$, $f\left(v_\parallel\right)$ is the parallel velocity distribution, $\xi\left(v_\parallel\right)$ is the parallel transmission factor, U_0 is the first grid voltage and eZ_i is the ion charge.

Outside the RFA probe, the thermal ion velocity distribution is assumed as maxwellian. So the collector current can be approximated as [20]

$$I = I_0 \exp\left(-\frac{Z_i}{T_i^*}\left(U_\mathrm{G} - U_0\right)\right) + I_\mathrm{offset} \tag{4.2}$$

where I_offset is given by any offset of the electronics and I_0 defined by the ion saturation current:

$$I_0 = \frac{1}{4} qnA\tau \sqrt{\frac{8k_\mathrm{B}T}{\pi m}} \tag{4.3}$$

where A is the effective entrance area given by the front slit plate and the low transmission grid, and τ the transmission factor given by the high transmission grids. Fitting this equation to a measured I-U characteristic, the ion temperature can be calculated.

To disturb the electric field between the grids as little as possible, they are planar and separated by 1 mm thick ceramic components (ZrO_2 on PSI-2 and Al_2O_3 on EAST and W7-X).

The collectors are also made of tungsten. They are divided into three strips each side (see figure 24), to measure the collected ion current of the three channels each side independently. On the basis of the expected ion temperatures and densities from previous experiments [17] and the used low and high transmission grids, collector currents in the order of several hundred µA were expected.

Within the probe head, two MC-RFA modules are embedded back to back for simultaneous measurements parallel and anti-parallel to the magnetic field lines, as shown in figure 25. In order to compare the ion temperature to the electron temperature,

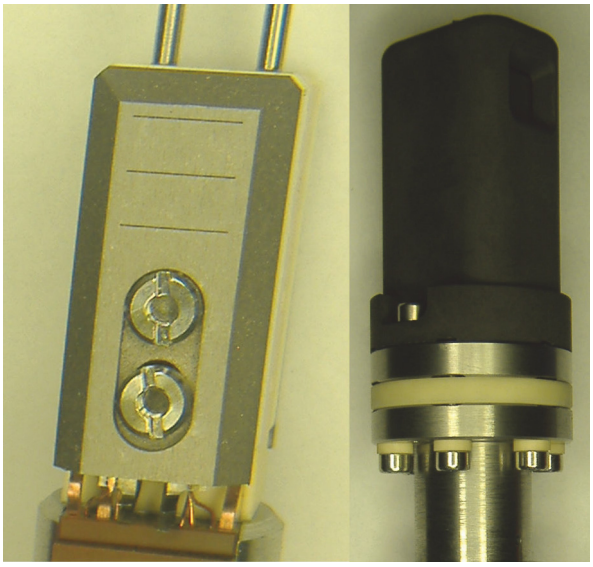

Figure 25: Developed multi-channel RFA probe for EAST (right), premounted back-to-back oriented RFA modules (left) [31].

several Langmuir pins are integrated (see chapter 4.2.1 for EAST and chapter 4.2.2 for W7-X).

This probe head is protected by a graphite cover (see figure 25) on EAST during the 2016 and 2017 campaigns and W7-X during the first divertor campaign and protected by a boron nitride on W7-X during the second divertor campaign. It is mounted on a manipulator system, which can be moved maximum 2 m/s on EAST [73] and maximum 3.5 m/s on W7-X [54] and it is capable of crossing the last close flux surface (LCFS).

4.1.2 Feasibility test on the linear device PSI-2

The linear plasma device PSI-2 was used for a feasibility test of a multi-channel retarding field analyzer. This device has a magnetic field of 0.1 T and is able to produce plasmas with electron temperatures up to 30 eV and densities of the order of up to 10^{18} m^{-3}. Previous experiments showed an ion temperature of $T_i = T_e/3$. For this measurements deuterium or hydrogen plasmas were used.

In contrast to the design of the MC-RFA used on EAST tokamak and W7-X stellarator, this probe has only two channels. The front slit plate has a thickness of 50 µm, due to the lower heat load and a slit width of 100 µm, similar to the design used on EAST. For

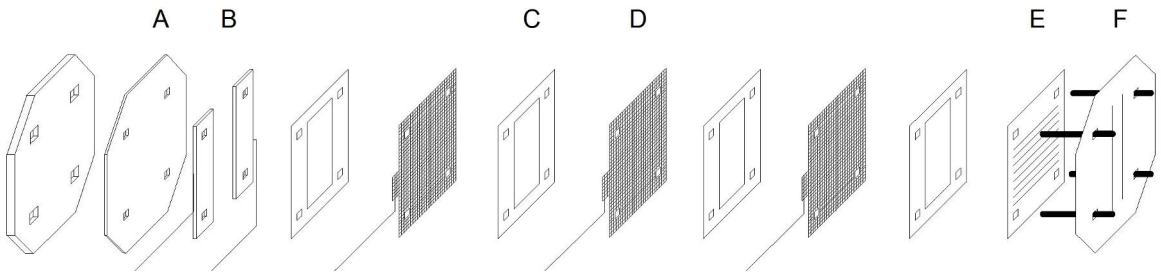

Figure 26: Sketch of simplified design: ZrO_2 plate (A), collector plates (B), 1 mm thick ZrO_2 plate, grids (D), low transmission grid (E), 2-channel slit plate (F). Components were held together with 4 ZrO_2 sticks (black).

separation, ZrO_2 plates with a thickness of 1 mm were used. In addition, two collector strips, made from stainless steel, were used.

The grids were also made of stainless steel. The sweeping voltage on the second grid was set from -50 V to 100 V, generated by a Textronix AFG 320 and amplified using a Kepco BOP 200/1. In addition, the fixed voltages on the first and third grid were set to -25 V or -50 V provided by a GW Instek GPS-4303.

The different components were held together by four sticks, made from ZrO_2 and mounted through holes in the edges of the components, as shown in figure 26. The whole stack is mounted in a tube holder, also made of stainless steel.

The measured collector currents were amplified using the amplifier card from EAST experiments. Depending on the chosen channel, an amplification of 10 µA, 100 µA or 1 mA to 5 V can be reached.

In the following, the evaluation and optimisation of the collector signal will be presented.

First, capacity effects are an important aspect of the grid system of an RFA probe, because of the AC voltage at the second grid. As shown in figure 27, the capacity currents follow the well known linear dependence on the scanning frequency of the swept biasing voltage on the second grid.

To be able the measure the temperature profiles during experiments, a sweeping frequency of the order of 1 kHz should be used. To minimise the capacity current and ensure a high signal to background ratio, two approaches were made.

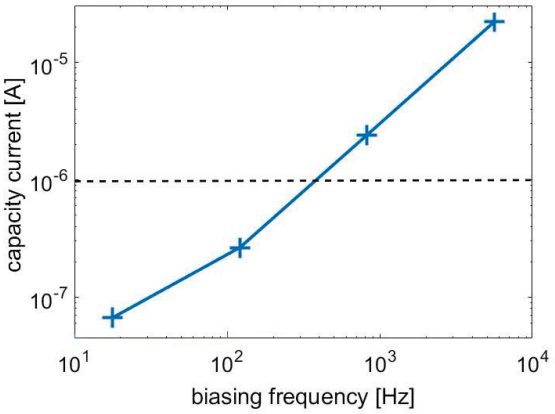

Figure 27: Frequency scan of the capacity current (blue) and the order of expected particle current (dashed).

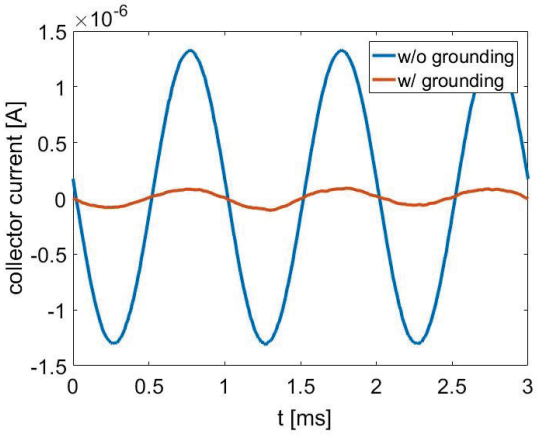

Figure 28: Collector current without plasma for 1 kHz sweeping frequency with (red) and without (blue) grounding.

In the design used on EAST, a conductive probe cover made of graphite is used. This leads to an amplification of the capacity effects like in a transformer. Grounding this cover fixes the potential of the cover and reduces the measured capacity current by a factor of 16, as shown in figure 28. However, meaurements in W7-X during the first divertor camapign showed that grounding the cover perturbes the plasma much more strongly and should be avoid if the signal to noice ratio is large enough. During experiments in the second divertor camapaign of W7-X, a non-conductive cover made of Boron nitride is used.

Additionally, the selected material for the ceramic components are important. ZrO_2 has a permittivity of 28. Therefore Al_2O_3 with a lower permittivity of 9.9 is used for EAST and W7-X.

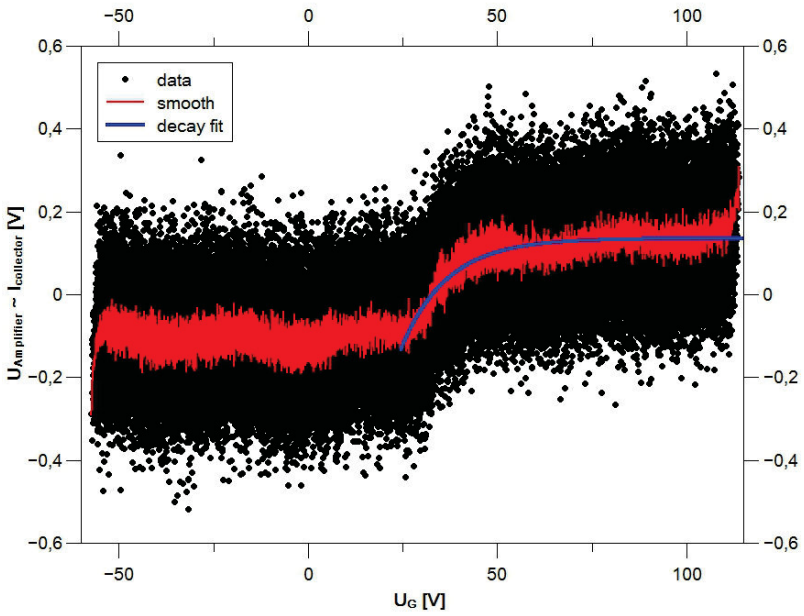

Figure 29: Measured I-U characteristic: raw data (black), low pass filtered data (red), and decay fit for ion temperature calculation (blue).

Since the measurements have been optimised, the multi-channel feasibility was checked, using two channels with a radial distance of 2 mm. Therefore saturation current profiles and ion temperature profiles were measured on the linear device PSI-2 with a lower scanning frequency of 5 Hz and a maximum manipulator velocity of 5 mm/s.

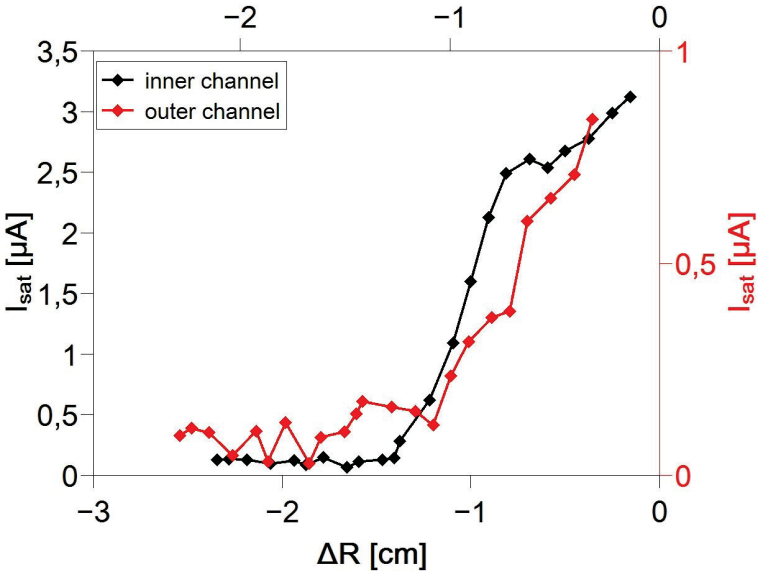

Figure 30: Ion saturation current of both channels for 5 Hz sweeping of U_G.

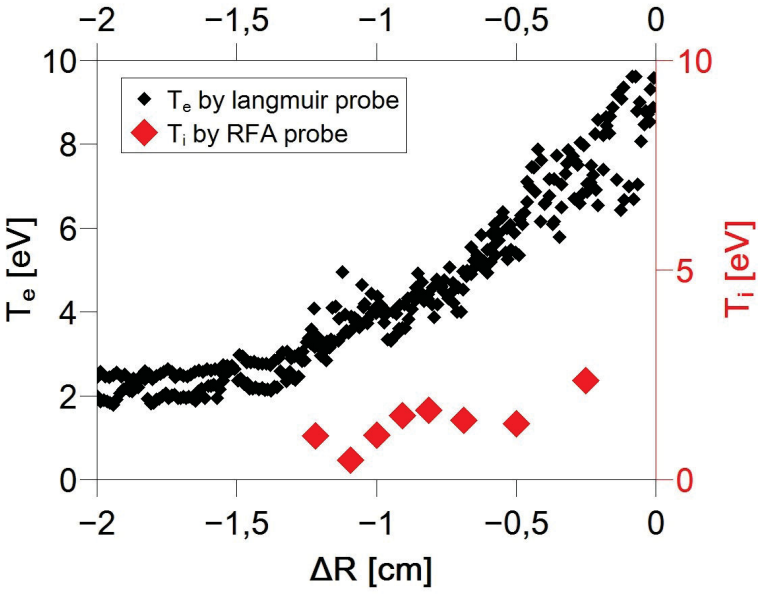

Figure 31: Calculated ion temperature profile on PSI-2 using the RFA probe (red) and electron temperature profile using a Langmuir probe (black).

The radial ion temperature profile measurements were measured with both channels simultaneously. Although the signal to noise ratio is low, due to the low plasma density, both ion saturation profiles follow the same radial gradient, as shown in figure 30. With higher ion density and temperature on W7-X and EAST of the order of 10 to 50 times higher values, the signal to noise ratio is larger and therefore the error becomes smaller.

In a second step, the ion temperature profiles were calculated, using the measured I-U characteristics, as shown in figure 29. Therefore, the data is split into a saturated part ($U < U_{\mathrm{G}}$) and a decaying part ($U > U_{\mathrm{G}}$) . Using the decaying part of the I-U characteristic, the ion temperature can be calculated.

The calculated ion temperature profile, shown in figure 31, is approximately a third of the electron temperature profile measured by a Langmuir probe. These values are comparable to previous experiments on PSI-2.

Summarising the experiments on PSI-2, the signal to background ratio could be increased, the multi-channel feasibility is shown and the ion temperature measurements were proven. Therefore, the multi-channel RFA design will be used for further investigations on ions in the SOL region of the tokamak EAST and the stellarator W7-X.

4.1.3 Influence of the RFA design on the measurements

The basic design of a retarding field analyzer has been established since the eighties (e.g. [50]). However, it was shown in previous publications [42] that the design parameters, like the slit width, has an impact on the measured energy distribution and therefore the accuracy of ion temperature calculations. Therefore, this impact will be simulated using a simple particle tracing code.

Because the MC-RFA channel size is significantly smaller than the fusion device, a simplified and non-curved magnetic field is used. As shown in figure 32, the boundary conditions are defined by the cover, the slit width of the front slit plate and the angle of the triangle slits of the first slit plate. The influence of the grids are neglected due to the larger structure size compared to the slit width.

First, the single ion particle energy and the ratio of perpendicular to total velocity compared to the magnetic field lines is chosen. In a second step, equally distributed starting positions of the gyration center for the particle tracing were allocated. Additionally, for every starting point, equally distributed gyration phases were set. In a

third step, the particle tracing is conducted, until the particle hits a wall or boundary limit. Due to the floated slit plate being prefered during EAST and W7-X experiments, electric fields within the boudary limit were neglected.

Counting the transmitted particles, a so-called sensitivity factor for the MC-RFA probe can be calculated.

The simulated sensitivity factor of thermal hydrogen ions for the design parameters used on EAST is shown in figure 33. The energy depence is neglectible for thermal ions. In contrast, the sensitivity factor for higher perpendicular to parallel velocity ratio is strongly decreasing. As result, the measured particles are dominated by particles with low perpendicular velocity contribution.

Due to the gyration motion of magnetically confined ions, the slit width is also important. If the Larmor radii are large enough, the particles hit the inner slit wall and do not transmit. As shown in figure 34, the sensitivity factor for gyrating ions strongly decreases for small slit width. Therefore, the slit width should be as large as possible. However, the slit width is limited by space charge limit and debye length of the plasma.

As published by M. Kočan [44], the slit plate thickness also has an impact on the sensitivity factor. To reduce these effects, a triangle slit was used, to reduce the effective depth. However, the suppression effect and heat deposition from plasma on the sharp slits edges has to be compared. As a result, an angle of 30° was chosen for experiments on EAST and W7-X.

Even for optimised design parameters, the probe head cannot be adjusted absolutly to be parallel to the magnetic field lines, because the magnetic topology at the probe head changes during the radial movement. Therefore, the effect of the adjustment angle between probe head and magnetic field line on the transmission of ions was calculated. As shown in figure 35, the sensitivity factor, especially for small gyration radii, decreases strongly for small slit width. On the other side, for a larger slit with (like used on EAST tokamak), such a strong suppression cannot be seen.

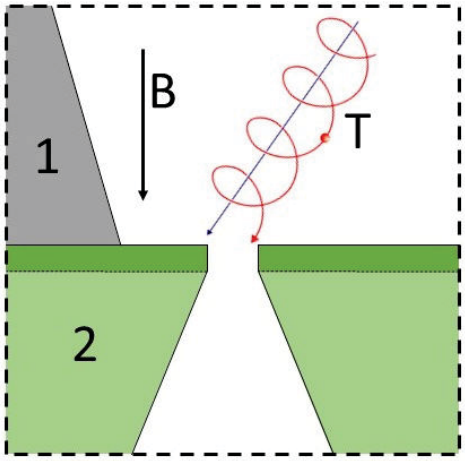

Figure 32: Sketch of the boundary conditions for the particle tracing. 1: probe cover, 2: slit plate, defined by slit width and triangle slit, B: direction of magnetic field line, T: particle trajectory, defined by tilt angle of the gyration center and gyration.

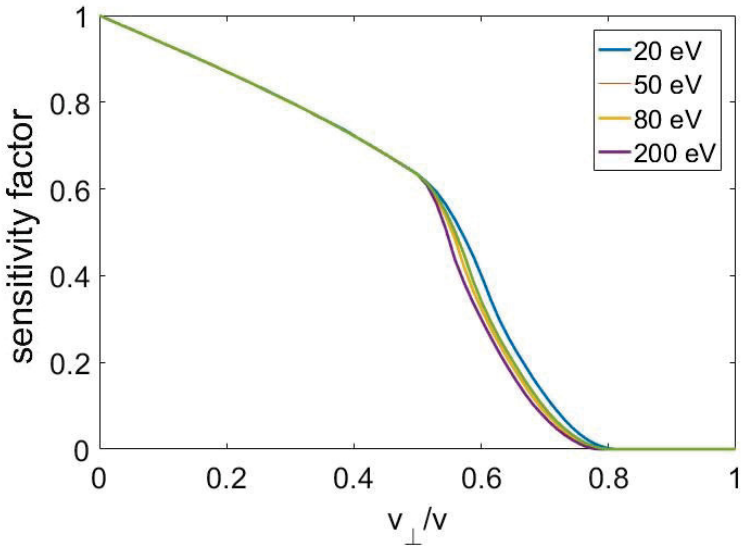

Figure 33: Normalised sensitivity factor for different single particle energies in the thermal range in dependence on the ratio between gyration velocity and total velocity of the particle.

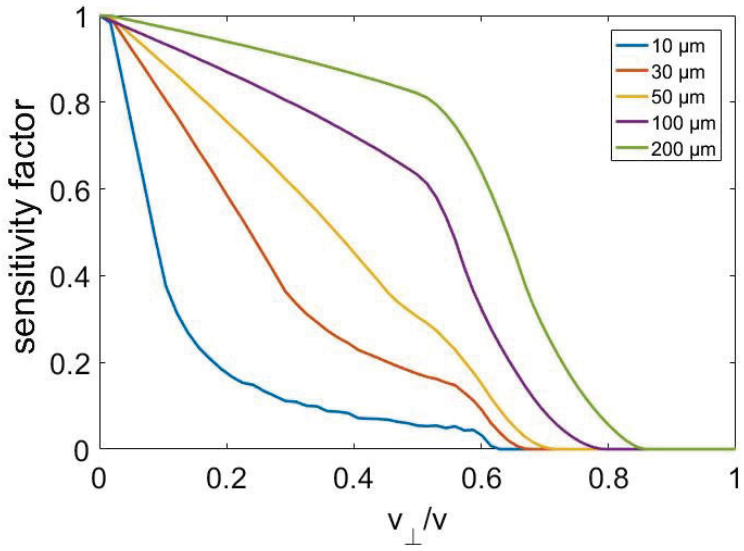

Figure 34: Normalised sensitivity factor for different slit widths in dependence on the ratio between gyration velocity and total velocity of the particle.

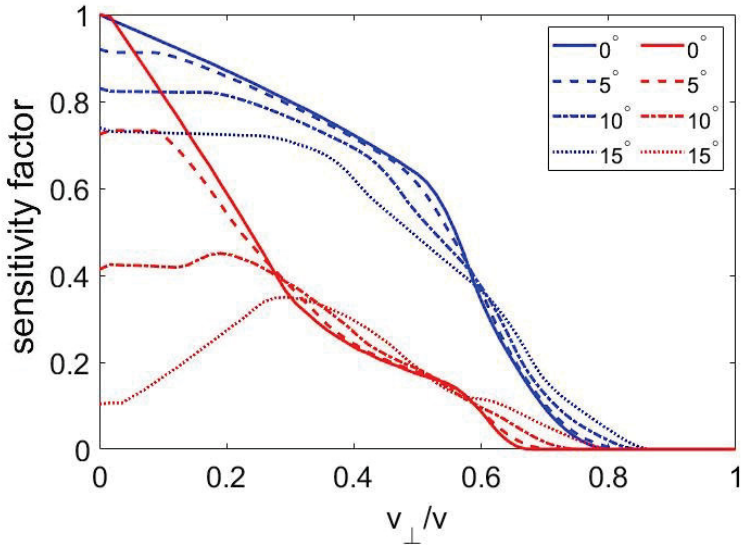

Figure 35: Normalised sensitivity factor for different tilt angle between magnetic field line and probe head in dependence on the ratio between gyration velocity and total velocity of the particle. blue: 100 µm slit width (used on EAST tokamak), red: 30 µm slit width (used on W7-X stellarator).

4.2 Commissioning of the mutli-channel retarding field analyzer

Parts of the following chapter are published in:

M. Henkel et al: *Development of a multi-channel retarding field analyzer for the SOL physics on EAST and W7-X*, europhysics conference abstracts Volume 41F (2017)

M. Henkel et al: *Multi-channel retarding field analyzer for EAST*, Plasma science and technology 20 (2018)

M. Henkel et al: *Retarding field analyzer for the Wendelstein 7-X boundary plasma*, Fusion Engineering and Design, Volume 157, 111623 (2020)

4.2.1 Multi-channel retarding field analyzer for the EAST tokamak

A multi-channel RFA probe with 3 channels each parallel and anti-parallel to the magnetic field lines and a set of single-Langmuir pin and floating potential pin was developed for the 2016 and 2017 campaigns on EAST tokamak (see figure 36). Its aim was to show the feasibillity on midle-sized fusion devices in preparation for the W7-X experiments (see chapter 6). Further, fast particle measurements in the plasma edge of EAST tokamak during ELM appaerance were done, as shown in chapter 5.

The basic design of our MC-RFA probe is shown in chapter 4.1.1. As already mentioned, it is important that the slit width is of the order of the Debye length (at EAST $10 - 100$ textmu m) in order to shield the measurements from collective plasma effects [7]. Even experiments in the SOL region of the EAST tokamak showed good shielding by suppressed floating potential at the low transmission grid. Thus, the front slit plate width of 100 µm seems appropriate.

Due to the high power load on the front slit plate, a thickness of 3 mm were used. To reduce the (see chapter 4.1.3) triangular slits were used, so that at smallest slit width of 100 µm an effective depth of 100 µm is given. Further, a distance of 4 mm for the front slit plate and 1 mm for the low transmission slit plate are chosen to ensure that the plasma density inside the probe head is below the space charge limit.

Grids 1 and 3 are biased negatively with $U_0 = -200$ V using a Gensys 100/15 DC power supply. The biased voltage on grid 2 can be swept up to a maximum of ± 200 V and sweeping frequency of up to 1 kHz. This sweeping rate of less than 200 kV/s ensures

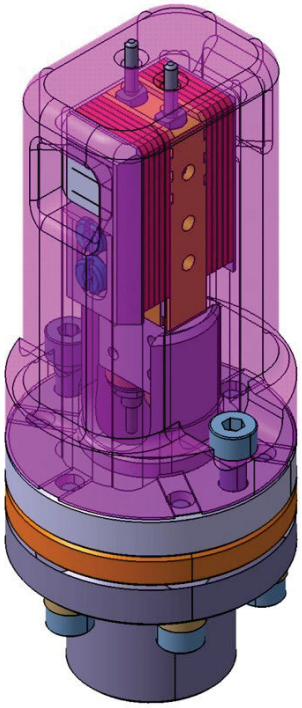

Figure 36: Sketch MC-RFA-probe for the 2016 and 2017 campaign on EAST tokamak, supplemented by two Langmuir pins.

that the signal follows the sweep and the capacitive effects are reasonably low. The constant biasing for grid 1 and 3 was generated using a Wavetec 275 with a maximum range of 10 V and amplified by a Kepco BOP 200/1 to obtain sweeping of up to ±200 V. The collector currents were measured over a variable resistance. Including the data aquisition, an amplification of 10 µA up to 1 mA to 3.76 V on EAST is reached.

To obtain futher information about the electron temeprature and floating potential, two pins were mounted on top of the probe (see chapter 4.1.1). One pin is used as single-pin Langmuir probe to measure electron temperature profiles. The second pin is grounded via a 1 M Ω resistance for floating potential measurements.

This probe head is protected by a graphite cover and mounted on a midplane manipulator system in the low-field side, which can be moved at a maximum speed of 2 m/s and which is capable of crossing the LCFS. The tilt angle of the probe head can be adjusted with a screw system between probe head and manipulator in order to match the tilt angle of the magnetic field lines.

For the commissioning of the MC-RFA probe on EAST, deuterium plasmas were used. Plasma currents I_P of 400 or 450 kA and a vacuum toroidal magnetic field of 1.78 or 2.19 T with upper single-null configuration were chosen. The discharges were heated ohmically and by lower hybrid wave heating. For H-mode plasmas, NBI heating was added.

The radial ion temperature profiles were measured with both opposite MC-RFA modules, including up to three channels each side. Because the ion temperature and electron temperature profiles are measured at the same axis along the manipulator movement, the relative positions to each other are independent on magnetic topology.

The electron temperature was calculated from the I–U curve, measured with the single-Langmuir pin on top of the MC-RFA probe. One exemplary electron temperature profile is shown in figure 37. Additionally, floating potential measurements were done, as shown in figure 38. Also, multi-channel ion temperature measurements were performed, shown in figure 39.

Because the maxwellian distributionis changed by the presheath, the values parallel (p) and anti-parallel (a) to the magnetic field lines are not equal and $T_i = (T_{p,i} + T_{a,i})/2$ [6] should be used. In this case, the nonaveraged T_i is shown because the lower hybrid heating may cause superposed signals from fast particles.

The calculated ion temperature decay length, shown in figure 39, is 6.5 mm ± 1.0 mm. The plotted channels showed comparable ion temperature profiles within the error bars of less than 10%, so that the usability for simultaneous measurements at different radial positions is proven. Unfortunately, due to lithium coating in the vessel, some of the channels were blocked and had no signal.

Previous measurements of the Mach number in the SOL region have shown values between 0.3 and 0.7, the two directions of the MC-RFA channels measure different plasma flows. In these experiments, downstream signals were too small for measurements, most likely due to the small signal to noise ratio.

Furthermore, an asymmetry of the I–U curve for the ramp up and the ramp down phases can be seen. This could be caused by a too fast sweeping rate dU_G/dt, which could influence the particles. To prevent such asymmetries, the sweeping ramp should be decreased e.g. by optimising the sweeping range.

Moreover, the small signal of the order of several µA and therefore, a small signal to noise ratio leads to an increase of the error bars. As well, additional potential at the

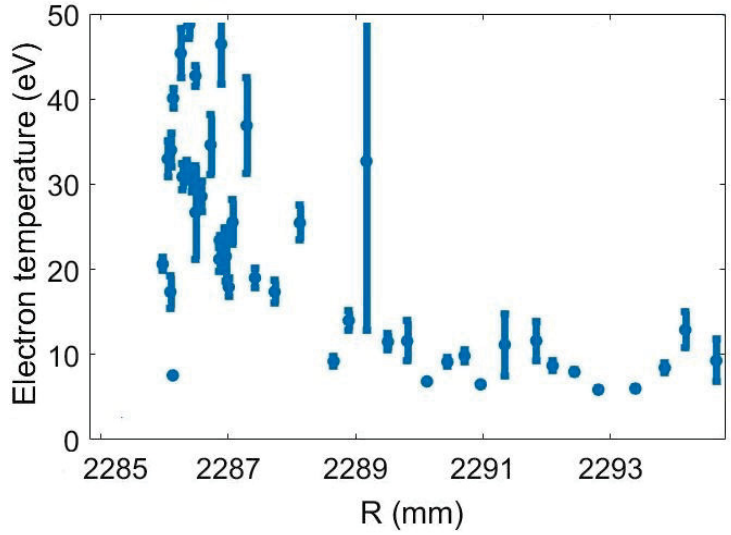

Figure 37: Exemplary electron temperature profile in the SOL region of EAST tokamak measured with the MC-RFA probe. (#72493 @ 4.8-6.0 s)

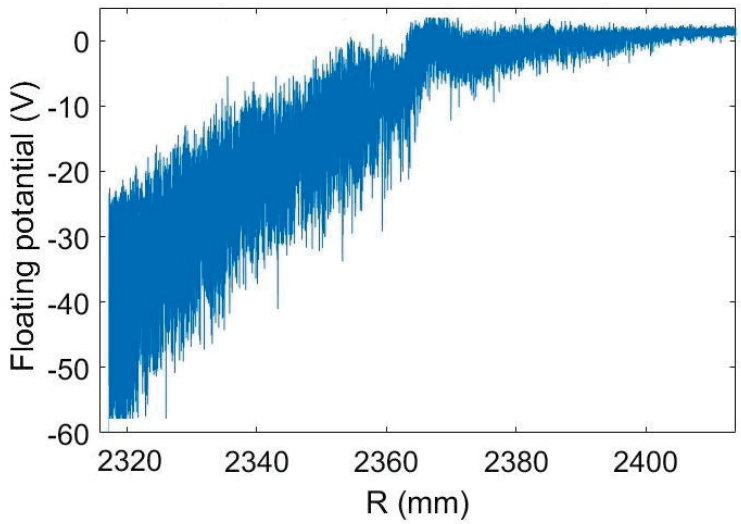

Figure 38: Exemplary floating potential profile in the SOL region of EAST tokamak measured with the MC-RFA probe. (#73107 @ 5.0-6.1 s)

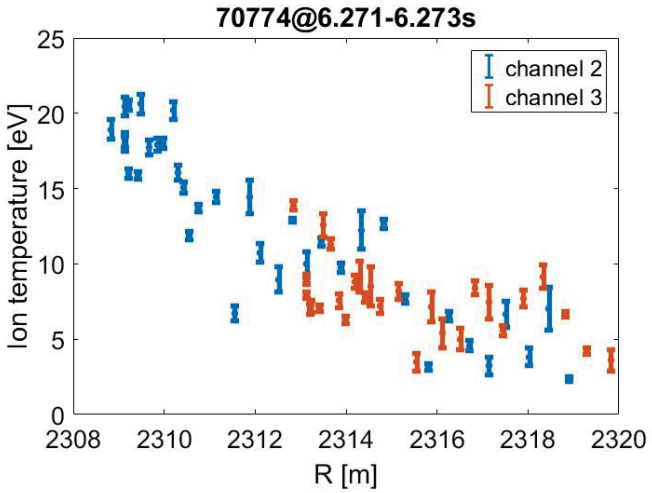

Figure 39: Exemplary ion temperature profile for two channels in the SOL region of EAST tokamak measured with the MC-RFA probe. (#70774 @ 6.2-6.3 s)

probe head, e.g. the floating potential of the cover, can lead to a shift of the I–U curve. To decrease the error bars of the ion temperature measurements, the low transmission grid will be removed for future experiments.

4.2.2 Multi-channel retarding field analyzer for the Wendelstein 7-X stellarator

For more flexibility during experiments, the pin system on top of the MC-RFA probe was enlarged for the second divertor campaign of W7-X stellarator. Unlike the EAST design, in W7-X five tungsten pins were used (see figure 40). All pins had a diameter of 2 mm and protruded from the cover by 3 mm. This enables triple Langmuir probe measurements with a higher time resolution of 1 MHz, instead of 1 kHz for single Langmuir probe measurements. Additionally, an optional gas inlet, made from stainless steel, was installed. To prevent conductive contact between the extended set of pins and the cover, the cover for the second divertor campaign was made of boron nitride, which is not conductive.

Furthermore, the slit width for the RFA modules was reduced to 30 µm because the debye lengths was expected in the order of 5 to 50 µm in the SOL region, based on previous experiments on the W7-X stellarator. To still have a suitable signal to noise ratio, the low transmission slit was removed.

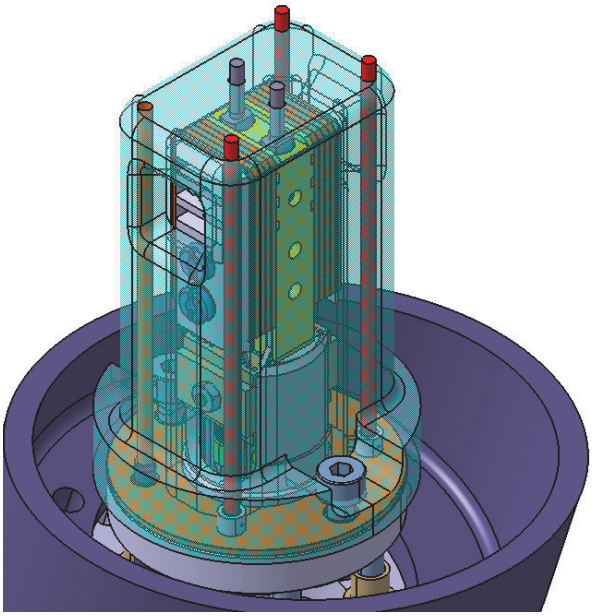

Figure 40: Sketch MC-RFA-probe for the second divertor campaign on W7-X stellarator, supplemented by five Langmuir pins and a gas inlet.

The first and third grid in the RFA modules were biased −100 V, whereas the middle grid was biased swept ±200 V. The collector currents were measured over a variable, remote controllable resistance. Including the data aquisition, an amplification of 1 mA up to 10 A to 0.5 V is reached.

Contrary to the experience at the EAST, the RFA grids were destroyed during the first divertor campaign, while using the EAST designed probe, as shown in [32]. The damage pattern points to arcing between the grids as most likely mechanism. To avoid such damage in the second divertor campaign, a 1 kΩ high power resistor was added to the biasing electronics, to reduce the current flowing through the grids. In addition, all the grids were without biasing during the first plunges of the RFA probe, to clean the MC-RFA probe with hot plasma.

In W7-X, a strong positive floating potential in the SOL was observed. In this regime, this potential could exceed the sweeping voltage on the middle grid. Under these conditions, the ions inside the RFA probe do not have a potential difference and then would not be modulated by the sweeping voltage, as shown in figure 41. However, as previously mentioned, the sweeping range should not be increased, to fit the potential in the whole SOL region, to protect the grids from arcing. Therefore, an additional

remote controllable DV power supply will be added in the next campaign, to be able to shift the biasing between the discharges.

As shown in figure 42 (left), the I-U curve is shifted for measurements close to the separatrix, most likely due to potential change by electron emmission from the heated probe, obseved for other probes in the SOL region during the second divertor camapign and indicated by a drop in the floating potential measurement. Because of that, the ion saturation can not be reached using ±200 V biasing. That is why the calculation of ion and electron temperarture profiles were limited to $R > 6.048$ m.

On the other side, a second saturation of the current can be seen in figure 42 (right). The most likely reason is a drop in the negative biasing in the RFA module. Unfortunately, the actual biasing in the RFA module was not measured, rather the voltage at the MPM connection was.

All in all, during operation of the RFA in the second divertor campaign, three collector channels (11, 12 and 23) measure modulated ion currents as the voltage applied to the second grid within the previously shown limits.

In the reference discharge, the main plasma is confined by the standard configuration and heated by 3.1 MW electron cyclotron resonance heating (ECRH) power. A central line integrated electron density $9 \cdot 10^{19}$ m^{-3} was controlled by gas puffing. Meanwhile, the MC-RFA probe was plunged into the SOL region, crossing the short and long connection length part of the magnetic edge island.

As shown in [32], the dominant frequency of the background noise is about 80 kHz. However, after plunging close to the separatrix, the frequency increased to 200 kHz. Further, in the inner channels (11 and 12) the background noise became larger for $f > 10$ kHz. This behaviour indicates, that it is possibly caused by the probe body itself modifying turbulence around it.

To reduce the noise for ion temperature calculations, the collector currents were first low-pass filtered with a cutoff frequency of 10 kHz for channels 11 and 12, and 30 kHz for channel 23 due to lower noice. They were then subtracted by the induced current, due to the inductive coupling between the middle grid and the collector (see chapter 4.1.2).

The ion temperature is obtained by fitting the I-U curve based on the equations shown in chapter 4.1.1 and assuming Z= 1 (hydrogen plasma). Because the initial input setting could affect the fitting result, the initial parameters have been scanned [32].

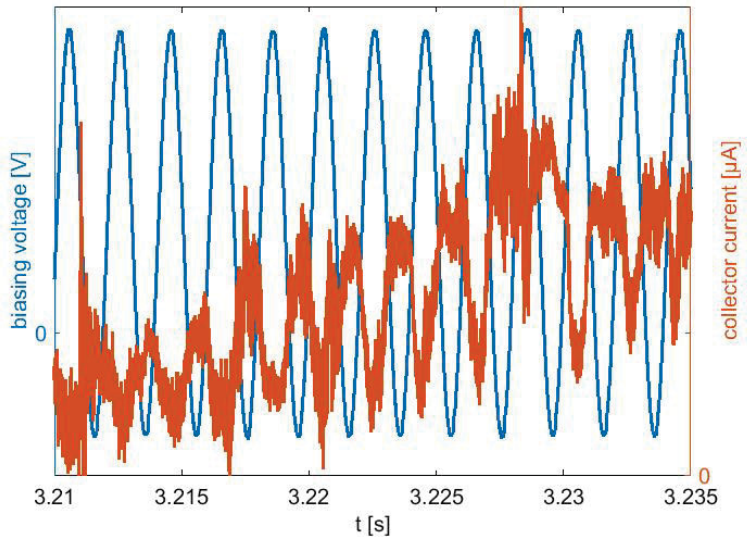

Figure 41: Biasing (blue) and a I-U curve (red) affected by a strong positive floating potential.

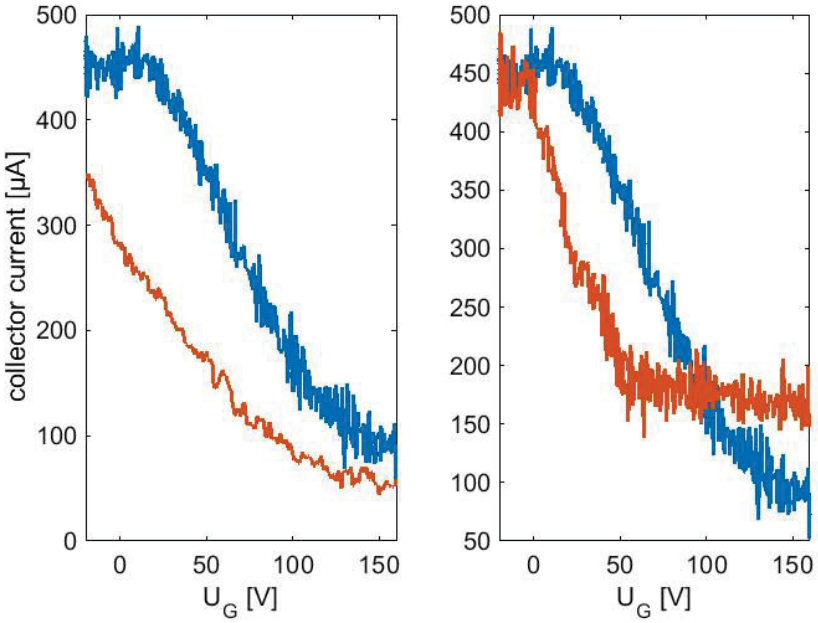

Figure 42: Each subplot one normal I-U curve (blue) and one I-U curve (red) affected by potentials. Left: saturation current is not reached, right: current saturates for positive U_G.

Afterwards, the parameters with highest coefficient of determination were used. One example fit is shown in figure 43.

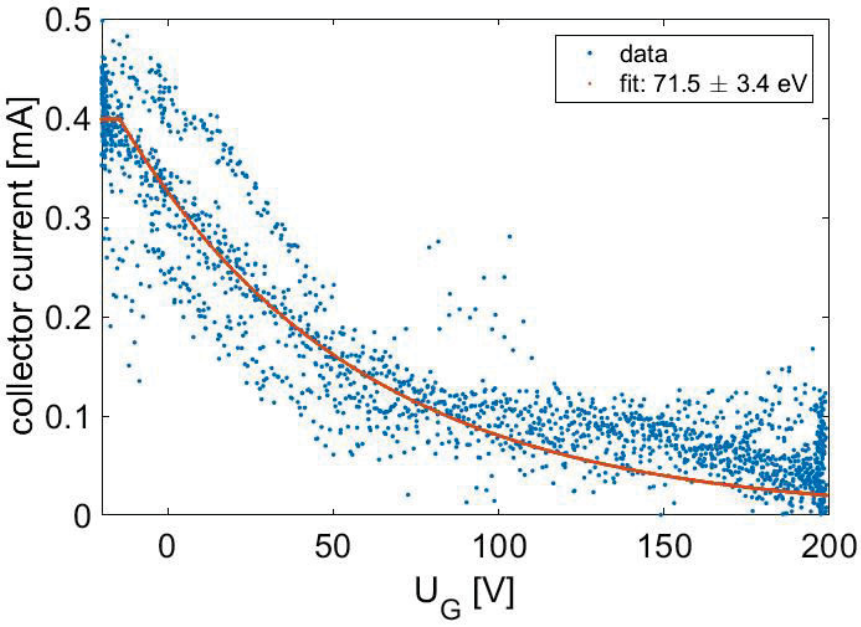

Figure 43: Exemplary low pass filtered collector current for channel 23 and temperature fit.

The electron temperature profile is calculated using the V_f and V_+ pins on top of the probe. In figure 44, it can be seen that the electron temperature peaks at the border between long and short connection length region. However, a drop in the expected maximum of the peak is given, which is consistent in all measurements with the multi-channel RFA probe, but not seen in other diagnostics data and cannot yet be expained.

Furthermore, in figure 44 it can be seen that the fitted ion temperature profiles for up- and downstream directions have a different ion temperature. Channel 11 and 12, which had higher noise level, also had higher temperatures, which indicates a stronger modification of the energy distribution of the ions by the probe head. Usually, the ion temperature of both directions is used to calculate a more precise T_i value. However, not all channels had signal in the second divertor campaign. That is why channel 23 is preferred for further studies in chapter 6.

Summarised, a retarding field analyzer probe has been developed for the first time for the W7-X stellarator boundary plasma. Altough some channels did not have signal, the multi-channel feasibility is shown.

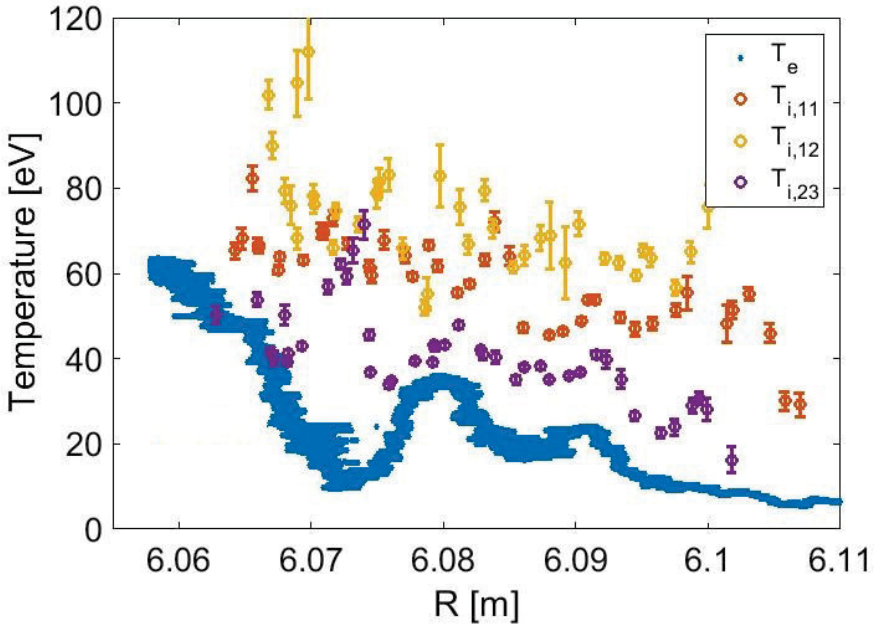

Figure 44: Ion temperature profiles for the channels 11, 12 and 23 and electron temperature profile. (#180905.015 @ 18.0-18.3 s)

4.2.3 Troubles and their rectification with the multi-channel retarding field analyzer

During the commisioning and the experiments, various troubles appeared while using the multi-channel retarding field analyzer. To avoid repetition in future work, the most important troubles and their rectifications are shortly summarised in the following:

No signal in the RFA channels:

During experiments in the tokamak EAST, lithium coating was applied to improve the plasma stability during the campaign. Unfortunately, the probe was coated as well. This leads to a blocking of the slits in the first slit plate.

To remove such blocking, the RFA probe was heated several times, plunging deeply into the plasma edge.

Capacity effects:

As already shown in chapter 4.1.2, a capacity current will be induced on the collector plates, driven by the sweeping of the second grid biasing. However, such an effect can also be observed between RFA modules and Langmuir pin system. Due to separated

biasing for the RFA modules and the pins, both capacity currents were superposed in both diagnostic parts.

The best way is to solve this, is a triple-pin arrangement, like used during the second divertor campaign on the W7-X stellarator. In this case, no capacity effects from the pins are induced and the capacity current of the RFA modules can be subtracted by filtering the sweeping frequency.

If this is not possible due to limited probe size, both biasings should be coupled, to avoid phase shift.

Arcing inside the probe head:

Usually, the probe should be heated before experiments, to remove gas inside the probe head and coating from the surface. However, during the first divertor campaign on the W7-X stellarator, gas was left inside the probe head. During the first planges, this remaining gas induced arcing between the grids. Due to the resistance being too low between both grids, this arcing burned holes into the grids. (see [32])

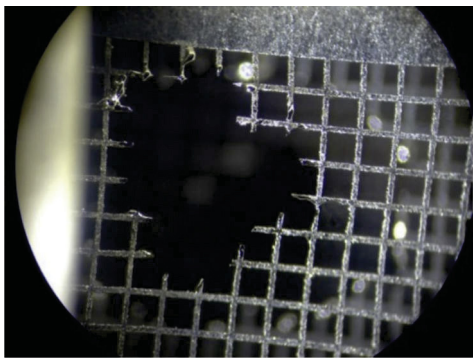

Figure 45: Destroyed grid from the multi-channel RFA probe during the first divertor campaign on W7-X stellarator.

To avoid such destructive arcing in the second divertor campaign on the W7-X stellarator, a resistance of 1 kΩ was added in the electronics between both grids.

Electron emmision due to high probe temperature:

During the second divertor campaign on the stellarator W7-X, a drop in the measurements was observed for several manipulator probes while plunging deep into the SOL region, as shown in chapter 4.2.2.

The most likely reason is electron emmission and, as a result, a potential change in case of high probe temperature. As can be seen in figure 46, the probe temperature

increased rapidly, crossing a certain position with high plasma edge temperatures and stayed at a high temperate for the rest of the plunge.

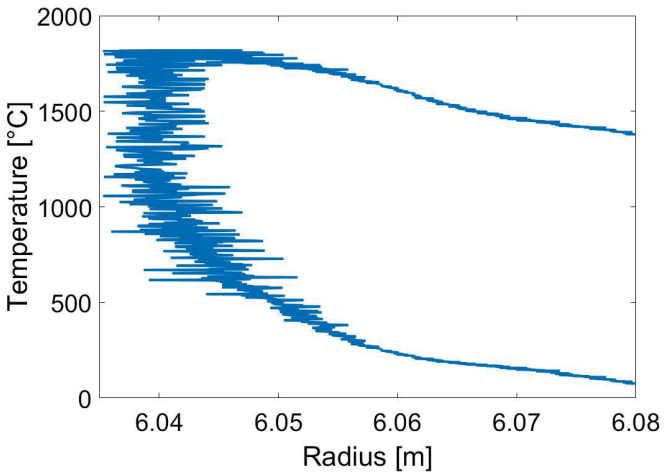

Figure 46: Calculated probe surface temperature during the second divertor camapign on W7-X stellarator. (#180814.047)

High surface temperatures can not be avoided. However, the pin material will be changed to graphite for the next campaigns, to reduce the emmisive effects.

High floating potentials:

Floating potentials can have an influence on several things. First, the probe cover should be made by non-conductive material (like Boron nitride on W7-X stellerator). Experiments during the first divertor campaign on W7-X stellarator showed, that a grounded cover induced additional current flow from plasma to the cover and thereby changed the plasma conditions massively. That's why the experiments were continued with floated probe cover.

However, the potential of this probe cover could have an influence on the measurements. If e.g. the cover potential is higher than the local plasma potential at the RFA channel position, due to the length of several centimetres, ions could be reflected before entering the probe head and the measured thermal energy distribution will be modified. Also, if the collector biasing is below the plasma potential, such a modification can be obvserved.

In addition, the floating potential shifts the effective biasing, due to the fixed grounding of the biasing (see chapter 4.2.2). If a high positive or negative floating potential

appears in the SOL region, the ions cannot be against or the saturation current cannot be reached anymore.

To solve this problem, the biasing has to be adjusted to the expected SOL floating potential range, using:

$$U_{\mathrm{f}} > U_{\mathrm{slits}} > U_{\mathrm{collector}} \tag{4.4}$$

Further, a DC biasing will be added in the next W7-X camapigns, to reach:

$$U_{\mathrm{biasing}} \geq \max\left(U_{\mathrm{f}}\right) + 3T_i \tag{4.5}$$

5 Fast particle measurements during ELM crashes in the plasma edge of EAST tokamak

This chapter describes the measurements of fast particles in the outer midplane during the 2016 campaign on EAST tokamak. To measure them, the middle grid biasing is set at a fixed potential (usually $\geq$ 3Ti) for both modules of the multi-channel RFA probe, in order to repel all thermal particles. Several previous experiments have shown that retarding field analyzers are a good opportunity to measure fast particles in the SOL region (e.g. [28]). However, no publication could be found, explaining why fast ion dominated losses can be detected earlier than fast electron dominated losses during ELM crashes, as was measured in the 2016 campaign on EAST tokamak [31]. Therefore, this measurements will be examined in more detail in this chapter.

First, the plasma conditions and the occurring magntic mode will be shown. Further, it will be shown that magnetic reconnection drives fast electrons and ions and leads to its loss after ELM crash.

Furthermore, the location of origin and the propagation of fast ions and fast electrons in the plasma core will be shown, using neutral particle analyzers and heterodyne radiometers. Using divertor Langmuir probes and the developed multi-channel RFA probe, the propagation in the SOL region and the different behaviours of both species will be shown.

Last, it will be shown, that a fast ion postcursor appears, which is not present in the magnetic signal.

5.1 Experimental set-up and edge localised mode

During these experiments, deuterium plasmas were used with a plasma current of 500 kA and a toroidal magnetic field coil current of 11 kA. Further, an upper single-null configuration was chosen. These discharges had a density of $3.4 \cdot 10^{19}$ m^{-3} and were heated ohmically and by lower hybrid wave heating. Providing a heating power of $P_{\mathrm{ECRH}} = 0.4$ MW and co- and counter directed neutral beam injection with 55-60 kV, ELMs could be seen.

It can be found, that ELM related peaks in the magnetic signal (Minorv coils), the presence of fast particles at the RFA probe, and ELM related peaks in the divertor balmer alpha lines (filterscope) correlates. This indicates that the fast particles are driven by the ELM crash.

Although, various types of ELM crashes were measured during experiments, only in approximately 10% were fast particles detected. Always, magnetic precursors preceded ELM crashes with fast particles in the SOL region, as shown in figure 47.

In figure 47a the signal of a poloidal distributed mirnov coil array and in figure 47b the mirnov coil signal in the outer midplane is shown. It can be seen, that a magnetic mode arises. While the magnetic perturbation increases (see figure 47d), measured by the Mirnov coils, the poloidal rotating frequency always decreases to approximately 2 kHz (see figure 47c). Becoming unstable leads to magnetic reconnection, which causes high particle and energy losses from the confined region to the SOL region.

Using an array of 26 poloidally distributed mirnov coils, a poloidal periodicity of three can be found. However, in toroidal direction, only two coils were availible, due to the lower sampling rate of the toroidal coil array. The signal of both opposite mirnov coils in the outer midplane and the signal of a neutral particle anaylzer for fast ions in the midplane is shown in figure 48. It can be seen, that both mirnov coil signals have an opposite phase to each other. Assuming that the modification of the fast ion contribution, measured by the neutral particle analyzer, depence on the magnetic perturbation, as well a toroidal perodicity of three can be found.

Using ECE measurements (heterodyne radiometer) for fast electrons in the the plasma core region at the port P [3], a low-field mode can be found at $R = 2139.4 \pm 10.0$ cm to $R = 2273.7 \pm 9.2$ mm in the outer midplane (see fig. 51).

[3] The EAST device is devided into 15 modules, each with one outer midplane port. Therefore, the modules are called port A to port P, as shown in [47]

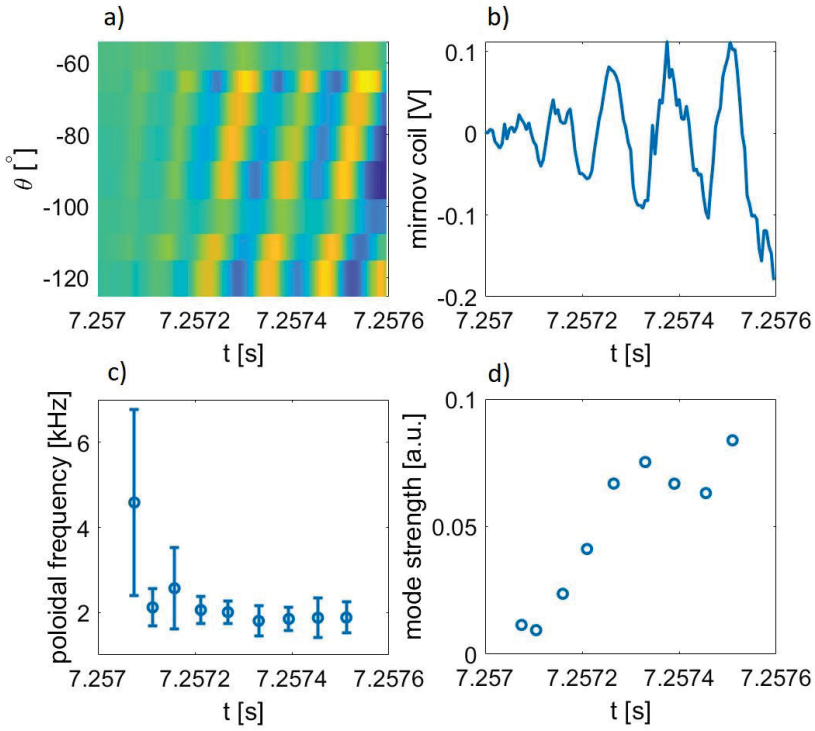

Figure 47: Exemplary magnetic precursor during ELM experiments in the C port of EAST tokamak. a) signal of poloidal mirnov coil array, b) mirnov coil signal in outer midplane, c) poloidal rotation frequency, d) mode strength (#70766)

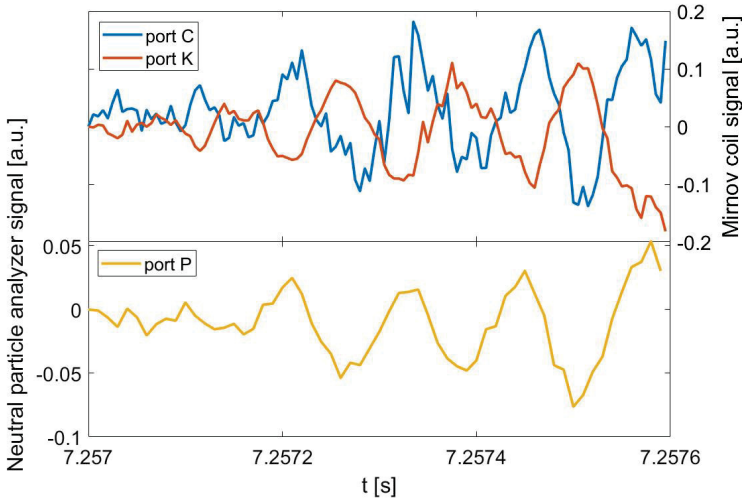

Figure 48: Mirnov coil signal for two opposite ports and neutral particle analyzer signal during magnetic precursor. (#70766)

However, the mode of the fast ion signal is invard shifted. Using the neutral particle analyzer, the low-field side mode in the outer midplane can be found at $R = 2185.5 \pm 58.1$ mm to $R = 2032.8 \pm 32.7$ mm (see figure 51).

5.2 Formation and propagation of fast particles

Similar to the neutral particle analyzer (NPA), the ECE signal can be used as indicator for fast electrons, due to its sensitivity to fast particles. Both fast ions and electrons are superposed to the thermal plasma background. The ELM crash leads to a drop in the ECE signal in the outer plasma core. Afterwards, a narrow peak in the outer channels of the neutral particle analyzer and the heterodyne radiometer can be found (see fig. 49), which shows the presence of fast particles.

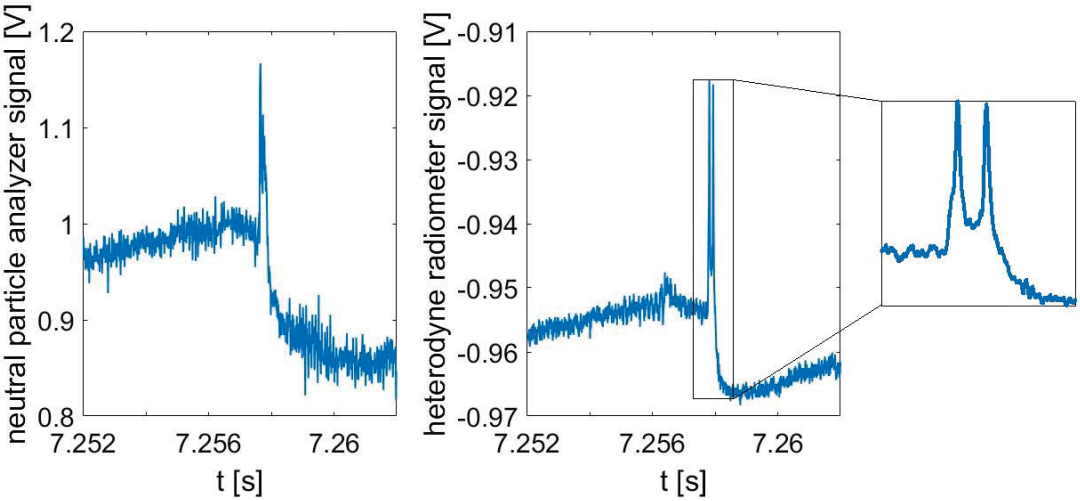

Figure 49: Neutral particle analyzer signal for fast ions and heterodyne radiometer signal for fast electrons in the outer channels during ELM. (#70766)

In the ECE signal, it can be seen that a double peak occurs. Both peaks have a time delay of 95 µs. On the other side, only one peak occurs in the NPA signal.

In figure 50, the signal of the horizontal neutral particle analyzer located in the midplane of port P is shown, in which the white line indicates the ELM crash measured by the mirnov coils. A strong fast ion contribution appears after the crash, most likely driven by magnetic reconnection during the crash. Because such a peak can not be found in the vertical neutral particle analyzer and inner horiontal line of sights, it can be assumed that the fast ions are moving mostly parallel to the magnetic field lines.

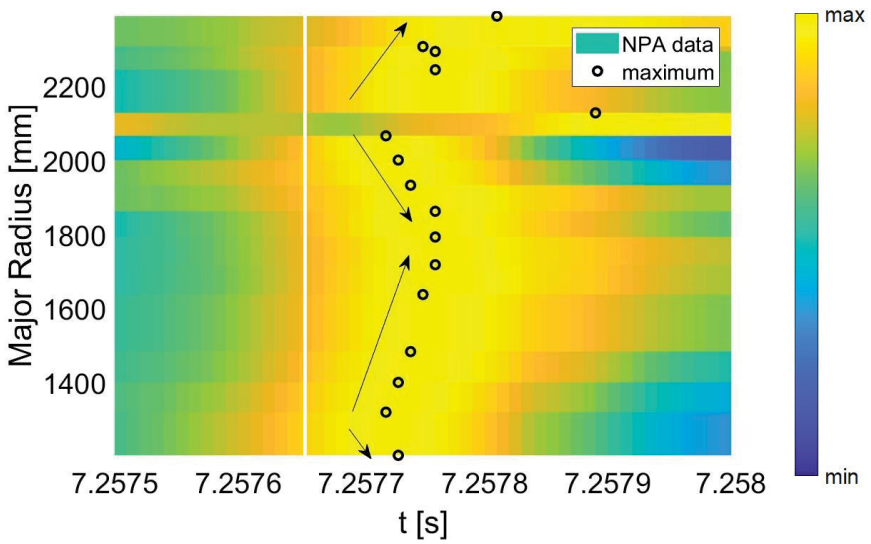

Figure 50: Neutral particle analyzer signal after the ELM crash. Peak maxima marked with circles. Propagation of fast ions indicated by arrows. (#70766)

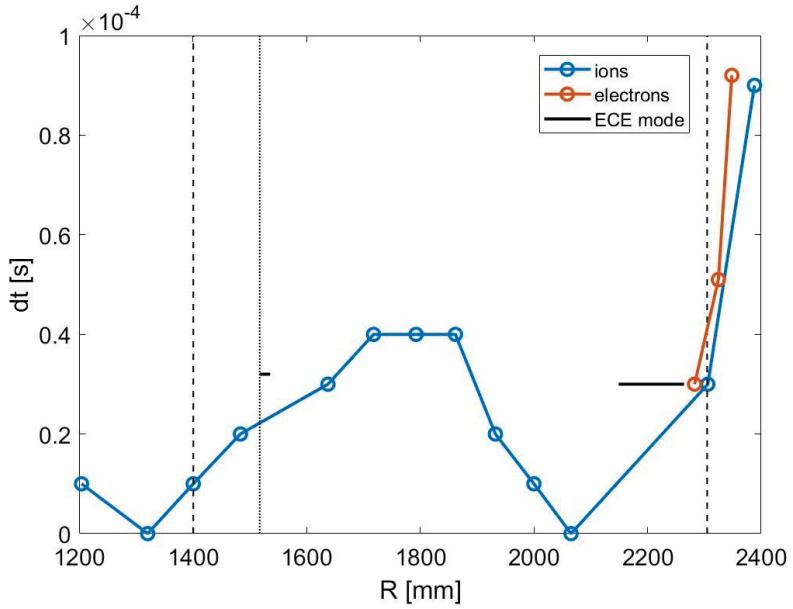

Figure 51: Time delay between peak maximum of the signals from the neutral particle analyzer for fast ions and from the heterodyne radiometer for the ECE signal (including fast electrons), supplemented by the position of the confined electron mode during ELM (ECE mode). The dashed lines indicate the LCFS and the dotted line is the lower limit of the heterodyne radiometer signal. (#70766)

That's why the locations of the fast ions for the different channels are approximated as the tangential point between line of sight and field line.

Accordingly, fast ions were observed first at 2065.5 ± 65.3 mm and then propagating outwards with an average radial velocity of 7.8 km/s, as indicated by the arrows. Afterwards, the signal of the heterodyne radiometer drops, indicating fast heat losses of confined electrons. This ELM related mode in the electron signal (ECE mode) crashes if the fast ions cross the mode location (as shown in figure 51). In the SOL region, the fast electrons are propagating outwards with a velocity of 1.7 km/s and the fast ions propagating outwards with a velocity of 1.4 km/s.

5.3 Fast particles in the SOL region

In figure 52, the signals of two opposite RFA channels are shown. The RFA signals can be split into two parts.

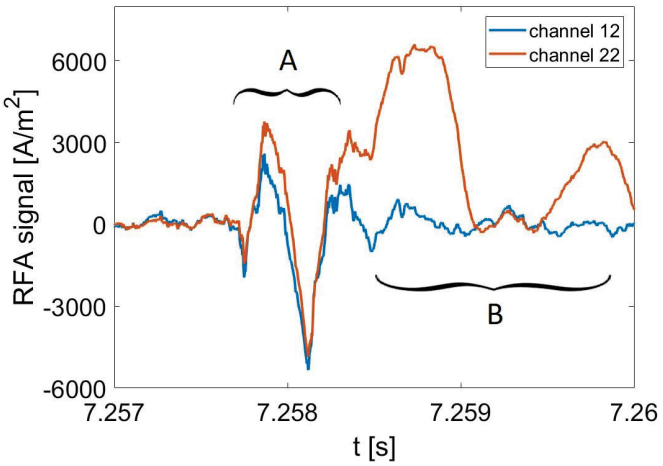

Figure 52: Signal of two opposite MC-RFA channels. (#70766)

The collector current, marked with A, is similar for channels parallel and anti-parallel to the magnetic field lines. It's a narrow peak, which indicates fast particle measurements due to the quick loss of them. It was found, that first a dominating fast ion contribution (positive signal) can be seen, followed by a dominating fast electron contribution (negative signal).

In contrast, the collector current, marked with B, is broader and different for measurements which were done parallel and anti-parallel to the magnetic field lines. Due

to the different plasma flow given by temperature distribution and ion sound speed, this indicates a thermal contribution, which is heated above the RFA biasing by the magnetic reconnection and outwards transport.

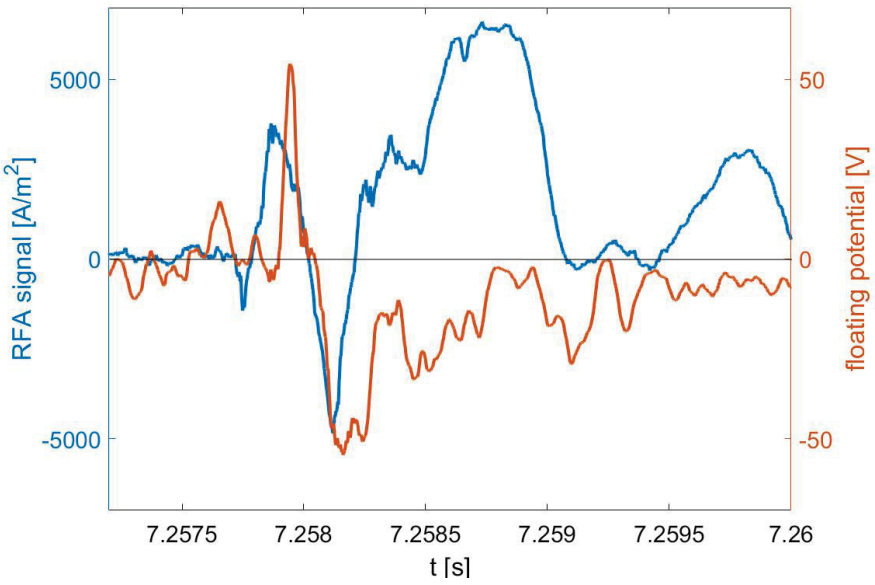

Figure 53: RFA collector current and floating potential measured with the MC-RFA probe. (#70766)

Due to the susceptibility of the floating potential on the total ion and electron saturation current [56], the floating potential is sensitive on fast particles, which are superposed to the saturation current of the thermal particles. This effect can be used to detect fast particle appearance without measuring it directly.

As shown in figure 53, the floating potential, measured by the MC-RFA probe, rises up to 55 eV during the first ion dominated peak in the RFA collector current. Though, such a narrow positive strikeline cannot be found in the floating potential measurements at the upper and lower divertor (see figure 54). Hence, the fast ions propagate horizontally outwards and do not follow the field lines due to the larger Larmor radius and mass.

Further, a narrow negative strikeline in the floating potential, corresponding to the negative peak in the floating potential measures by the MC-RFA probe, appears in the upper divertor, but not in the lower divertor. because of the so-called upper single-null configuartion during these experiments, this observation fits to the assumption that the fast electrons follow the magnetic field lines.

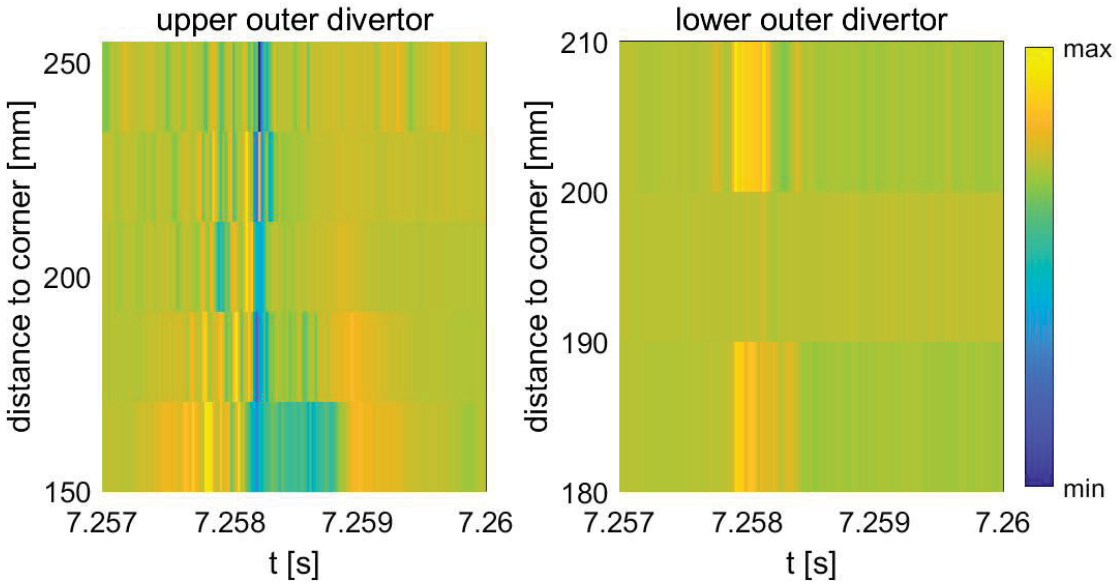

Figure 54: Floating potential measured by the Langmuir probe arrays at the upper and lower divertor. Left: Upper divertor at port O, right: lower divertor at port D. (#70766)

5.4 Post-ELM signals

As mentioned in the previous chapter, a second type of signal (see type B in figure 52) can be observed after the fast particle contributions. Such a post-ELM cursor can be found in the signal of the vertical neutral particle analyzers, as shown in figure 55, and the RFA probe, as shown in figure 52.

Because the modulation of the vertical NPA signal with a frequency of 1.1 kHz is much smaller than the modulation in the horizontal probes after ELM carsh, and the observation is not tangential to the magnetic field lines, the most likely reason is a modulation in the ion temperature and therefore in the fast ion contribution. It can be seen that no phase difference between the different channels is given, but a phase difference between both ports. This indicates a pure toroidal mode in the ion temperature.

Because no such a post-ELM modulation can be found in the ECE signal, and no negative modulation in the RFA signal is observed, likely no electron temperature post-ELM mode occurs.

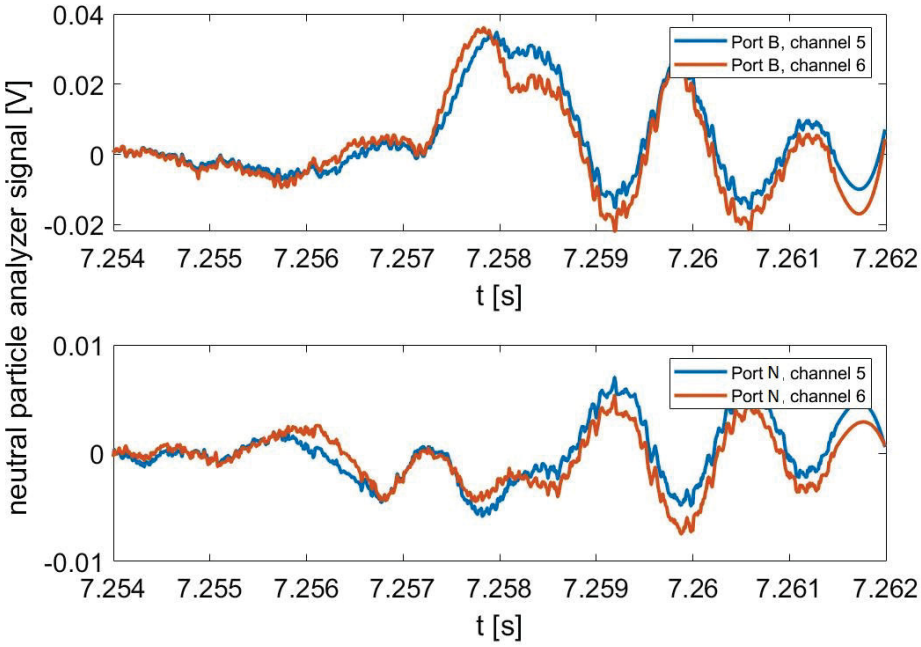

Figure 55: Post-ELM signals of the vertical neutral particle analyzers. (#70766)

However, the fast ion driven modulation in the RFA signal has a slightly lower frequency of 0.9 kHz, which indicates a deceleration in the SOL region.

5.5 Summary

The first positive peak is dominated by the fast ions driven by magnetic reconnection and detected by the neutral particle analyzer. The fast ions are propagation horizontally outwards and therefore cannot be detected in the upper or lower divertor region.

The first peak in the fast electron signal, measured by the heterodyne radiometer, is superposed to a stronger fast ion signal and therefore can not be detected by the RFA probe. In contrast, the second peak with a time delay of 95 µs can be observed in the RFA signal.

Further, a post-ELM mode in the ion temperature, but not in the electron temperature is shown.

6 Ion temperature measurements in the plasma edge of W7-X stellarator

This chapter describes the measurements of electron temperature and ion temperature profiles in the edge island of the W7-X stellarator during the second divertor campaign in 2018. In the previous campaigns, no measurements for ion temperatures in the SOL region of the W7-X stellarator were available [18]. Therefore, during these experiments, the standard configuration ($n/m = 5/5$ island) was used. Adding control coil currents, the island size could be adjusted. In the following, the ion temperature and electron temperature profiles inside the edge island will be investigated.

In the first part, the plasma conditions and the magnetic edge island will be described. Further, it will be shown that additional control coil currents shift the O-point outwards and therefore reduce the distance between O-point and border between the long and short connections length region

The influence of this decreased effective island size on the electron and ion temperature profiles was measured and will be shown in the second part.

Following, the interplay between plasma collisionality and the ratio between ion temperature and ectron temperature was calculated and will be shown in the third part.

6.1 Plasma condition and edge island topology

During these experiments, hydrogen plasmas were used with a magnetic field of 2.5 T at the magnetic axis and a density of $9{\cdot}10^{19}$ m^{-3}, controlled by gas puffing. The discharges were heated by electron cyclotron resonance heating (ECRH) with $P_{\mathrm{ECRH}} = 3.1$ MW.

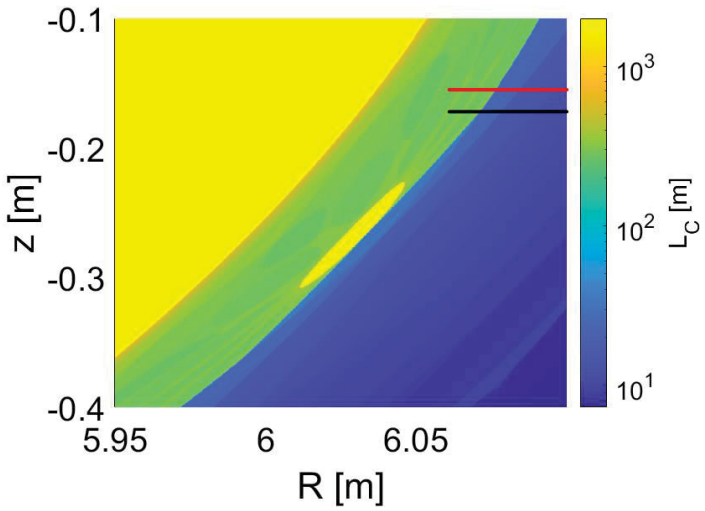

Figure 56: Connection length in the SOL region of the W7-X stellarator in standard configuration, defined by the magnetic edge island topology. Red line: MC-RFA measurements, black line: MPM line of motion and combined probe measurements by Drews [18].

For ion temperature measurements during the second campaign, the standard configuration was used, which allows comparision with the so-called combined probe measurements [18]. In this configuration, a iota value of 1.0 occurs in the plasma edge, which leads to 5/5 magnetic edge islands. As shown in figure 56, the island topology can be devided into closed field lines at the O point (yellow), field lines with long connection length (green) and field lines with short connection length (blue), due to the intersection of these edge islands by different divertor modules.

Although the total island size is increasing with increasing control coil current, the O-point is shifted outwards and the distance between O-point and border between long and short connection length region is decreasing. Consequently, the flattening in the temperature profiles behave like in smaller island width. This effect will be used for the studies in this chapter.

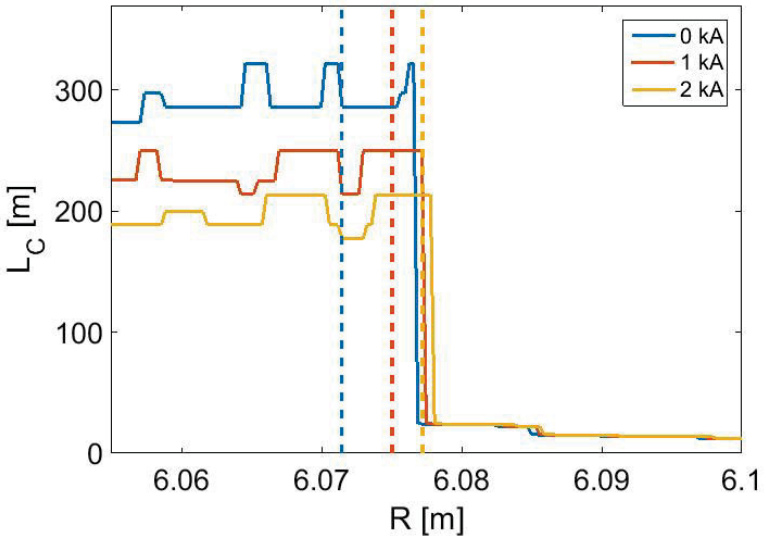

Figure 57: Connection length profiles for standard configuration and different control coil currents at RFA position, supplemented by the position of the corresponding flux surface closest to the O-Point.

Using the MC-RFA probe, the ion temperature and electron temperature profiles inside the edge island were measured. For this, the multi-purpose manipulator (MPM) [54] at the toroidal position $\theta = -159.26°$ and the outer midplane at $z = -0.171$ m was used in between the characteristic bean shaped and triangular shaped cross-section. As shown in figure 56, the manipulator is located between the X and O point. However, the different pins and RFA channels are not located at the same line of motion, due to the tilt of the island surfaces. Hence, the calculated profiles will be projected to the line of motion of the center of the probe top surface at $z = -0.147$ m for comparission.

6.2 Ion temperature and electron temperature profiles inside the edge island

The electron temperature measurements with the triple Langmuir probe had a time resolution of 1 MHz, whereas the ion temperature measurements from the RFA modules had a sweeping frequency of 1 kHZ and a sampling frequency of 1 MHz.

Plunging the MPM, allows to measure the profiles along the line of motion (see figure 56). An example for the standard configuration without additional control coil currents is shown in figure 58.

In these experiments, a spatial resolution of 1.8 mm for the ion temperature was reached. Further, the length of the Larmuir pins of 3.0 mm leads to a smoothing of the electron temperature measurements. During these discharges, the RFA probe did not cross the LCFS, due to safety reasons. However, the point of the line of motion closest to the O-point is crossed. Therefore, the ion to electron temperature ratio inside the island can be calculated.

Due to emission processes for high temperatures (like [18]), the electron profile drops in high electron temperature regions. Therefore, the drop at the maximum of the island peak and inside the LCFS do not fit to the actual electron profile. Hence, EMC3-Eirene calculations must be used for further studies, to bridge this part.

It can be seen that the electron temperature profile peaks at the border between short and long connection length, as also seen in the previous campaign [17]. Further, a drop in the electron temperature profile inside the island indicates that the heat transport in the island is dominated by parallel transport along the magnetic field lines, which connects the inner and outer island separatrix and propagates from the separatrix to the O point.

However, such a drop is not visible in the ion temperature profile inside the island. Due to the larger Larmor radius of the ions and the higher diffusion coefficent, the heat transport perpendicular to the field lines and therefore accross the island is higher and the profile is flattened.

Further, because both ions and electrons have the same density due to quasi-neutrality in the island SOL region, the perpendicular heat transport of ions is usually higher ($\Xi_i > \Xi_e$). This leads to a larger decay length and $T_i > T_e$ in the far SOL region.

This flattening of the ion temperarture profile is consistent for all added control coil currents and plasma parameters during RFA experiments during the second divertor campaign. However, the peak profile of the electron temperature depends on the control coil current, as shown in figure 59.

Although the island size increases with increasing control coil currents, the ratio between peak maximum at the border between short and long connection length and minimum at the field line closest to the O-point is decreasing. This observation can be

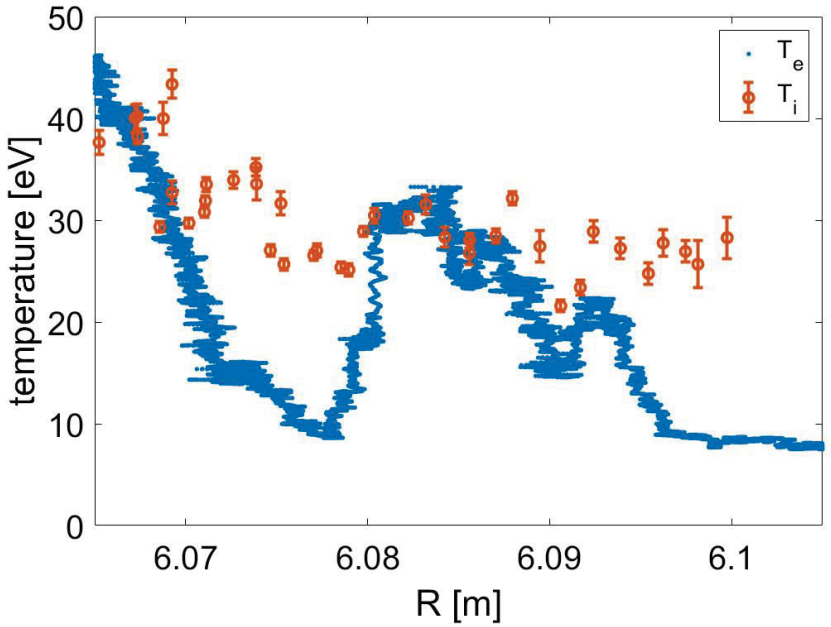

Figure 58: Electron and ion temperature profile in the SOL region of the W7-X stellarator in standard configuration. (#180905.015 @ 18.0-18.3 s)

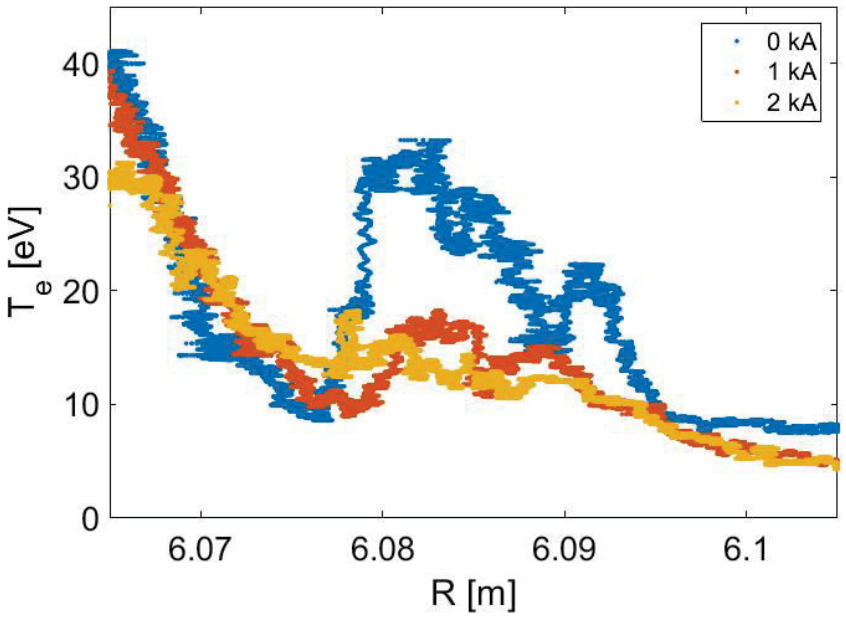

Figure 59: Electron temperature profiles in the SOL region of the W7-X stellarator in standard configuration with different additional control coil currents. (#180905.013-.015 @ 18.0-18.3 s)

explained by the intersection of the field lines by divertors. The field lines closest to the O-Point are always located in the long connection length region. In contrast, the field lines closest to the separatrix are split into long and short connection length regions. Therefore, the transport between inner and outer separatrix is not given by parallel heat transport, which is much higher than perpendicular heat transport. That's why the peaking mostly depends on the flux surfaces, which are completely located in the long connection length region.

As shown in figure 57, if a control coil current was added, the O-Point was shifted outwards and the distance to the border between both connection length regions decreased. This leads to a flattening of the peak in the electron temperature profile and lower plasma collisionality in the island structure. The resulting electron to ion temperature ratios are investigated in the following.

6.3 Ion temperature to electron temperature ratio in dependence on control coil currents

Because no direct heating mechanisms for ions were available in the second divertor campaign, the heat source is only given by convective and conductive transport from electrons to ions.

As shown in figure 60, the ion to electron temperature ratio for $\nu^* < 10$ in the short connection length region (circles) is approximately 1. In this parametric region, the conductive heat transport is dominant and is driven by the particle transport.

In constrast, the ion to electron temperature ratio for $\nu^* > 10$ in the long connection length region (triangles) is increasing. Although no direct dependence between the electron temperature drop and therefore the ion to electron temperature ratio and the plasma collisionality is given, both are coupled.

As already mentioned, the ion temperature flattened due to the larger Larmor radius compared to electrons and the higher resulting radial transport.

However, the Larmor radius of electrons is much smaller and therefore the parallel transport dominates. As result, the electron temperature drops in the island structure. Because of the dependency of $\nu_{ei} \sim T^{-1.5} \rightarrow \nu^* \sim T^{-2}$, the plasma collisionality increases in this region.

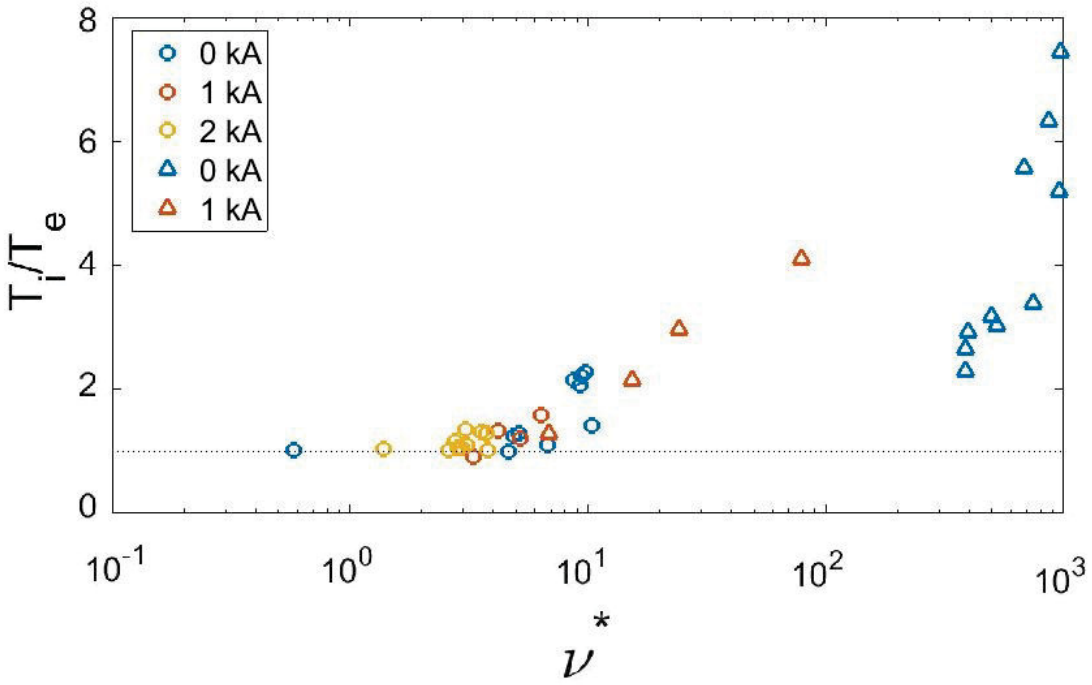

Figure 60: Ion to electron temperature ratio at the position closest to the O-point (triangles) and at the border between short and long connection length (circles) in the SOL region of the W7-X stellarator in standard configuration with different additional control coil currents. (#180905.007-.028)

Further, the decay of electron density and electron temperature inside the island region can be approximated with $\lambda_T = \frac{\nu^*}{60}\lambda_n$ [24] and leads to flattening for increasing ν^*.

The resulting electron temperature and therefore the resulting ion to electron temperature ratio is an equilibrium between both mechanisms and depends on several parameters, like topology and plasma parameters.

6.4 Summary

Summarised, it was observed that the ion temperature profile flattened in the island region. In contrast, the electron temperature profile has a peak at the border between short and long connection length regions and a drop closest to the O-point. This shows that the electron heat transport is dominated by parallel transport and the ion heat transport is dominated by perpendicular transport in the island structure.

Further, the flattening can be increased and the ion to lectron temperature ratio can be decreased, shifting the O-point closer to the short connection length region.

The observed ion to electron temperature ratios in the long connection length region are mostly defined by the drop in the electron temperature profile, which is defined by an equlibrium of flattening of the electron temperature profile with high plasma collisionality and increase of the plasma collisionality in the electron temperature drop.

7 Conclusion

The aim of this thesis was the commissioning of a multi-channel retarding field analyzer and measurements of ion temperature as well as fast particles in the scrape-off layer region. This thesis included:

- Designing and commissioning of a multi-channel retarding field analyzer
- Optimising the multi-channel retarding field analyzer based on experience during experiments and numerical simulations
- Measurements of fast particles in ELMy plasmas on the tokamak EAST
- Measurements of ion temperature in edge islands on the stellarator W7-X

A multi-channel retarding field analyzer for ion temperature and fast particle measurements in the SOL region was developed and commissioned in the tokamak EAST during the 2016 and 2017 campaigns. For ion temperature measurements in the stellarator W7-X, an advanced and optimised probe was built and used for the second divertor campaign in 2018.

Starting with a simple 2-channel probe design on the linear device PSI-2 and continuing with a 6-channel retarding field analyzer on the tokamak EAST, the multi-channel feasibility was shown. Between the EAST and W7-X experiments, the channel slits were narrowed and the inner grid modules were optimised, to improve the measurements. In addition, a set of pins on the top of the probe were used to measure the floating potential, ion saturation current, and electron temperature. Using a two pin arrangement during the EAST experiments, showed capacitive effects on the RFA channels. Consequently, a five pin arrangement was used for W7-X experiments. Thereby, the time and spacial resolution could be increased by a factor of 10^3.

The developed multi-channel retarding field analyzer was used for fast particle measurements in the scrape-off layer of the tokamak EAST. For this, the probe biasing was set on a fixed value to repel all thermal particles. Measurements during ELM showed the appearance of fast ions and fast electrons in case of a magnetic precursor. Using the mirnov coil signals, the solid state neutral particle analyzer, and the heterodyne radiometer, the propagation of fast electrons and fast ions after an ELM burst could be determined and it could be shown that the fast ions were generated earlier, and that the fast particles destabilised the electron based mode. However, both types of parti-

cles propagating with approximately same velocity in the scrape-off layer region. Using this knowledge, the observation, made by the retarding field analyzer probe, could be explained. Further, the localised propagation of lost fast ions in horizontal direction were shown, using the retarding field anaylzer and the divertor Langmuir probes. Because the edge localised modes are sensitive on the safety factor, further studies should be focused on the dependence of the fast particle appearance and propagation on the edge saftey factor on EAST tokamak. Especially the location of origin is of particular interest.

Further, the multi-channel retarding field analyzer was used for electron and ion temperature measurements in the scrape-off layer of the stellarator W7-X during the second divertor campaign. The measurements showed that the ion temperature profiles flattened for the given conditions, during the second divertort campaign. On the other side, the electron temperature profile peaks, due to an eqilibrium between dominated parallel heat transport and temperature decay coupled to the plasma collisionality. Furthermore, it was shown that the ion to electron temperature ratio inside the island structure can be decreased by using additional control coil currents. However, further studies on the effect of the plasma collisionality on the ion to electron temperature ratio in different magnetic configuartions should be done, due to the limited number of discharges during the second divertor campaign. Additionally, simulations with the EMC3-Eirene code could be a great completion.

Despite several optimisations, some work still have to be done in future. Although several publications mentioned an upper limit for the slit width, no experimental verifications were possible yet. Further, the biasing must be optimised, to remain operable in high potential scrape-off layer.

All in all, the multi-channel retarding field analyzer is flexible in its application. Using different biasing, it is possible to switch between fast particle and ion temperature operation. This enables broad knowledge about both types of particles in the scrape-off layer of stellarator and tokamak.

List of Figures

References

[1] A. Ando et al: *Evaluation of Mach probe characteristics and measurement of high-Mach-number plasma flow*, Thin Solid Films (2006)

[2] T. Andreeva et al: *Characteristics of main configurations of Wendelstein 7-X*, Problems of Atomic Science and Technology. Series: Plasma Physics (2002)

[3] T. Arber: *Fundamentals of Magnetohydrodynamics*, STFC Advanced School, University of Warwick (2013)

[4] D. Bohm: *The characteristics of electrical discharges in magnetic fields*, A. Guthrie and R. K. Wakerling (eds.), New York: McGraw-Hill (1949)

[5] A. H. Boozer: *Time-dependent drfit Hamiltonian*, The Physics of Fluids 27 (1984)

[6] E. Borie: *Einführung in die Plasmaphysik*, Forschungszentrum Karlsruhe (2005)

[7] S. I. Braginskii: *Transport processes in a plasma*, Reviews of Plasma Physics Volume 1 (1965)

[8] M. Brix: *Messung von Elektronentemperatur und -dichte mittels Heliumstrahldiagnostik im Randschichtplasma eines Tokamaks*, Schriften des Forschungszentrum Jülich, Reihe Energie & Umwelt, Band 307 (1998)

[9] D. Brunner et al.: *Scanning retarding field analyzer for plasma profile measurements in the boundary of the Alcator C-Mod tokamak*, Review of scientific instruments (2013)

[10] F. F. Chen: *Plasma physics and controlled fusion, Volume 1: Plasma physics*, Plenum Press, New York (1984)

[11] S. L. Chen et al: *Effect of three-dimentinal conducting strucures on vertical stability in EAST*, Nuclear Fusion 55, 013010 (2015)

[12] B. V. Chirikov: *A universal instability of many-dimensional oscillator systems*, Physics Reports 52 (1979)

[13] D. P. Coster: *Extensions to the SOLPS edge plasma simulation code to include additional surface interaction possibilities*, Workshop on New Directions for Advanced Computer Simulations and Experiments in Fusion-Related Plasma-Surface Interactions (2005)

[14] S. C. Cowley: *The quest for fusion power*, Nature physics Volume 12 ((2016)

[15] T. Denner: *Verteilung des Wärmeflusses auf eine optimierte Limiteroberfläche and Struktur der Plasmarandschicht*, Berichte des Forschungszentrum Jülich (1998)

[16] P. Drewelow: *Investigation of Divertor Heat Flux Pattern and their Correlation to the Edge Magnetic Field of the Plasma Confinement Experiment LHD*, Technische Universität Berlin (2013)

[17] P. Drews et al.: *Measurement of the plasma edge profiles using the combined probe on W7-X*, Nuclear fusion 57 (2017)

[18] P. Drews: *The role of magnetic topology in the edge plasma performance on W7-X*, Heinrich-Heine-Universität Düsseldorf (2019)

[19] R. Dux: *Plasmaphysik und Fusionsforschung*, Lecture notes of university Augsburg (2002)

[20] S. Elmore et al: *Upstream and divertor ion temperature measurements on MAST by retarding field energy analyser*, Plasma physics and controlled fusion (2012)

[21] https://www.euro-fusion.org/wpcms/wp-content/uploads/2011/07/fig04.jpg (2016)

[22] N. Ezumi et al: *Particle transport measurements in the LHD stochastic magnetic boundary plasma using Mach probes and ion sensitive probe*, Journal of Nuclear Materials 415 (2011)

[23] R. Fitzpatrick: *Linear and nonlinear response of a rotating tokamak plasma to a resonant error-field*, Physics of plasmas 21 (2014)

[24] W. Fundamenski: *Scrape-off layer transport on JET*, Fusion science and technology, Vol. 53 (2008)

[25] G. Fußmann: *Einführung in die Plasmaphysik*, Humboldt Universität zu Berlin (2005)

[26] O. Gruber et al: *Observation of Continuous Divertor Detachment in H-Mode Discharges in ASDEX Upgrade*, Physical review letters 74 (1995)

[27] K. Guangli, S. Jiafang: *Lower Hybrid Current Drive System*, http://east.ipp.ac.cn (2016)

[28] N. Gulbrandsen, Å. Fredriksen: *RFEA Measurements of High-Energy Electrons in a Helicon Plasma Device with Expanding Magnetic Field*, Frontier in Physics 5:2 (2017)

[29] D. Harting, Detlev Reiter: *3D Monte-Carlo-Simulation der ergodisierten Randschicht von TEXTOR-DED*, Berichte des Forschungszentrums Jülich V. 4173

[30] F. M. M. Hasenbeck: *Development ans Application of a Multiscale Model for the Magnetic Fusion Edge Plasma Region*, Schriften des Forschungszentrum Jülich, Reihe Energie & Umwelt, Band 307 (2015)

[31] M. Henkel et al.: *Multi-channel retarding field analyzer for EAST*, Plasma Science and Technology 20 (2018)

[32] M. Henkel et al.: *Retarding field analyzer for the wendelstein 7-X boundary plasma*, Fusion Engineering and Design 157 (2020)

[33] Q. U. Hongpeng: *Ion-Banana-Orbit-Width EÆect on Bootstrap Current for Small Magnetic Islands*, Plasma Science and Technology, Vol.15 (2013)

[34] H. Hoelbe et al: *Access to Long-pulse Relevant Edge Scenarios in Wendelstein 7-X in its Early Phases of Operation*, EUROfusion (2015)

[35] M. Hölzl et al.: *Numerical modeling of diffusive heat transport across magnetic islands and highly stochastic layers*, Physics of Plasmas 14, 052501 (2007)

[36] M. Hölzl: *Diffusive Heat Transport across Magnetic Islands and Stochastic Layers in Tokamaks*, Technische Universität München (2010)

[37] A. Ishizawa et al.: *Multi-scale interactions between turbulence and magnetic islands and parity mixture - a review*, Plasma Physics and Controlled Fusion, Volume 61 (2019)

[38] G. Janzen: *Plasmatechnik. Grundlagen. Anwendungen. Diagnostik*, Hüthig (1992)

[39] B. B. Kadomtsev et al.: *Electron heat conductivity of the plasma across a 'braided' magnetic field*, Plasma Physics and Controlled Nuclear Fusion Research, Volume 1, page 649 (1979)

[40] A. von Keudell: *Einführung in die Plasmaphysik*, Lecture notes of Ruhruniversity Bochum (2014)

[41] M. Kikuchi et al: *Fusion Physics*, International Atomic Energy Agency (2012)

[42] M. Kočan et al.: *On the reliability of scrape-off layer ion temperature measurements by retarding field analyzers*, Review of scientific instruments (2008)

[43] M. Kočan: *Measurements of scrape-off layer ion-to-electron temperature ratio in Tore Supra ohmic plasmas*, Journal of Nuclear Materials 390–391 (2009)

[44] M. Kočan: *Ion temperature measurements in the scrape-off layer of the Tore Supra tokamak*, Université Henri Poincaré (2009)

[45] J. A. Krommes et al.: *Plasma transport in stochastic magnetic fields. Part 3. kinetics of test particle diffusion.*, Journal ofPlasma Physics 30 (1983)

[46] A. W. Leonard: *Edge localized modes in tokamaks*, Physics of plasmas 21 (2014)

[47] L. Y. Li et al.: *Hot spots induced by LHCD in the shadow of antenna limiters in the EAST tokamak*, Physics of plasmas 25 (2018)

[48] C. Liu et al.: *The effects of kinetic instabilities on the electron cyclotron emission from runaway electrons*, Nuclear Fusion, Volume 58 (2018)

[49] M. Maeda et al: *Measuring Method for Mach Number in Tokamak Edge Plasma Using Probes*, Japanese Journal of Applied Physics, Volume 38 (1999)

[50] G. F. Matthews et al: *The determination of sheath potential from retarding field analyser measurements in tokamak edge plasmas*, Journal of Nuclear Materials 145-147 (1987)

[51] I. Milch: *Kernfusion: Berichte aus der Forschung*, Max-Planck-Institut für Plasmaphysik (2002)

[52] I. Milch: *Magnettests an Wendelstein 7-X erfolgreich abgeschlossen*, Max-Planck-Institut für Plasmaphysik

[53] A. W. Molvik et al.: *Large acceptance angle retarding-potential analyzers*, Review of Scientific Instruments 52, 704 (1981)

[54] D. Nicolai et al.: *A multi-purpose manipulator system for W7-X as user facility forplasma edge investigation*, Fusion Engineering and Design 123, 960-964 (2017)

[55] J. Ongena et al.: *Magnetic-confinement fusion*, Nature Physics 12 (2016)

[56] A. K. Pandey, S.K. Karkari: *Characteristics of floating potential of a probe in electronegative plasma*, Physics of Plasmas 24 (2017)

[57] W. Peide: *Experimental Advanced Superconducting Tokamak - Design, Fabrication and Assembly*, Lecture at Institute of Plasma Physics, Chinese Academy of Sciences (2005)

[58] F. W. Perkins et al: *Chapter 1: Overview and summary*, Nuclear Fusion Volume 39 (1999)

[59] M. Preynas et al: *Experimental characterization of plasma start-up using ECRH in preparation of W7-X operation*, EPJ Web of Conferences 87, 02005 (2015)

[60] A. D. Rodatos: *Untersuchung der magnetischen Flussflächen am Stellarator WEGA*, Max-Planck-Institut für Plasmaphysik Greifswald (2011)

[61] E. Pisselhoy: *http://www.ipp.mpg.de/13232/technotransfer*, Max-Planck-Institut für Physik (2015)

[62] P. H. Rutherford: *Nonlinear growth of the tearing mode*, Physics of Fluids 16 (1973)

[63] M. Schneider et al: *On alpha particle effects in tokamaks with a current hole*, Plasma Physics and Controlled Fusion 47 ((2005)

[64] R. Schneider et al: *Plasma Edge Physics with B2-Eirene*, Contributions to Plasma Physics 46 (2006)

[65] R. P. da Silva et al: *ECE radiometry in the TCABR tokamak*, Brazilian Journal of Physics 34 (2004)

[66] A. Stampa: *Einführung in die Plasmaphysik*, Universität - Gesamthochschule Essen (2002)

[67] T. H. Stix: *Plasma transport across a braided magnetic field*, Nuclear Fusion 48 (1978)

[68] U. Stroth: *Material zur Vorlesung der Plasmaphysik*, Technische Universität München (2015)

[69] Y. Sun: *Nonlinear Transition from Mitigation to Suppression of the Edge Localized Mode with Resonant Magnetic Perturbations in the EAST Tokamak*, Physical review letters 117 (2016)

[70] j. Wesson: *Tokamaks*, Oxford University Press (2011)

[71] X. Xiao and S. Wang: *Explicit Runge–Kutta integrator with Hamiltonian correction for long-time simulations of guiding-center orbit in tokamak configurations*, Physics of Plasmas 15 (2008)

[72] Z. Xinjun et al: *Current Status of ICRF Heating Experiments on EAST*, Plasma Science and Technology, Vol.13 (2011)

[73] N. Yang et al: *Coherent structures in the boundary plasma of EAST Tokamak*, Technical university of Denmark (2014)

[74] F. Yude: *Electron Cyclotron Resonance Heating*, http://east.ipp.ac.cn (2016)

[75] G. Zhuang et al.: *Overview of the recent research on the J-TEXT tokamak*, Nuclear Fusion 55 (2015)

[76] H. Zohm: *Plasmaphysik*, Ludwig-Maximilians-Universität München (2012)